Article

Multi-Parametric Investigations on Aerodynamic Force, Aeroacoustic, and Engine Energy Utilizations Based Development of Intercity Bus Associates with Various Drag Reduction Techniques through Advanced Engineering Approaches

Yinyin Wang [1,2], Vijayanandh Raja [3,*], Senthil Kumar Madasamy [3], Sujithira Padmanaban [4], Hussein A. Z. AL-bonsrulah [5,*], Manivel Ramaiah [6], Parvathy Rajendran [7,8], Arul Prakash Raji [3], Anselme Muzirafuti [9] and Fuzhang Wang [10]

1 Economics and Management School, Nantong University, Nantong 226019, China; wyyntu11@163.com
2 Jiangsu Yangtze River Economic Belt Research Institute, Nantong University, Nantong 226002, China
3 Department of Aeronautical Engineering, Kumaraguru College of Technology, Coimbatore 641049, Tamil Nadu, India; senthilkumar.m.aeu@kct.ac.in (S.K.M.); arulprakash844@gmail.com (A.P.R.)
4 Masters in Computer Simulation in Science, Bergische Universität Wuppertal, Gaußstraße 20, 42119 Wuppertal, Germany; sujithira.padmanaban@uni-wuppertal.de
5 Iraqi Ministry of Oil, Midland Refineries Company, Najaf Refinery, Najaf 54001, Iraq
6 Department of Mechanical Engineering, Kumaraguru College of Technology, Coimbatore 641049, Tamil Nadu, India; manivel.r.mec@kct.ac.in
7 School of Aerospace Engineering, Universiti Sains Malaysia, Engineering Campus, Nibong Tebal 14300, Pulau Pinang, Malaysia; aeparvathy@usm.my or parvathy.rajendran@firstcity.edu.my
8 Faculty of Engineering & Computing, First City University College, Bandar Utama, Petaling Jaya 47800, Selangor, Malaysia
9 Dipartimento di Scienze Matematiche e Informatiche, Scienze Fisiche e Scienze della Terra, Università degli Studi di Messina, Via F. Stagno d'Alcontres, 31-98166 Messina, Italy; anselme.muzirafuti@unime.it
10 School of Mathematics and Statistics, Xuzhou University of Technology, Xuzhou 221018, China; wangfuzhang1984@163.com
* Correspondence: vijayanandh.raja@gmail.com (V.R.); huseenabd541@gmail.com (H.A.Z.A.-b.)

Abstract: The impacts of conflicting aerodynamic forces and side drifting forces are the primary unstable elements in automobiles. The action of an unstable environment in automobile vehicles increases the chance of an accident occurring. As a result, much study is required to determine how opposing aerodynamic forces and side drifting force affects function, as well as how to deal with them for safe and smooth navigation. In this work, an intercity bus is chosen as a main object, and computational fluid dynamics (CFD) analysis is used to estimate aerodynamic forces on the bus in all major directions. Experimentation is also carried out for validation reasons. CFD findings for a scaled base model and a dimple-loaded model based on experimental results from a subsonic wind tunnel are demonstrated to be correct. The drag forces generated by CFD simulations on test models are carefully compared to the experimental drag findings of same-dimensioned models. The error percentages between the results of these two methods are acquired and the percentages are determined to be within an acceptable range of significant limitations. Following these validations, CATIA is used to create a total of nine distinct models, the first of which is a standard intercity bus, whereas the other eight models are fitted with drag reduction techniques such as dimples, riblets, and fins on the surface of their upper cumulus side. A sophisticated computational tool, ANSYS Fluent 17.2, is used to estimate the comparative assessments of the predictions of aerodynamic force fluctuations on bus models. Finally, dimples on the top and side surfaces of the bus model (DESIGN–I) are proposed as a more efficient model than other models because dimples are a vital component that may lower pressure drag on the bus by 18% in the main flow direction and up to 43% in the sideslip direction. Furthermore, by minimizing the different aerodynamic force sources

without impacting the preparatory needs, the proposed model may provide comfortable travel. The real-time bus is created, and the finalized drag reduction is applied to the optimized places over the whole bus model. In addition, five distinct size-based bus models are developed and studied in terms of aerodynamic forces, necessary energy to resist aerodynamic drag, required forward force for successful movement, instantaneous demand for particular power, and fuel consumption rate. Finally, the formation of aeroacoustic noise owing to turbulence is estimated using sophisticated computer simulation. Last, for real-time applications, multi-parametric studies based on appropriate intercity buses are established.

---

1. Introduction

Nowadays, most people utilize the road for transportation, and buses play an important role because of their low cost [1]. Because of the widespread use, bus operators, both government and commercial, are constantly improving the amenities on board to entice customers. Anti-lock braking systems, completely air-conditioned systems, and shock absorption systems are significant features introduced in existing buses to ensure comfort during bus travel [2]. In addition to these amenities, operators must focus on maintaining a smooth, comfortable ride, which includes avoiding obstacles such as uneven road conditions, potholes, surface type, condition, and gradient, to mention a few. The crosswind of the bus is one of the key issues related to comfortable travel [3]. Crosswind is nothing more than side force to buses caused by the environment and/or other heavily laden vehicles. The crosswind impact might compress a bus's indentation direction, decreasing the bus's comfort. At most, a serious collision may occur as a result of a massive cascade effect from other heavily loaded cars. This work examines the effect of sideslip and ways to reduce it using advanced engineering methodologies [1,3].

1.1. Literature Survey

The main platform in this study is an intercity bus and its aerodynamic impact. Previous research revealed that crosswind is the most important element affecting the comfort of bus travel, with the origins of crosswind being natural conditions and/or external influences from heavy vehicles [3]. The CFD and its experimental validation were mostly used in the analysis of the aerodynamic force on buses [4,5]. As a result, this work also employed CFD-based research on side force impact on intercity buses, with subsonic wind tunnel-based practical testing carried out to validate CFD results [4,5]. The key benefit of a CFD-based simulation study is the availability of correct boundary conditions, which facilitate the convergence process in the CFD solver [5]. Because the working fluid is turbulent in nature in the presence of tiny disturbances, the turbulence model and its subordinate parameters play an important role in the aerodynamics study. Thus, the fundamental objective for implementing the turbulence model in this CFD study was accomplished and finished in order to determine which type of turbulence model is appropriate for this article. Furthermore, the kind of solver, the type of inlet conditions and their values, and an appropriate approach to link pressure and velocity were discovered [6]. Previous works performed extensive investigations of drag on automotive vehicles, in which drag reduction strategies such as the implementation of streamline shapes at the frontal area, the implementation of riblets, and the implementation of zigzag cuts were soundly applied [7]. Furthermore, the use of the aforementioned procedures was applied to limit airflow separation at potential areas such as stagnation points, curved forms, side mirrors, and so on [8]. As a consequence of these successes, the pressure drags on the automobile vehicle can be reduced, wherein aerodynamically two separate forms of drags such as pressure drag and skin friction drag have been contributing significantly to the lowering of performance of an automotive vehicle. As a result, pressure drag reduction

techniques are inevitably utilized in automotive vehicles to lessen the opposing force (drag) that operates in the opposite direction of forward-moving vehicles [9]. Similarly, drag reduction strategies are employed in this study to minimize turbulence caused by the primary aerodynamic force in the major direction and crosswind at the side section of an interstate bus. In general, the geometrical variation occurs at the side face of the bus (top of the window), which allows for the occurrence of flow separation of crosswinds [10]. Because of these turbulence forms, pressure imbalances are formed at the side face, pushing the buses away from the main highways. As a result, the loss of side force owing to pressure drag must be addressed using appropriate drag reduction techniques.

1.2. Proposed Concept

In this research, eight distinct drag reduction approaches are utilized, and their aerodynamic performance studies are done using CFD [11]. Taking these eight models into consideration, four versions were created with the addition of dimples. As a result, the authors of this present work think that the dimple-based drag reduction strategy can lower the dynamic pressure increase at flow separation zones, reducing the production of undesirable turbulence over the intercity bus. Because the authors are mainly interested in exploring the presence of dimples and their side effects, four alternative dimple-based models are imposed in this work. Figure 1 depicts a visual depiction of this suggested notion.
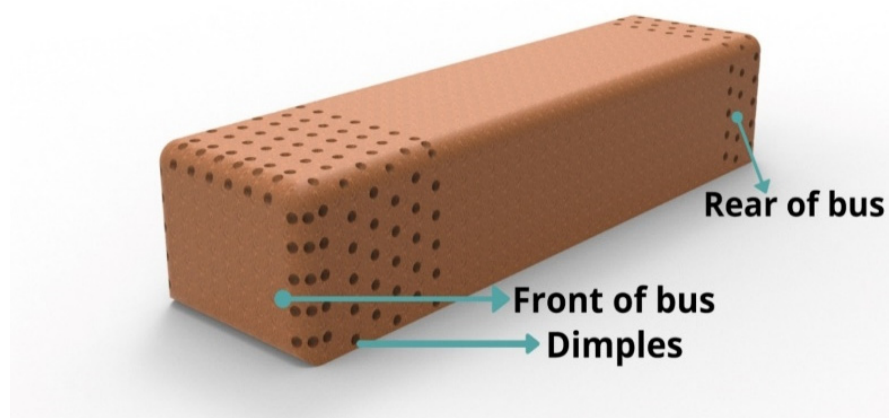

Figure 1. Proposed drag reduction technique on an intercity bus.

2. Proposed Methodologies

The competence of the problem-solving approach adds substantially to the creation of trustworthy output in research efforts. The key evaluation elements involved in the approach selection process are the nature of the problem and its criticality. Aside from the problem viewpoint, the capability study of the approach is also critical in providing an acceptable solution to complex situations [12]. As a result, reciprocal relevance and integration between real-time issues and their solution approaches are necessary. This study analyzes comparative aerodynamic force calculations on several intercity bus types, with a total of eight models built. In addition, three alternative operating velocities are examined for each model to gain a better understanding of the aerodynamic forces and their impacts on all directions. The eight models are as follows: the base bus model, a bus with dimples on the side and top surfaces, a bus with inverted dimples, a bus with more dimples on the side and top surfaces, a bus with alternate square cuts on the side surface, a bus with fins with a gap of 10 mm at the top and side surfaces, a bus with fins with a gap of 20 mm at the top and side surfaces, and a bus with riblets. In order to handle such large and crucial issues, an appropriate and adaptable technique, such as CFD-based simulation, is required [13]. Fluid property simulation is generally based on the Navier–Stroke equation [13–26] and is assisted by numerical methods-based solutions. The

following factors contributed to the selection of this simulation methodology: flexibility at any level, minimal processing time, the user-friendly approach, and the ability to forecast complicated situations.

2.1. Conceptual Design

The main frame of an intercity bus was selected as this paper's main design platform, and is a dual viewpoint component when compared to others. The multiple viewpoints are structurally important in transporting passengers and aerodynamically important in producing more drag than other components such as tires, windows, mirrors, and so on. The initial phase in the conceptual design was to display three-dimensional bus models. This was a necessary step before employing the CFD approach.

A standard bus and its dimensions were employed, as determined by earlier research [2,14]. Because the technique is time-consuming, only a 1/10th scaled model of the original bus was employed for the full comparative CFD study. The following are the scaled dimensional parameters of the present bus base model: The bus's length is 1006 mm, its width is 208 mm, and its height is 263 mm, with a radius of 10 mm at each corner. CATIA (Computer Aided Three-dimensional Interactive Application) was used to create the bus design. Drag reduction methods such as dimples, riblets, and inverted dimples are particularly difficult to represent in geometry; hence, a sophisticated modeling tool such as CATIA is best suited for these stages. Figure 2 depicts both the reference and the base bus models. Table 1 contains all the data of the imposed drag reduction approaches.
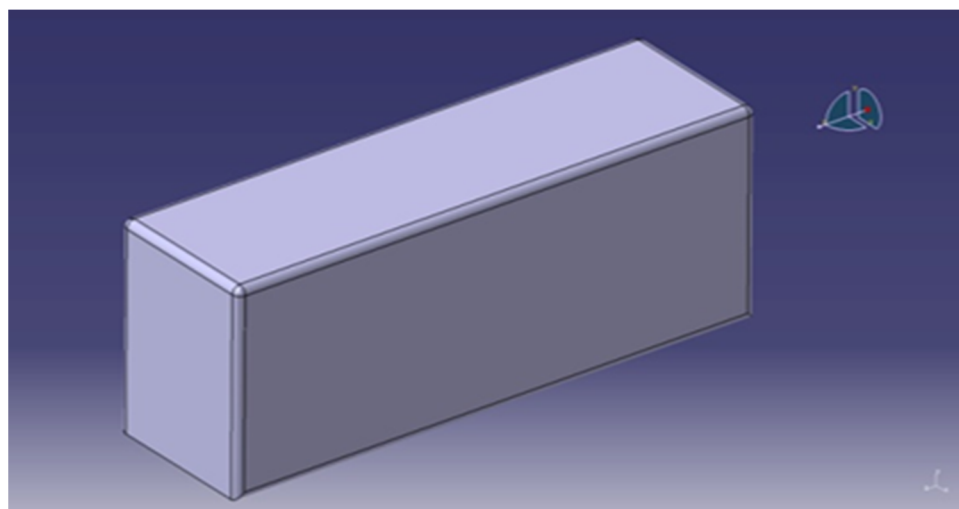

Figure 2. A typical view of the base design of the intercity bus's main body.

All the main flow directions (drag force developing direction) except Model V are taken as the z-direction. The main flow directions in Model V are taken as the x-direction.

2.1.1. Model I—Bus Body Equipped with More Dimples on the Top and Side Surfaces

The specification for the bus model is covering the top, front, and sides with dimples 5 mm in diameter with the help of groove options. In addition, the frontal portion is covered with more dimples than the rear due to its adverse effect on pressure. Since most comparative drag investigations dealt only with the scaled model, these kinds of low design data dimples were acceptable. The authors recommend that the proportional multiplication of this dimple design be a mandatory process to be done in real-time. The design of a bus equipped with a greater number of dimples at its top and side surfaces is shown in Figure 3.

Table 1. Comprehensive explanations of various drag reduction techniques.

Bus Model	Corresponding Figure Number	Description about the Proposed Drag Reduction Techniques
Base model	2	The modeled bus is considered the base, so no modifications are imposed on this model.
Model I	3	A blunt body (outer shape of the bus model) equipped with more dimples on the top and side surfaces
Model II	4	A blunt body (outer shape of the bus model) equipped with inverted dimples on the top and side surfaces
Model III	5	A blunt body (outer shape of the bus model) equipped with dimples on the side and top surfaces
Model IV	6	A blunt body (outer shape of the bus model) equipped with square cuts on the side surface
Model V	7	A blunt body (outer shape of the bus model) equipped with fins with a gap of 10 mm on the top surface
Model VI	8	A blunt body (outer shape of the bus model) equipped with fins with a gap of 20 mm on the top surface
Model VII	9	A blunt body (outer shape of the bus model) equipped with riblets on the top surface
Model VIII	10	A blunt body (outer shape of the bus model) equipped with dimples on the top surface
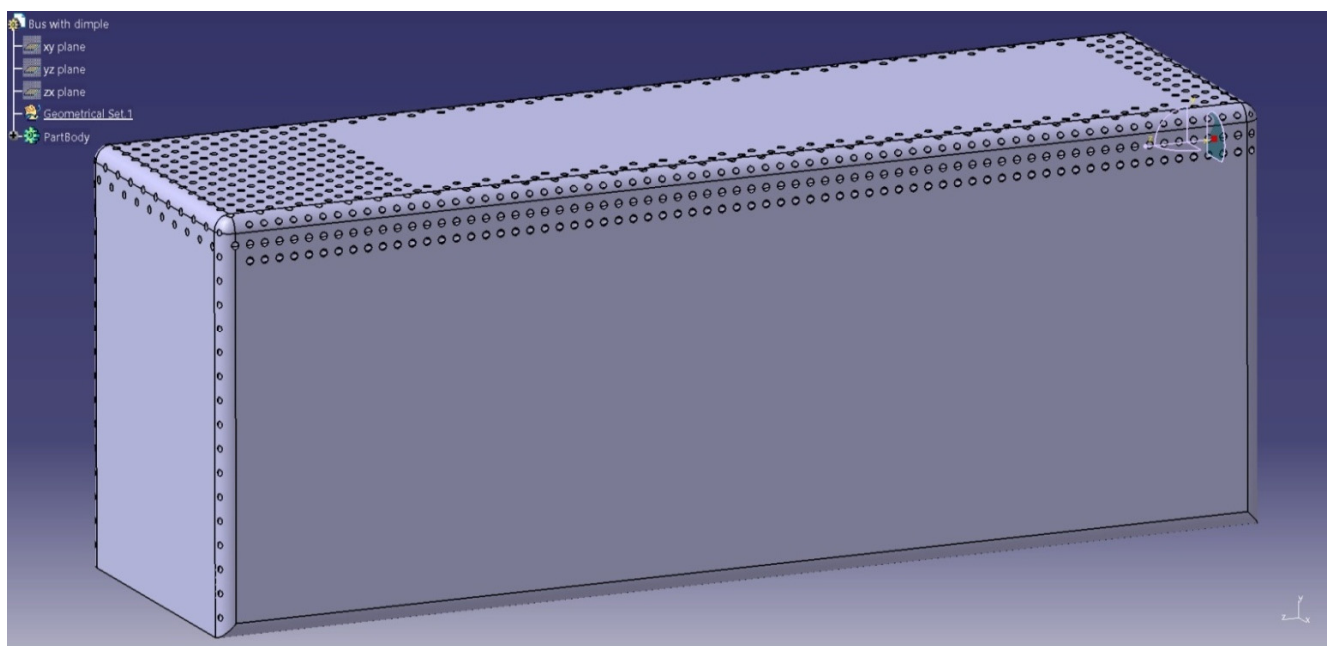
Figure 3. An isometric view of the main body of an intercity bus loaded with many dimples located partially on the top and side faces.

2.1.2. Model II—Bus Equipped with Inverted Dimples on the Top and Side Surfaces

The unique design specification imposed on this bus model is inverted dimples on the top and side faces, where the dimple diameter is 5 mm and the distance between dimples in each row is 15 mm. The fillet radius is 10 mm, where the initiation of the dimple modeling is 10 mm from the origin point with respect to the bus. Figure 4 reveals the bus model with inverted dimples on the top and side surfaces.
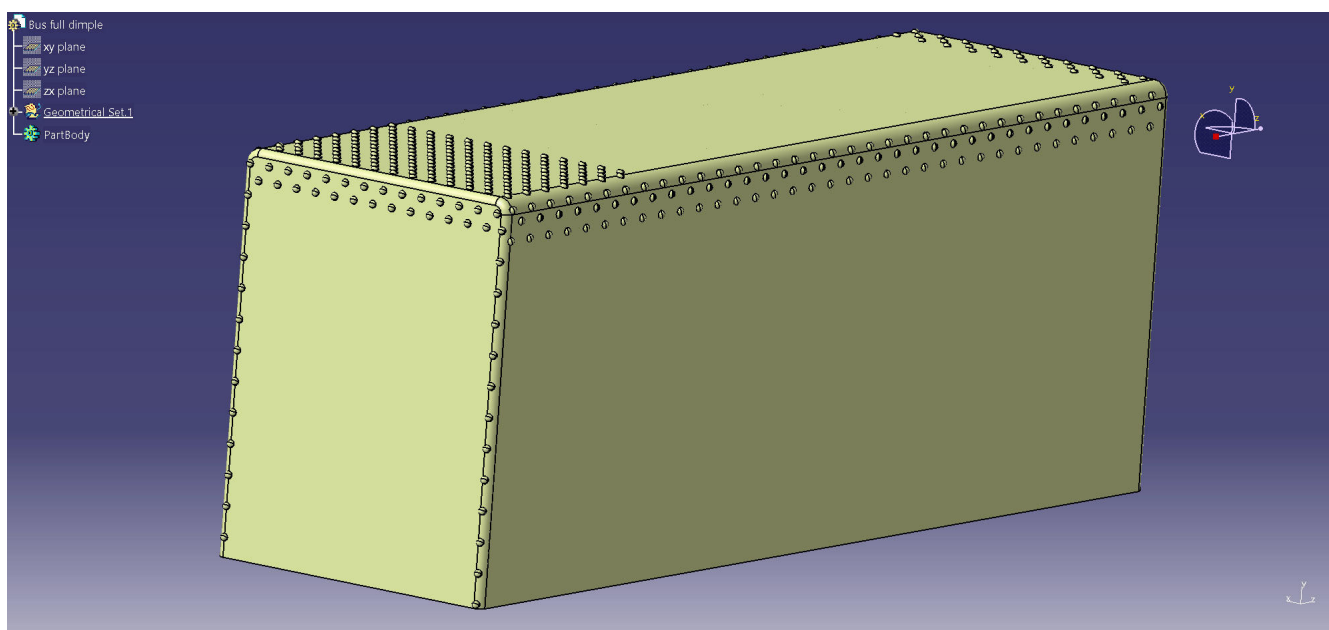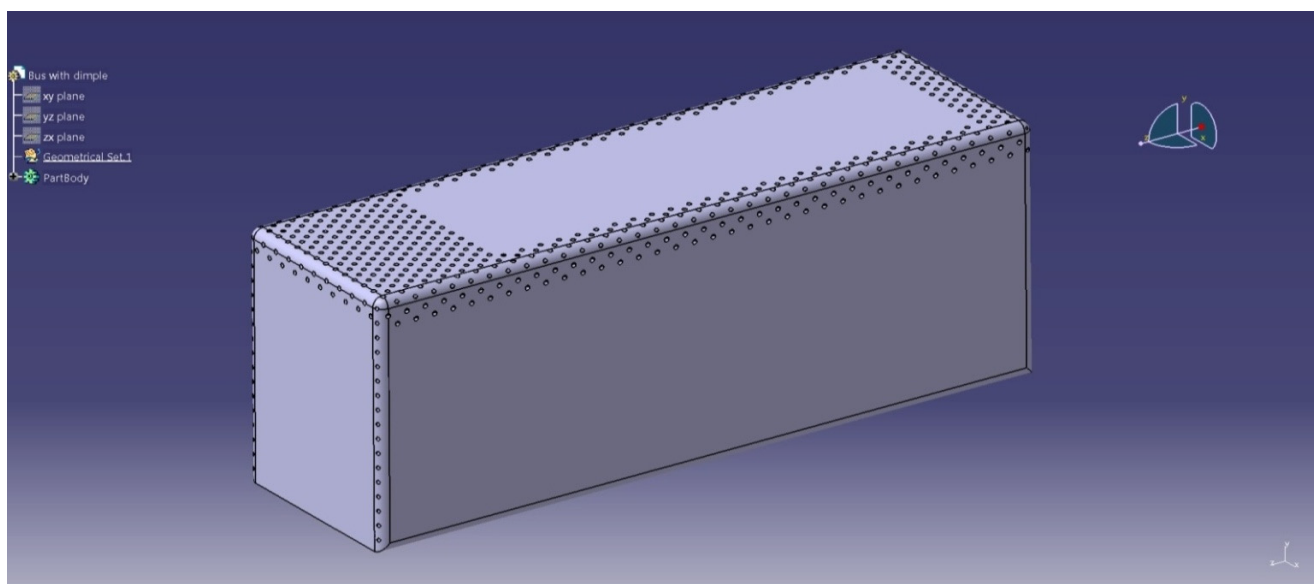
Figure 4. An isometric view of the main body of an intercity bus loaded with a medium number of inverted dimples located partially on the top and side faces.

2.1.3. Model III—Bus Equipped with Dimples on the Side and Top Surfaces

In this design, as shown in Figure 5, the dimple diameter is 5 mm and the distance between dimples in each row is 15 mm, whereas the fillet radius is taken as 10 mm. In the fillet region, the inter-distance between dimples is 10 mm, ordered in two rows with respect to both sides of the fillet at the bus edge. On the front side bus model, 6 rows and 2 rows of dimples are presented on the top of the front of the bus model and at the rear of the bus model, respectively.

Figure 5. An isometric view of the main body of an intercity bus loaded with a medium number of dimples located partially on the top and side faces.

2.1.4. Model IV—Bus Equipped with Square Cuts on the Side Surface

The design characteristics of bus model IV include the removal of rectangular space of 10 mm in the lengthwise direction and a frontal blend diameter of 10 mm, as depicted in Figure 6.
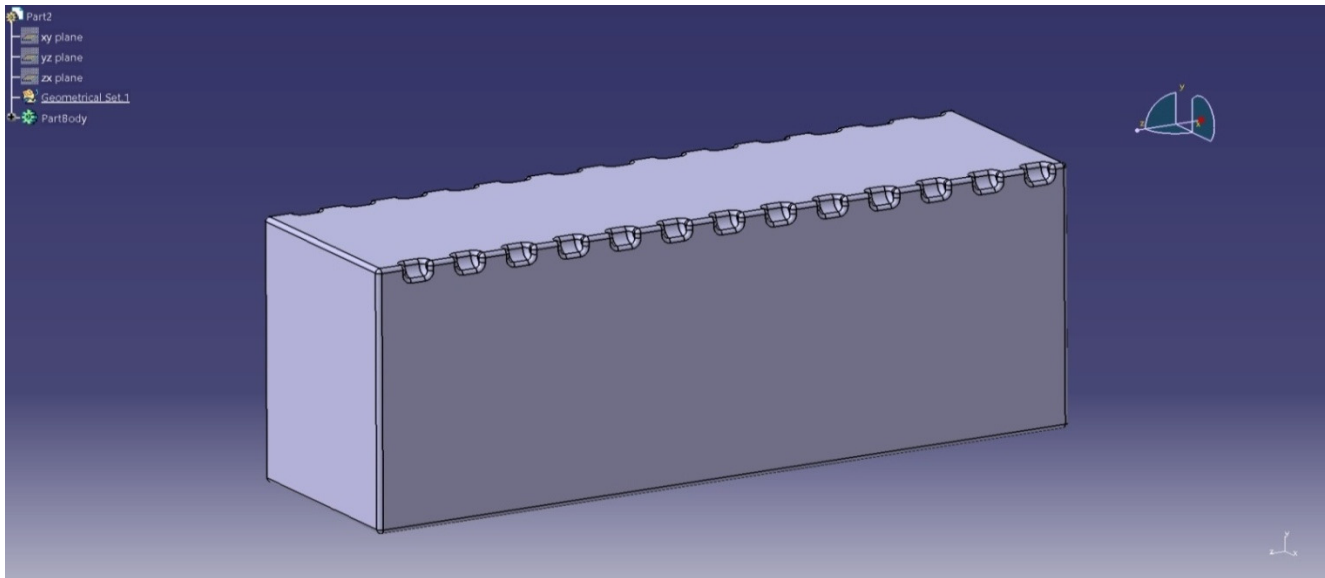

Figure 6. An isometric view of the main body of an intercity bus loaded with a small number of square cuts located on the side faces in the longitudinal direction.

2.1.5. Model V—Bus Equipped with Fins with a Gap of 10 mm on the Top Surface

In this design, the bus is modeled with a rectangular cut section with a length of 5 mm and a breadth of 5 mm running through the entire width of the top surface of the bus at a distance of 10 mm from each other, as depicted in Figure 7.
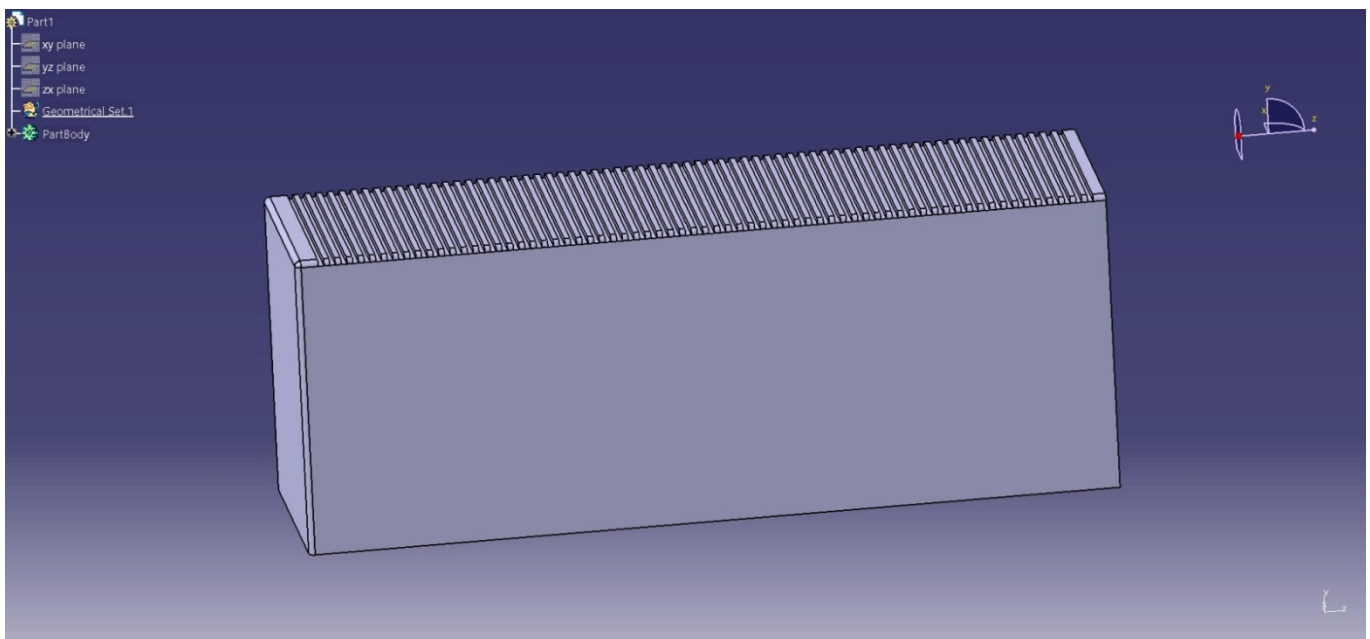

Figure 7. An isometric view of the main body of an intercity bus loaded with a high number of 10 mm gap-based fins on the top faces.

2.1.6. Model VI—Bus Equipped with Fins with a Gap of 20 mm on the Top Surface

In this bus model, the rectangular cut section of the length is kept at 5 mm and the depth is kept at 5 mm, whereas the inter-distance spacing varies from 20 mm for the flow passage. Figure 8 clearly shows the bus modeled with fins at a distance of 20 mm from one another on the top surface.
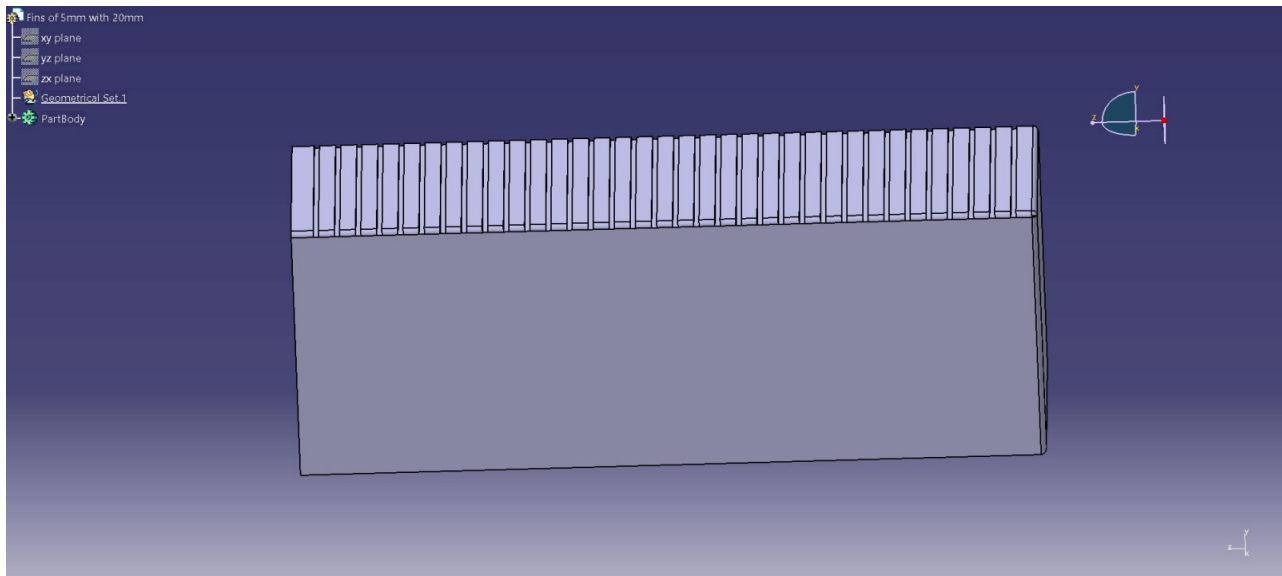

Figure 8. An isometric view of the main body of an intercity bus loaded with a medium number of 20 mm gap-based fins on the top faces.

2.1.7. Model VII—Bus Equipped with Riblets on the Top Surface

In this design, the bus is modeled with a saw-toothed or triangular cut section on the top with a height of 5 mm. These proposed geometrical representations, which are implemented on the top of the intercity bus, are referred to as riblets. Because of the area variations throughout the longitudinal directions of the bus, the free stream velocity in these imposed regions may decrease. The bus modeled with riblets is shown in Figure 9.
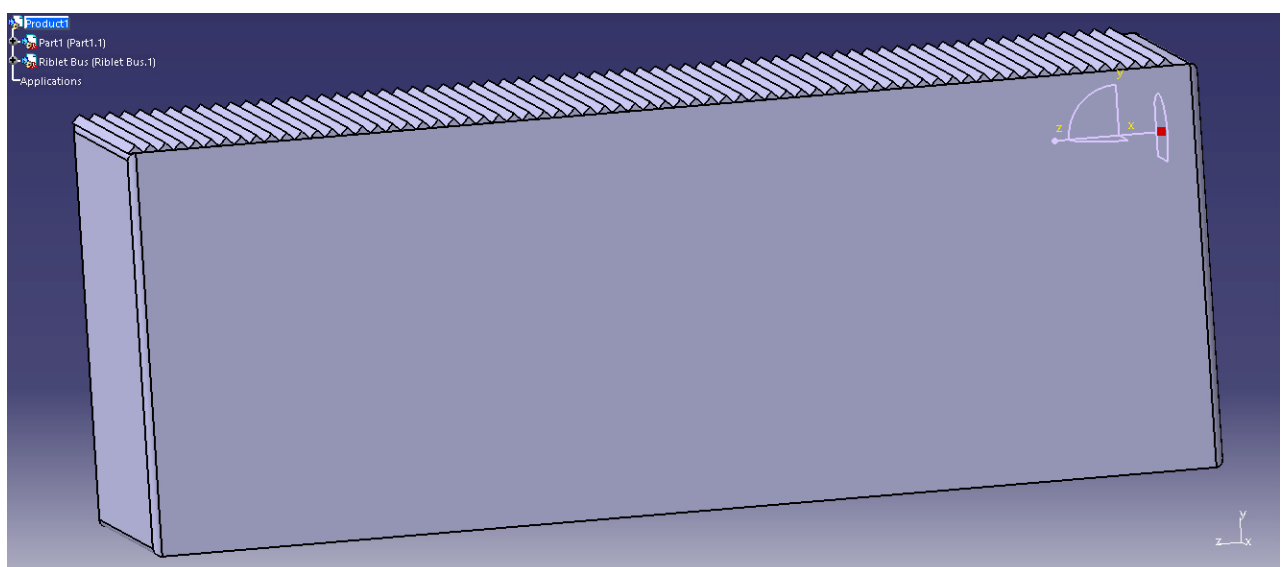

Figure 9. An isometric view of the main body of an intercity bus loaded with a high number of riblets on the top face.

2.1.8. Model VIII—Bus with Dimples on the Top Surface

The bus modeled with dimples on the top surface, as shown in Figure 10, has dimples predominantly on the top surface. The dimple diameter is 5 mm, and they are placed very close to one another. As a bonus, two rows of dimples cover the bus's corner edges as well.
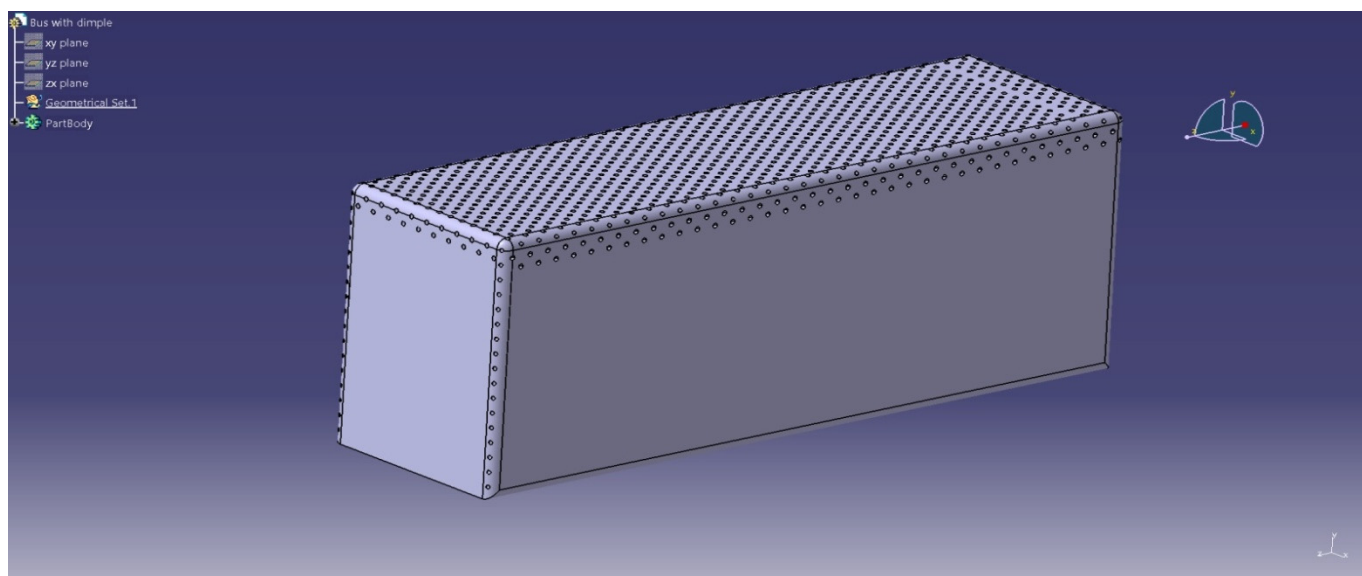
Figure 10. An isometric view of the main body of an intercity bus loaded with a medium number of dimples located completely on the top and partially on the side faces.

2.2. Discretization on the Bus Body

The discretization approach, in general, serves as the foundation for numerical integration, which is an unavoidable step in the CFD technique [1]. The discretization technique was carried out with the assistance of an analytical program, specifically ANSYS Mesh 17.2. The ANSYS Workbench 17.2 version of both academic and research licenses has been offered for all types of computational simulations. The CATIA design is provided in the geometry component of the computational tool, which is included in the Fluid Flow (ANSYS Fluent 17.2) analysis system [1]. The flow field over the bus was constructed in the design modeler by selecting the Enclosure option from the Tools menu. The created enclosure was of the box type, with 4 m on each side of the bus in the x-direction and 2 m on each side of the bus in the y- and z-directions. Using the Create menu's Boolean option, the bus was removed from the contained box. The flow field was then discretized in the meshing phase by setting the relevance center to fine, the smoothing to high, and the transition to fine [15]. The grid data for each discretized piece of music had 643,964 nodes and 3,458,589 elements [1].

Figures 11–14 depict typical viewpoints of several forms of discretized structured control volume with intercity bus models. All of these mesh structures were built with the intention of conducting grid independence research on sideslip force-based investigations. The mesh for main flow aerodynamics analysis was generated in the same way as the mesh for sideslip analysis. Figures 15 and 16 depict a typical internal cut-plane-based elemental view of the whole control volume with the bus, as well as a zoomed projection view of the bus. For the main flow and sideslip flow computations, the reference lengths for control volume formation were taken as the length of the bus and the width of the bus, respectively. All 10 mesh instances (five mesh cases for sideslip analysis and five mesh cases for main flow aerodynamics analysis) were projected to have a mesh quality of between 0.975 and 0.99.
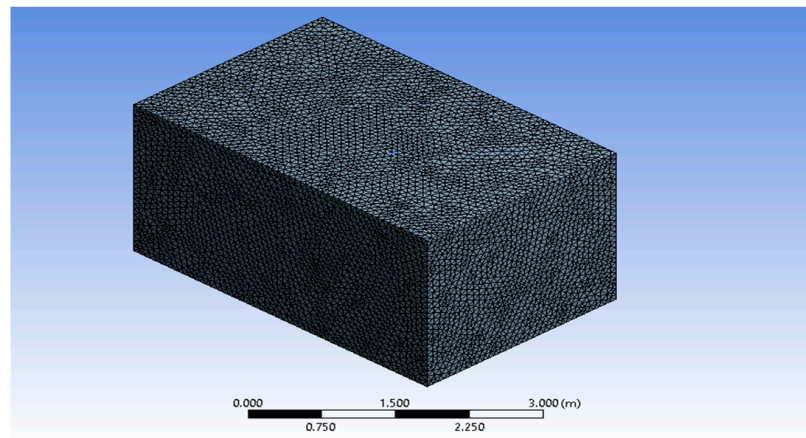
Figure 11. Solid model view of the discretized structure of the base bus model—curvature-based unstructured mesh.
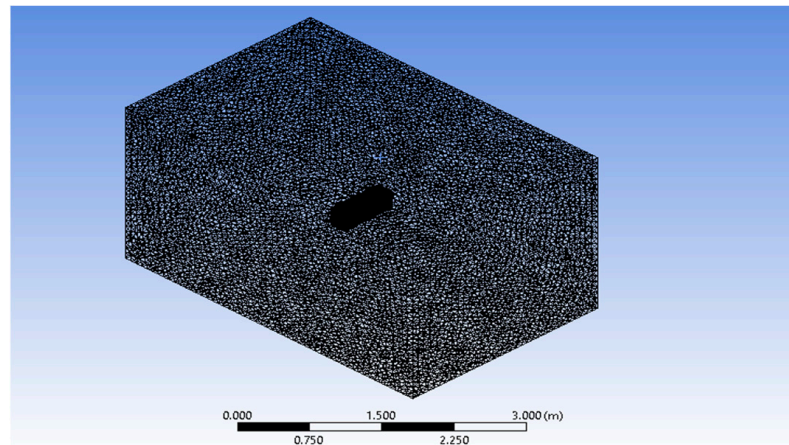

Figure 12. Wireframe model view of the discretized structure—fine curvature with face mesh setup on model VI.
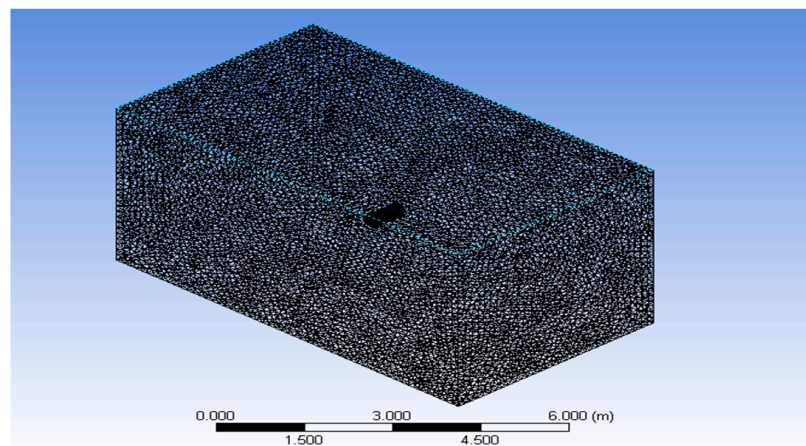

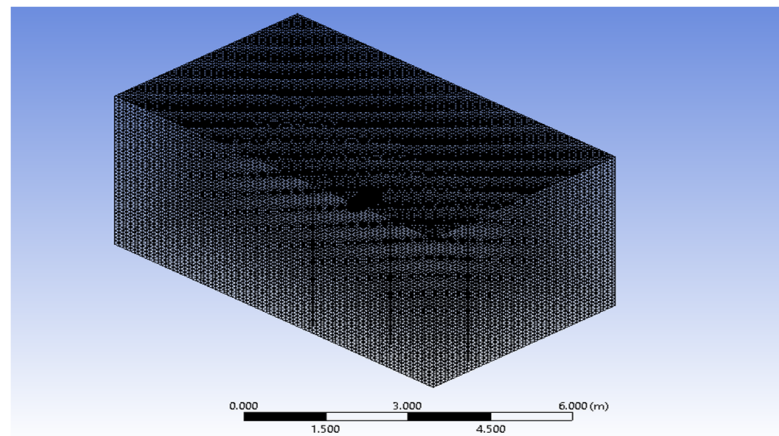**Figure 13.** Wireframe model view of the discretized structure of model IV—area proximity-based unstructured mesh.

Figure 14. Typical view of the fine curvature and proximity with face mesh setup on model VIII.
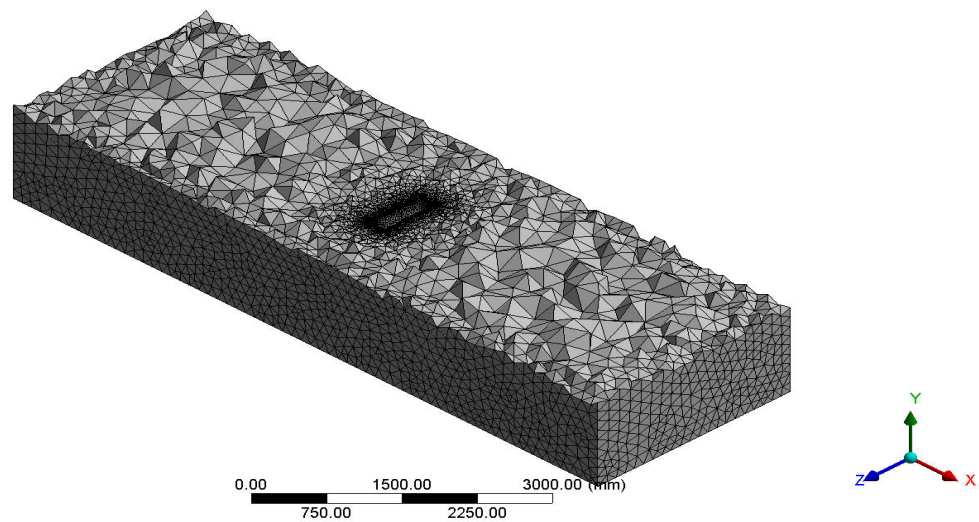

Figure 15. Typical internal cut-plane view of the entire control volume—sideslip analysis.
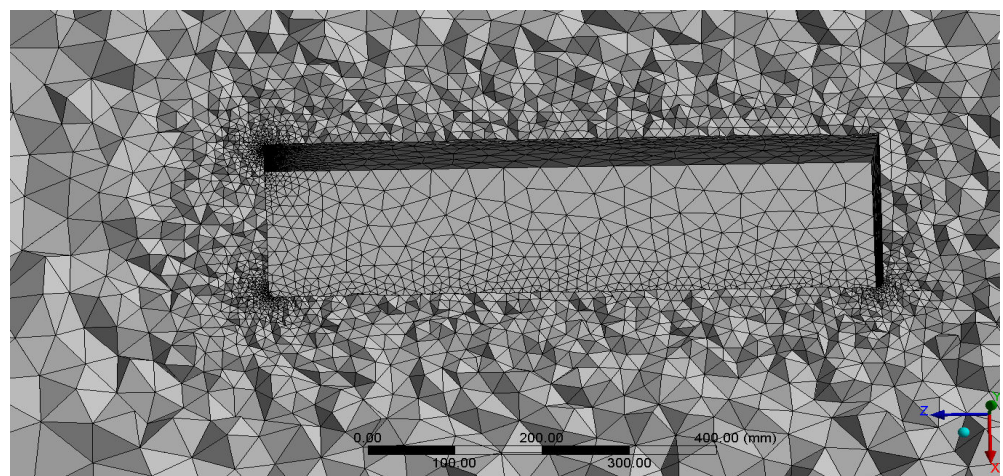

Figure 16. Typical internal cut-plane view of the entire control volume—sideslip analysis.

Because the coordinate system played an important role in the development of discretization and the achievement of appropriate processing time, Figure 15 clearly shows the enforced global coordinate system for these extensive studies. For all other circumstances, the same coordinate system was used.

2.3. Boundary Conditions

The boundary conditions and governing equations are the most important compositional elements in the mathematical modeling of CFD-based boundary value issues. In general, the boundary value issue has both natural and artificial boundary conditions, with no and free slips falling under natural boundary circumstances [16]. As a result, boundary condition requirements are critical in CFD-based situations, since accurate conditions can only deliver acceptable results. The current geometry was separated into pieces, namely, inlet, outlet, wall, and bus, using the named selection option for the ease of defining the beginning and boundary conditions. Figure 17 clearly depicts the information imposed on the computation's beginning circumstances. The analytical solver in this study was pressure-based, using a constant time and absolute velocity formulation. The majority of the time, the working environment and its fluid were regular atmospheric conditions based on one, which did not vary over time due to the usual surroundings with extremely minimal external disturbances. As a result, although the majority of the preceding publications finished their CFD studies under constant flow circumstances, steady flow was used in this analysis as well. Because it is simple to use, the conventional k-model was chosen as the viscous and turbulence model [17–19]. The air flowing over the bus had a density of 1.225 kg/m^3 and a viscosity of 1.7894×10^{-5} kg/(ms). The operating pressure was set at 101,325 Pascal [1], the usual static pressure acting on the bus's working environment (atmospheric pressure). The inlet was a velocity inlet with magnitudes of 5 m/s, 10 m/s, and 15 m/s for each of the three situations. The outlet had a gauge pressure of 0 Pascal and was a pressure outlet. The bus and the wall were both considered fixed walls with no-slip properties. To be linked, the solution technique for pressure-velocity coupling was chosen. Second-order upwind was specified for the spatial discretization gradient, pressure, momentum, turbulent kinetic energy, and turbulent dissipation rate. Under the monitors, drag, lift, and moment monitors were constructed. The hybrid initialization method was used to start the solution. In order to obtain a flawless solution, the residuals of all the solving parameters were given a value of 10^{-6}. As a result, the convergence criteria for all residuals were given as 10^{-6}. The force operating in the x-direction was estimated in the post-processing window using the force calculator. The pressure contour and velocity stream were also recorded, and the results for all design alterations were compared in three distinct ways [16].
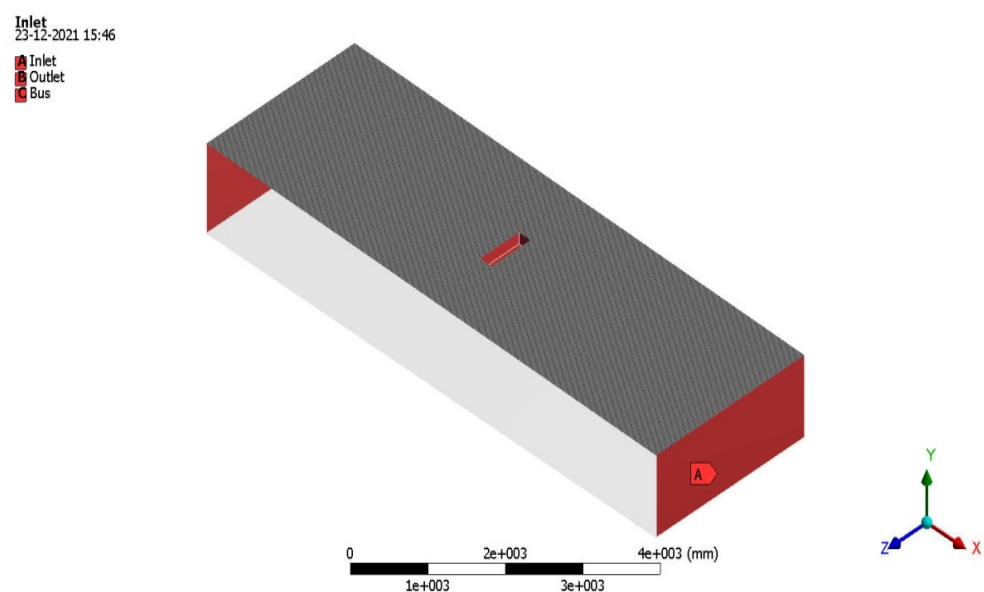

Figure 17. Details of the initial conditions imposed on the control volume.

2.4. Governing Equations

CFD-based issues rely heavily on numerical integration, which is carried out using the finite volume technique, finite difference method, mesh-less method, finite element approach, and so on [20]. In general, finite volume techniques are utilized everywhere, with the volume integral and surface integral of each mesh element playing a significant role. This numerical integration is the simplest version of CFD's governing equations, in which averaging principles are used to anticipate complex fluid phenomena using numerical calculations. All of these computations, including the continuity equation, momentum equation, and energy equation, are essential for the DNS (direct numerical simulation) approach, and the Reynolds averaged Navier–Strokes equations are essential for the finite volume method. The generalized term of the continuity and momentum equations is given in Equations (1) and (3), which comprise all of the components. Thus, the fluid's working nature and its working circumstances for the issues guide the equations included in this governing equation. Because the working condition was low speed, incompressible and steady flow was employed throughout the whole analysis, and Equation (1) was changed and is presented in Equation (2). In every non-nuclear continuum mechanics study, mass conservation is reflected in the continuity equation. The equation is created by taking the flow rate of mass in and out of a control volume and setting the net flow rate equal to the rate of change in mass within the control volume. The conservation rules have a more powerful local version in the form of continuity equations. Isolated systems cannot change mass via chemical reactions or physical changes, according to the law of conservation of mass.

$$\nabla \cdot \vec{V} = 0 \tag{1}$$

$$\frac{\partial(u)}{\partial x} + \frac{\partial(v)}{\partial y} + \frac{\partial(w)}{\partial z} = 0 \tag{2}$$

Equation (3) comprises important terms, which is termed as a momentum equation. Using Newton's second law of motion, the momentum equation is derived. The law of motion may be summarized as mass times acceleration equals force. Body forces and surface forces are the primary contributors of force. These include the gravitational force, electromagnetic forces, and so on. The pressure force, viscous forces, etc., all play a role in surface forces. Then there are the viscous forces, which include normal and shear stress. Depending on their nature, normal stress forces are exerted outside the control volume. Based on its nature, the control volume is compressed by pressure forces.

$$-\nabla p + \mu \nabla^2 \vec{V} + F = \rho (\vec{V} \cdot \nabla) \vec{V} \tag{3}$$

Equations (4) and (5) describe the terms in the generalized equations in further detail, where

$$\nabla = \frac{\partial}{\partial x} + \frac{\partial}{\partial y} + \frac{\partial}{\partial z} \tag{4}$$

$$\nabla^2 = \frac{\partial^2}{\partial x^2} + \frac{\partial^2}{\partial y^2} + \frac{\partial^2}{\partial z^2} \tag{5}$$

More crucially, this aerodynamics analysis was entirely dependent on reducing drag by reducing pressure drag caused by the creation of turbulence over the buses. As a result, the incorporation of turbulence models into complex calculations in order to adequately capture turbulence was both an unavoidable and required procedure. According to the survey, two equation turbulence models based on k-epsilon and k-omega are good for determining the presence of turbulence in incompressible flow calculations. The governing relationships of the aforementioned turbulence models [21–26] are represented by Equations (6)–(9). Firstly, the governing equations of k-epsilon are given in Equations (6) and (7), wherein Equation (6) comprises the analytical representation of turbulent kinetic energy (k) and Equation (7) comprises the analytical representation of turbulent dissipation (ε).

The model equation for the turbulent kinetic energy (k) is as follows:

$$\frac{Dk}{Dt} = \frac{\partial k}{\partial t} + \overline{u_j}\frac{\partial k}{\partial x_j} = \frac{\partial}{\partial x_j}\left[\frac{v_t}{\sigma_k}\frac{\partial k}{\partial x_j}\right] + P - \varepsilon \tag{6}$$

where the term $\frac{\partial k}{\partial t}$ is denoted as the rate of increase of k, the term $\overline{u_j}\frac{\partial k}{\partial x_j}$ is convective transport, the term $\frac{\partial}{\partial x_j}\left[\frac{v_t}{\sigma_k}\frac{\partial k}{\partial x_j}\right]$ is diffusive transport, the term P is the rate of production, and the term ε is the rate of destruction.

The model equation for the turbulent dissipation (ε) is as follows:

$$\frac{D\varepsilon}{Dt} = \frac{\partial \varepsilon}{\partial t} + \overline{u_j}\frac{\partial \varepsilon}{\partial x_j} = \frac{\partial}{\partial x_j}\left[\frac{v_t}{\sigma_g}\frac{\partial \varepsilon}{\partial x_j}\right] + C_{g1}\frac{P\varepsilon}{k} - C_{g2}\frac{\varepsilon^2}{k} \tag{7}$$

where the term $\frac{\partial \varepsilon}{\partial t}$ is denoted as the rate of increase of ε, the term $\overline{u_j}\frac{\partial \varepsilon}{\partial x_j}$ is convective transport, the term $\frac{\partial}{\partial x_j}\left[\frac{v_t}{\sigma_g}\frac{\partial \varepsilon}{\partial x_j}\right]$ is diffusive transport, the term $C_{g1}\frac{P\varepsilon}{k}$' is the rate of production, and the term $C_{g2}\frac{\varepsilon^2}{k}$' is the rate of destruction, so $C_{g1} = 1.44$; $C_{g2} = 1.92$; $\sigma_k = 1$; $\sigma_g = 1.3$.

Secondly, the governing equations of k-omega are given in Equations (8) and (9). This model comes under two equation categories, in which a modified version of the k equation is used in the k-ω model. A transport equation for ω is dissipation per unit of kinetic energy. Equation (8) comprises the analytical representation of modified turbulent kinetic energy (k) and Equation (9) comprises the analytical representation of dissipation per unit of kinetic energy (ω).

The equations for k and ω are as follows:

$$\frac{Dk}{Dt} = \frac{\partial k}{\partial t} + \overline{u_j}\frac{\partial k}{\partial x_j} = \frac{\partial}{\partial x_j}\left[v + \frac{v_t}{\sigma_k}\frac{\partial k}{\partial x_j}\right] + v_t\left(\frac{\partial[u_i]}{\partial x_j} + \frac{\partial[u_j]}{\partial x_i}\right)\frac{\partial[u_i]}{\partial x_j} - \beta^* k\omega \tag{8}$$

$$\frac{D\omega}{Dt} = \frac{\partial \omega}{\partial t} + \overline{u_j}\frac{\partial \omega}{\partial x_j} = \frac{\partial}{\partial x_j}\left[v + \frac{v_t}{\sigma_\infty}\frac{\partial \omega}{\partial x_j}\right] + \alpha v_t\left(\frac{\partial[u_i]}{\partial x_j} + \frac{\partial[u_j]}{\partial x_i}\right)\frac{\partial[u_i]}{\partial x_j} - \beta_1\omega^2 \tag{9}$$

where the term $\frac{\partial k}{\partial t}$ is denoted as the rate of increase of k, the term $\overline{u_j}\frac{\partial k}{\partial x_j}$ is convective transport, the term $\frac{\partial \omega}{\partial t}$ is denoted as the rate of increase of ω, and the term $\overline{u_j}\frac{\partial \omega}{\partial x_j}$ is convective transport. Similar to the k-epsilon equations, the other terms such as rate of production, rate of destruction, and diffusive transport are incorporated into Equations (8) and (9). The standard values of all the model constants are $\beta_1 = 0.075$; $\beta^* = 0.09$; $v_t = 0.553$; $\sigma_k = \sigma_\infty = 2.0$.

2.5. Grid Independence Studies (GIS)

Grid independence studies are widely performed to reduce numerical issues such as erroneous findings and a lack of mesh quality. To increase the consistency of their conclusions, challenging engineering topics should be treated to a grid independence study. In recent years, one of the critical issues involved in the selection of an advanced engineering approach has been the verification of CFD-based projected data estimates [24–29]. Because the purpose of this work is to limit the creation of vortices on the bus's boundary layer separation zones using different difficult drag reduction strategies, the counter check process of the outcome through a grid independence study is a crucial one, capable of delivering acceptable outputs. Two different GIS studies were done on bus model I for forward direction calculation and model VIII for sideslip analysis in this study. Both experiments consisted of five separate unstructured-mesh instances with a 10 m/s input velocity. Because bus models I and VIII are more advanced in terms of design and simulation, they were purposely chosen as reference models for these convergence studies in

order to fine-tune the results. Table 2 has a detailed description of the meshes and their primary components, such as nodes and elements. The results of extensive investigations on bus models I and VIII utilizing the aforementioned boundary conditions are displayed in Figures 18 and 19. Figures 18 and 19 clearly illustrate that case 3 outperformed all other mesh instances; hence, case 3 mesh approaches were chosen for all further analyses.

Table 2. Comparative information of all the mesh cases.

Types of Meshes	Details of Statics of Mesh	
	Number of Nodes	Number of Elements
Case 1—coarse mesh	101,163	554,695
Case 2—medium mesh	252,276	1,369,327
Case 3—fine mesh	523,346	2,818,069
Case 4—fine with face mesh set-up	696,383	3,843,318
Case 5—fine with inflation mesh set-up	643,964	3,458,589
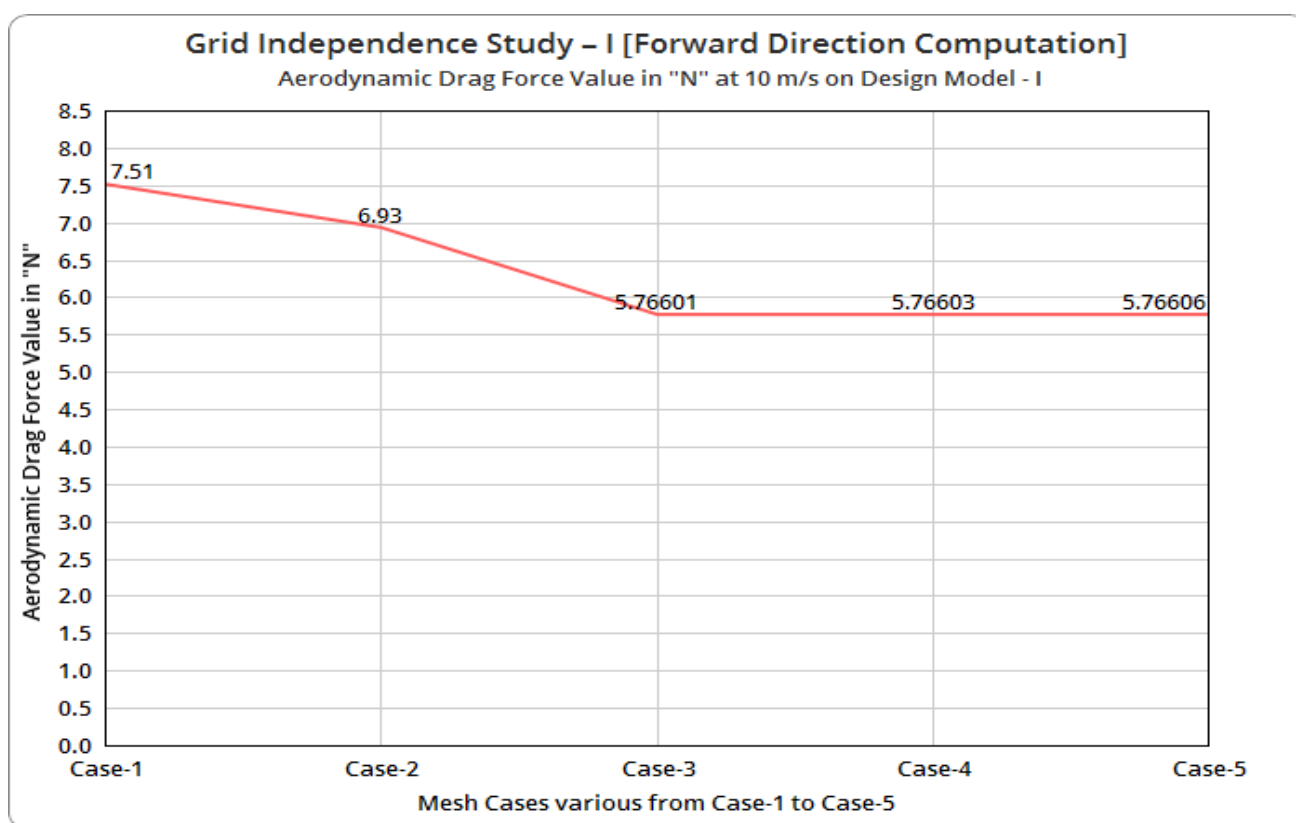
Figure 18. Comprehensive drag value in N at 10 m/s on model I.

The evaluation parameters for forward and side force-based computations in these GISs were aerodynamic drag and side-slip forces, respectively. Both of the previously stated parameters were crucial for their calculations; more precisely, they served as judges in the optimization of an appropriate model. Regardless of the enormous counts of components imposed, the projected drag values were quite similar to each other when the discussion was carried out on the first GIS, following mesh scenario III. The same environment was extended for the next GIS as well; thus, the mesh scenario III was well suited to offer trustworthy results, taking into account other important qualities such as minimal computation time consumption, attainment of repeatability of discoveries, and so on.
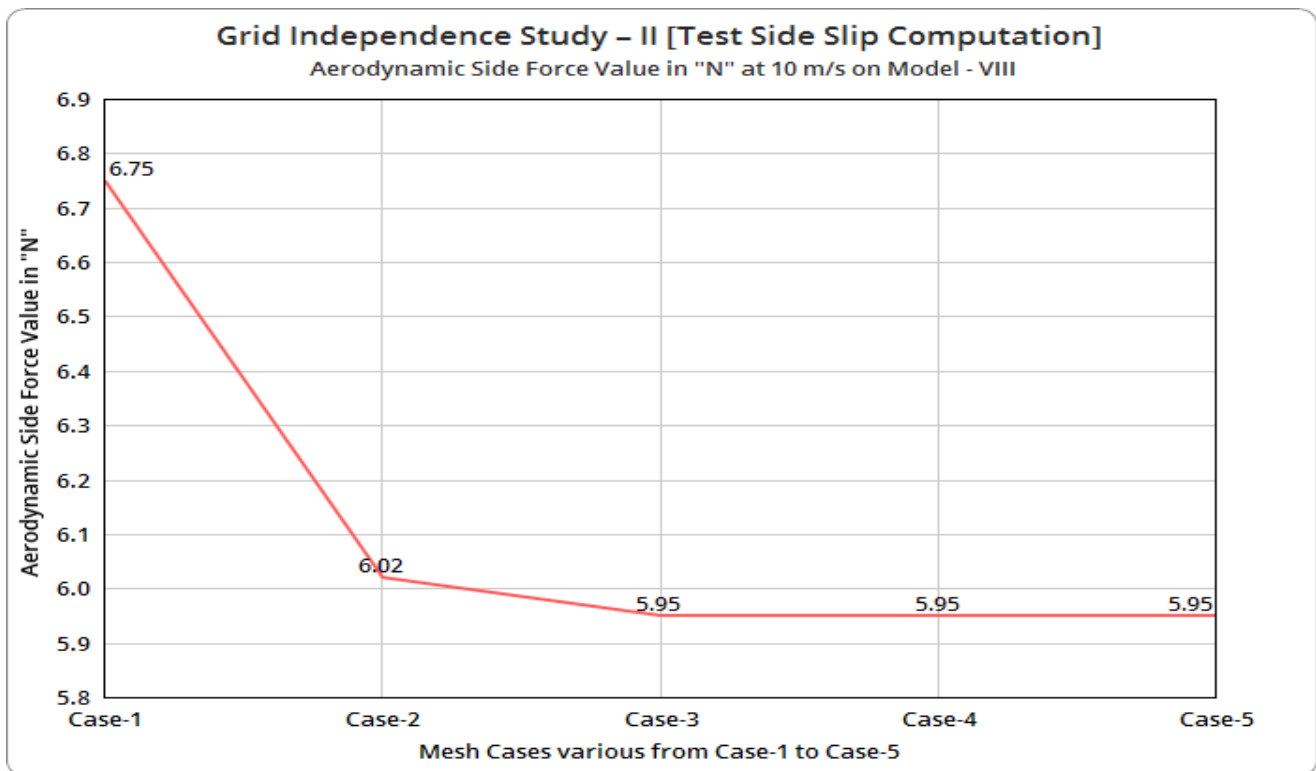
Figure 19. Comprehensive side force value in N at 10 m/s on model VIII.

2.6. Validational Study on the Proposed Methodology

In general, numerical simulation solutions are influenced by boundary and initial conditions such as turbulence model selection, initial value provision, selection of a second-order solution, and so on. As a result, rather than an approximate solution, previous fieldwork should be necessary to achieve an acceptable (highly efficient outcome of an approximate) response. Although numerical simulation is a sophisticated technique that may address critical issues, the addition of a systematic platform-based procedure may raise questions about the output's dependability. As a result, the validation of the simulation-based technique provides confidence regarding the estimated output's correctness. In this work, practical experiments with a low-speed wind tunnel were performed to examine the basis of an intercity bus model, and the results are supported by computer models.

2.6.1. Experimental Results

The experimental platform was a subsonic wind tunnel with a maximum capacity of 40 m/s fluid velocity across a 1 m length of test section. Figure 20 depicts the whole configuration of the subsonic wind tunnel used in these comparative experimental tests. This subsonic wind tunnel was modified with a data collection system that can give a numerical output of aerodynamic forces such as lift and drag, as well as input conditional factors such as rotor RPM and fluid particle entrance velocity [18]. In this systematic data collection system, hot film-based air velocity measurement was primarily imposed. The working ranges of this developed data collection system are capable of measuring aerodynamic outcomes efficiently for velocity ranging from 0.1 to 40 m/s, temperature ranging from 0 to 120 °C, and electrical output ranging from 4 to 20 mA. Because the output measurement format is completely digitalized, this data gathering system includes a small reconfigurable input and output controller. The main specs of the electronics controller are a 667 MHz dual-core A9 processor, plus a field programmable gate array processor, 512 MB of base read-only memory, and 256MB of DDR3 relayed random access memory. This computer has four USB ports and four Ethernet ports that it can use to connect. This computer runs a real-time Linux operating system.

Figure 20. Typical full view of the subsonic wind tunnel with the data acquisition system (bottom right).

As a reference test specimen, the base intercity bus model with no drag reduction was employed, which is a scaled model with a 1/10th ratio of the original model. The primary goal of these experiments was to evaluate the CFD-based aerodynamic forces on an intercity bus model, with the diffuser, test specimen stand, and data gathering equipment heavily employed for output extraction. The material utilized for the building of the foundation and drag reduction of the equipped bus types was wood. Wind velocity ranges were calculated based on fieldwork and a literature review, with velocities ranging from 14 m/s to 35 m/s employed as the inlet velocity for this experiment. In this imposed wind tunnel, in-built equipment measured flow velocities of 14 m/s, 17 m/s, 20 m/s, 22 m/s, 25 m/s, 28 m/s, and 35 m/s at the site of the test section where the test specimen was situated. The drag force generated on the bus model for various input velocities was measured and is presented in Table 2 using a data-gathering device. Figure 21 depicts typical cross-section and front views of the base bus model-based test configuration. As shown in Figure 22, each dimple on the test specimen had a front view like this one.

Figure 21. Typical zoomed-in and normal views of an intercity bus without dimples located in the test section.

Figure 22. Typical view of an intercity bus with dimples.

2.6.2. Numerical Results—Validation Case

In the subsequent phase of validation, the CFD technique was used to evaluate the aerodynamic parameters on the same scaled bus model. The literature review was quite useful in this CFD validation analysis, particularly with regard to the pressure solver, turbulent flow implementation, details of starting circumstances, and appropriate techniques of mesh representation in the solver [13]. The aforementioned velocities were subjected to CFD simulations, which principally investigated changes in dynamic pressure acting on the whole bus area, velocity distributions over the entire bus, turbulence creation, and aerodynamic force computation. Figure 23, which depicts the flow over the bus, also depicts the velocity streamlines together. Drag estimations and coefficient of drag values were also expected to be compared as significant post-processing evaluation factors. The data shown are all for a fluid input velocity of 35 m/s.
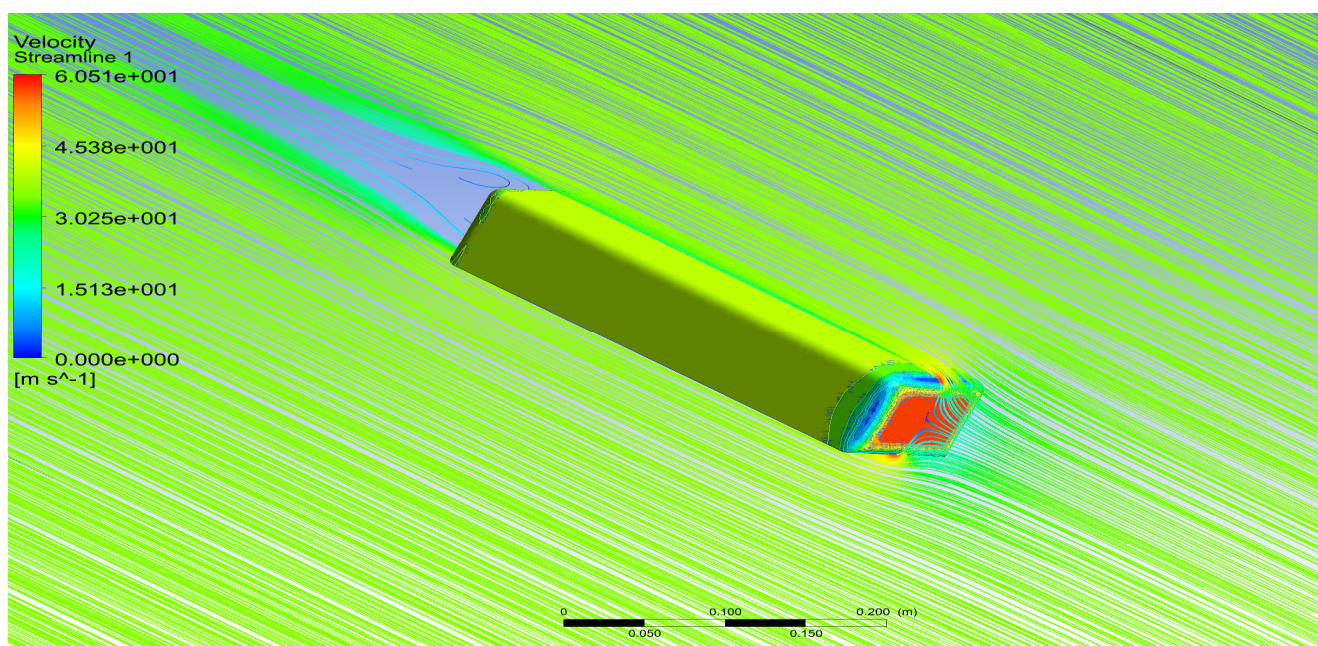
Figure 23. Velocity distributions over the bus models—tested only for experimental validation.

As shown in Figure 24, the pressure variations of the basic bus model were used to calculate the drag force acting on the bus as a result of aerodynamic forces.
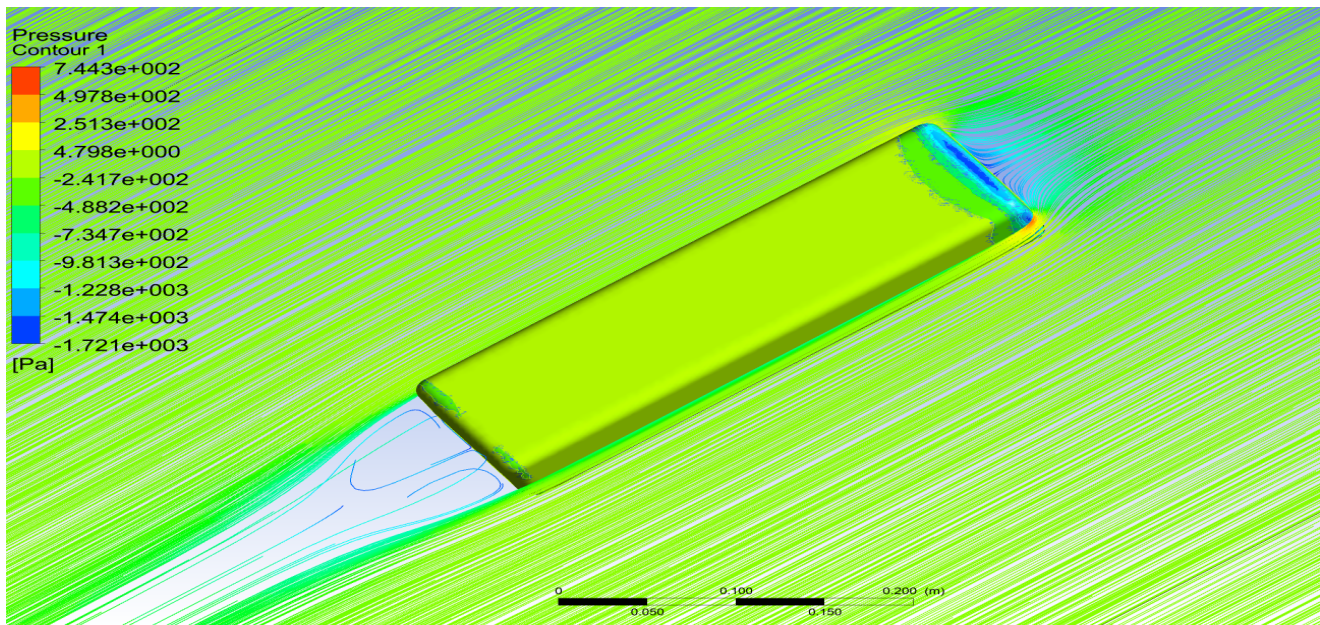
Figure 24. Pressure distributions over the bus models—tested only for experimental validation.

After the experiment and acquiring the CFD results, both the case outcomes were noted and are listed in Table 3. The aerodynamic drag values were carefully monitored when they went above 20 m/s due to the bus's nature [26].

Table 3. Comparison of drag on the bus models.

Velocity (m/s)	Drag (N) (Without Dimples)			Drag (N) (With Dimples)		
	Experimental	Numerical	Error Percentages	Experimental	Numerical	Error Percentages
14	0.26	0.2428	6.615385	0.489	0.45	7.97546
17	0.59	0.394	33.22034	0.4855	0.45	7.312049
20	0.7	0.67	4.285714	0.71	0.66	7.042254
22	1.01	0.98	2.970297	1.01	0.996	1.386139
25	1.3	1.194	8.153846	1.15	1.073	6.695652
28	1.37	1.2613	7.934307	1.25	1.1973	4.216
35	1.695	1.55	8.554572	1.6	1.56	2.5

The following information may be gleaned from Table 3: The coefficient of the drag value was observed during the convergence of iterations, and it was noticed that at a velocity of 22 m/s, the coefficient of the drag decreased from 0.51 to 0.306. The drag also decreased from 22 m/s to 1 to 8.5% by constructing dimples in the front and rear sections of the intercity bus. At low speeds, the drag forces in the model with dimples were somewhat higher than in the type without dimples. At high speeds, the drag force was smaller in the dimpled models than in the non-dimpled models, and the drag values decreased by 15 to 20% in the bus with dimples compared to the bus without dimples. Furthermore, the predicted drag values were quite similar to one other, indicating that the established boundary conditions are valid and capable of solving additional complex bus models. Despite this tiny discrepancy, the error % was computed using Equation (10) for confirmation.

$$\text{Error rate} = \frac{[\text{Experimental Result} - \text{CFD Result}]}{[\text{Experimental Result}]} \qquad (10)$$

$$\text{Error rate} = \frac{[1.15 - 1.073]}{[1.15]} \Rightarrow \text{Error rate} = 0.06695$$

From Equation (10), the error percentage between the computational results and the experimental result was estimated to be 6.69%. Because engineering calculations can have an error rate of less than or equal to 10%, the proposed methods for reducing drag are better for future automotive vehicles.

3. Results and Discussions

All of the previously defined boundary conditions, governing equations, and numerical integrations were included in the remaining modified and complicated bus models. Comparative studies of various conceptual bus models tried to achieve an optimistic conclusion as a result of the conceptual design's pressure gradient, flow separation, and incremental change in velocity rather than the current reality. Every bus model was imposed with small geometrical processes that may have enhanced eddy production; thus, complex as well as adaptable engineering methods were necessary to deal with such intricate settings, and computational fluid dynamics-based methodologies were applied [21].

3.1. Numerical Results—Forward Direction

The CFD technique was used on numerous bus models in the condition of forward speed maneuvers in the first experiment. Pressure forces acting on the frontal region of the bus, velocity distributions of fluid particles over the bus, and the production of turbulence in and around the bus were the primary results in this scenario. All of the previously discussed variables were calculated for each bus model and are shown in Figures 25–42.
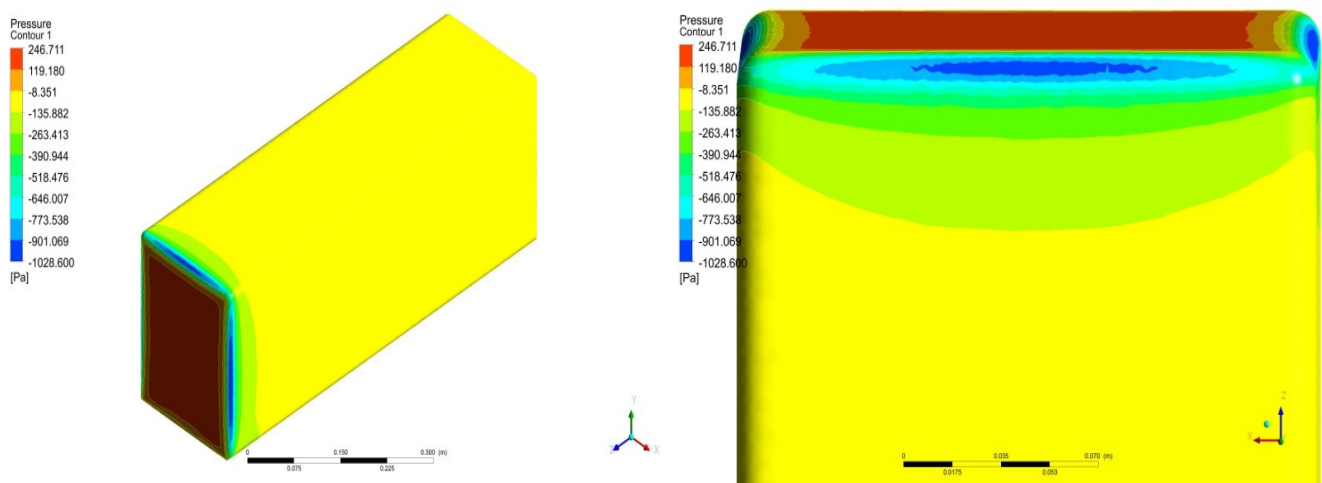
Figure 25. Typical isometric and zoomed-in frontal views of aerodynamic pressure distributions on the base model.

In general, the streamline and vector-dependent representations (Figure 26) were used to characterize the behavior of fluid particles within and around intercity buses. In order to comprehend the creation of eddies, the prospective flow separation zones were also tracked using total pressure prediction (Figure 25). According to the results of the base model, the velocity increase on the intercity bus occurred proportionately to distance. The top surface of the bus began perpendicularly at the ends of the frontal section to allow for extremely efficient flow separations. Based on these findings, the additional models were subjected to identical boundary conditions imposed by the CFD calculations. The imposed drag reduction approaches were chosen based on their ability to minimize the magnitude of free stream velocity once geometrical differences were considered.
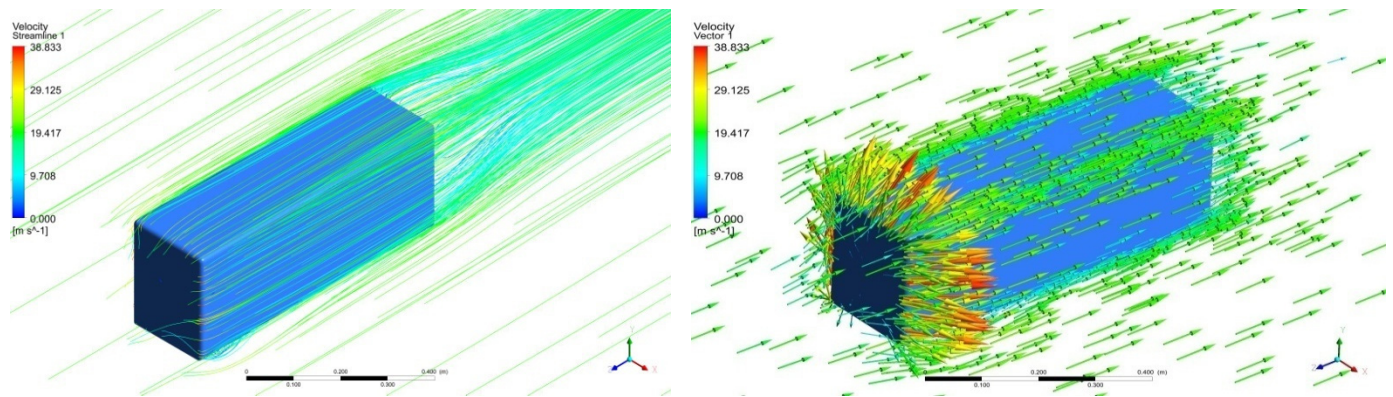
Figure 26. Streamline- and vector-based representations of air fluid velocity variations over the base model—isometric projections.
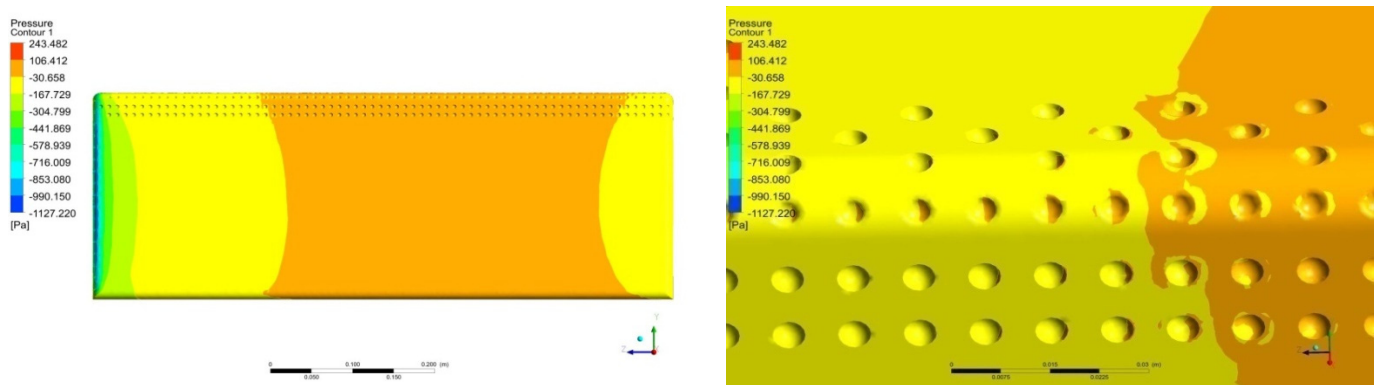

Figure 27. Methodical side and zoomed-in frontal views of aerodynamic pressure distributions on bus model I.
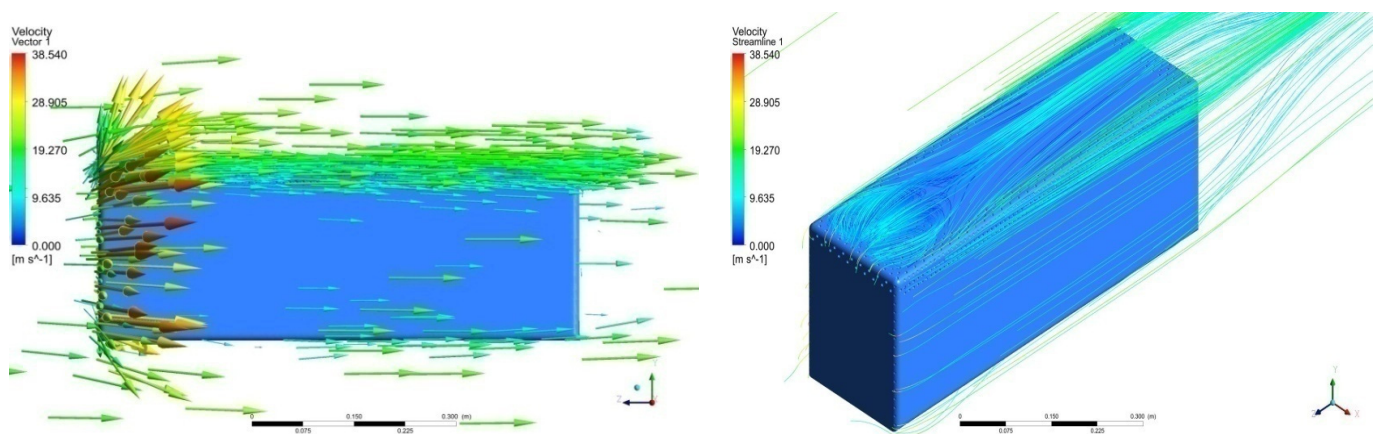

Figure 28. Vector and streamline-based representations of air fluid velocity variations over the first bus model—side and isometric projections.
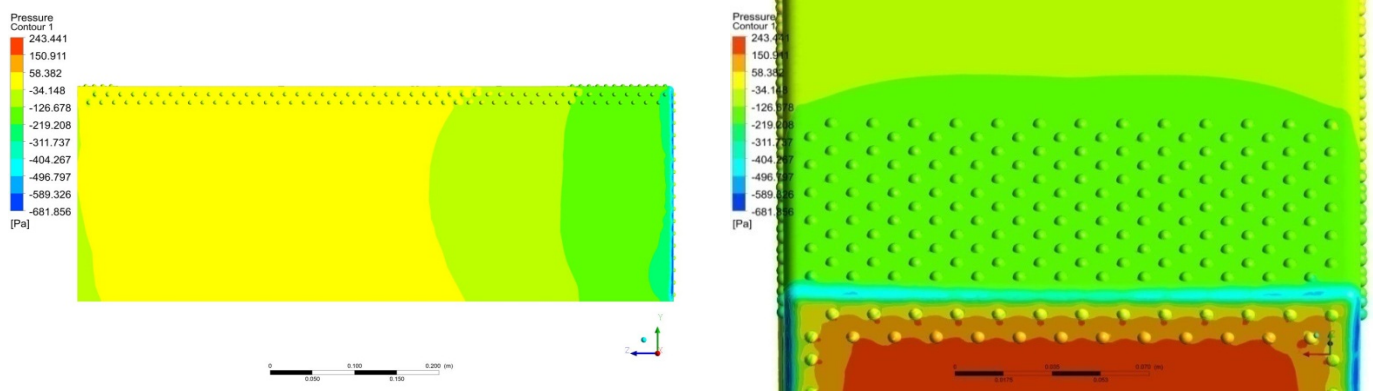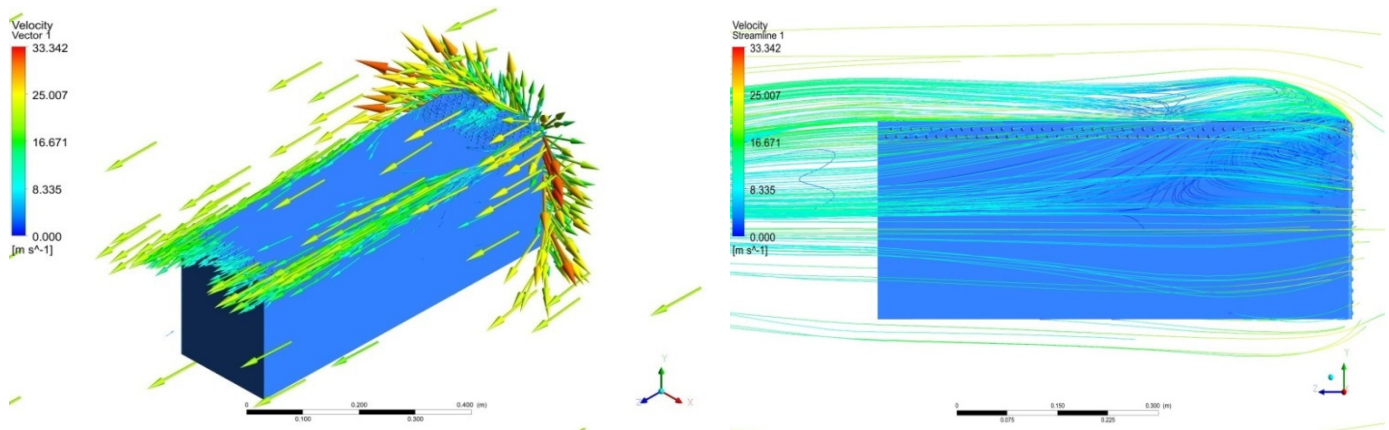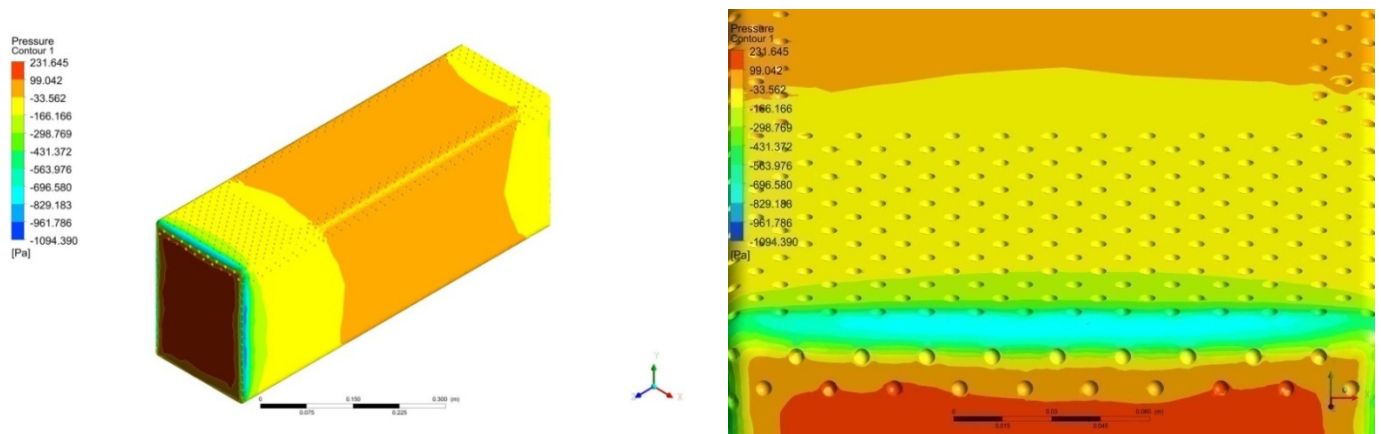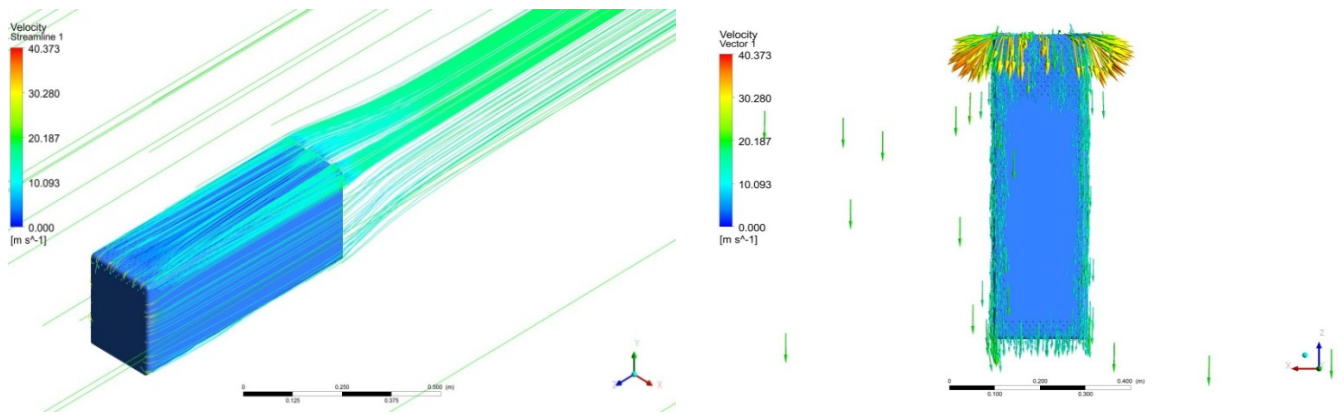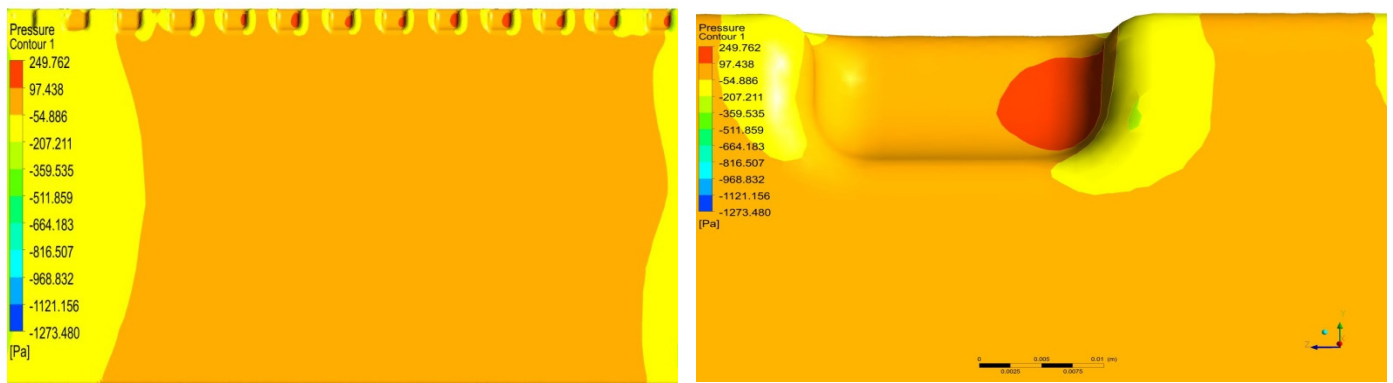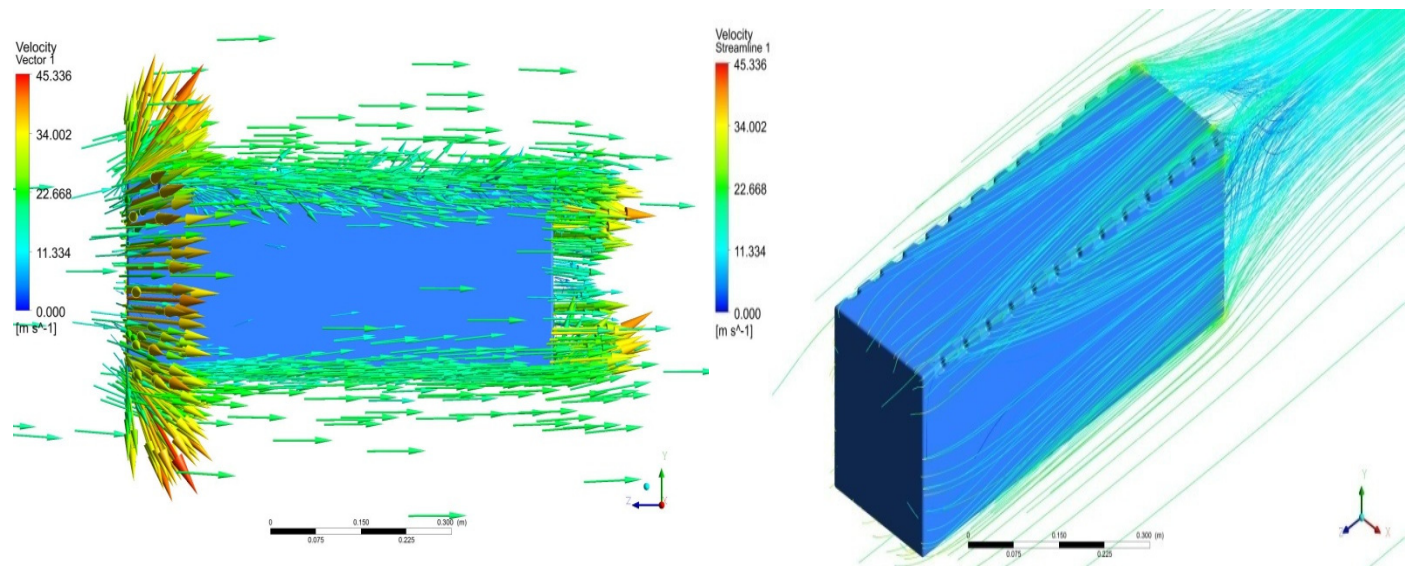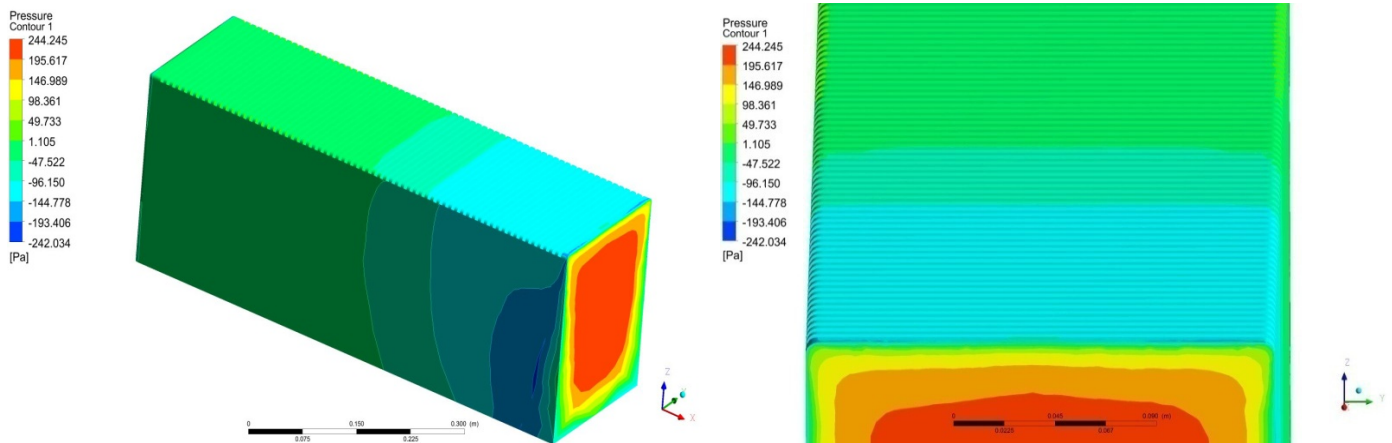
Figure 29. Systematic representations of isometric and zoomed-in frontal orientations of aerodynamic pressure distributions on the second bus model.

Figure 30. Streamline- and vector-based representations of air fluid velocity variations over the second bus model—isometric projections.

Figure 31. Logical isometric and zoomed-in frontal views of aerodynamic pressure distributions on the third bus model.
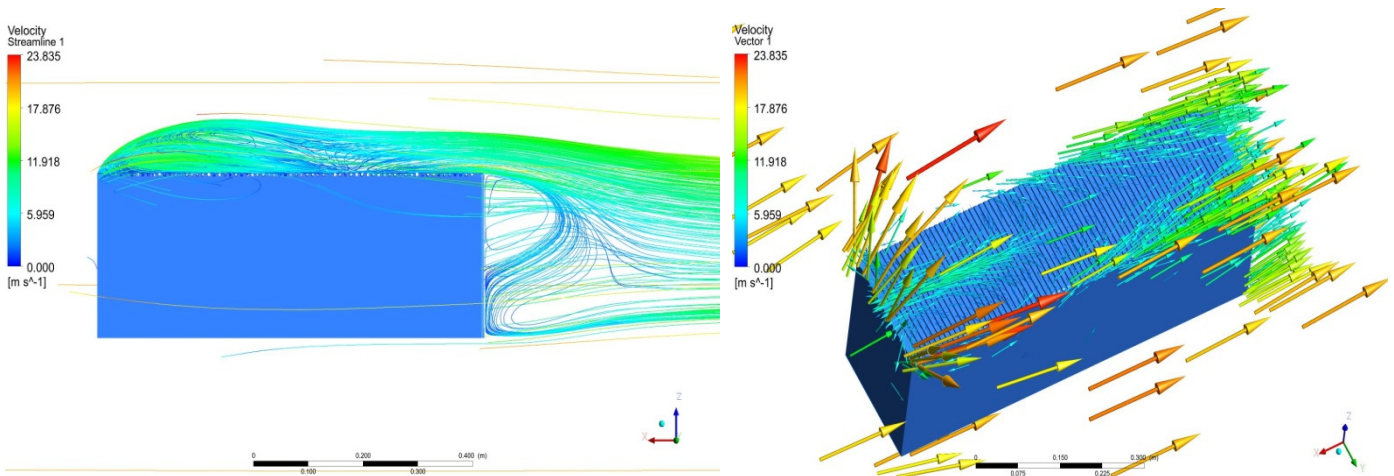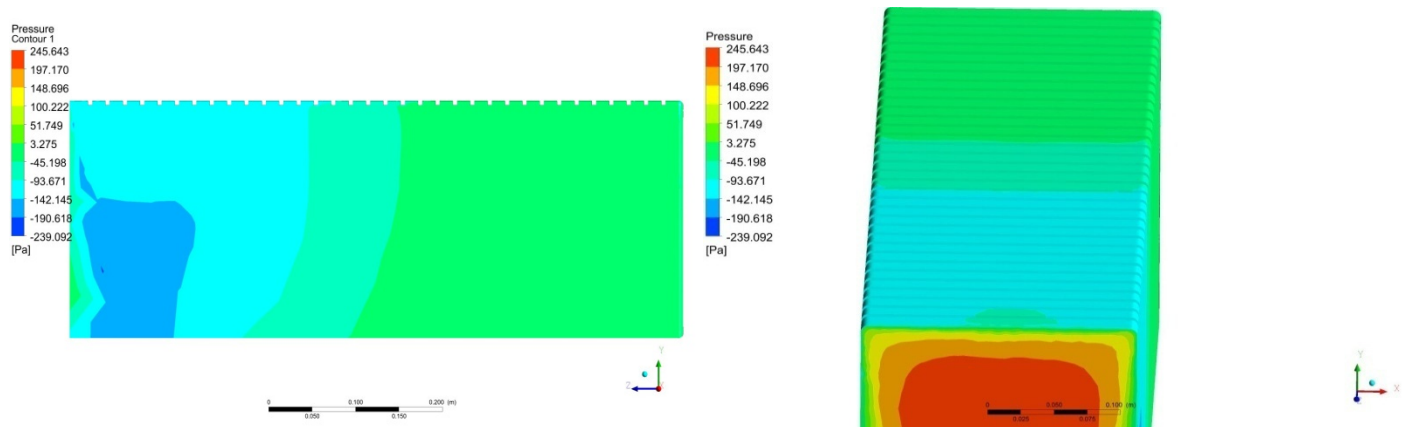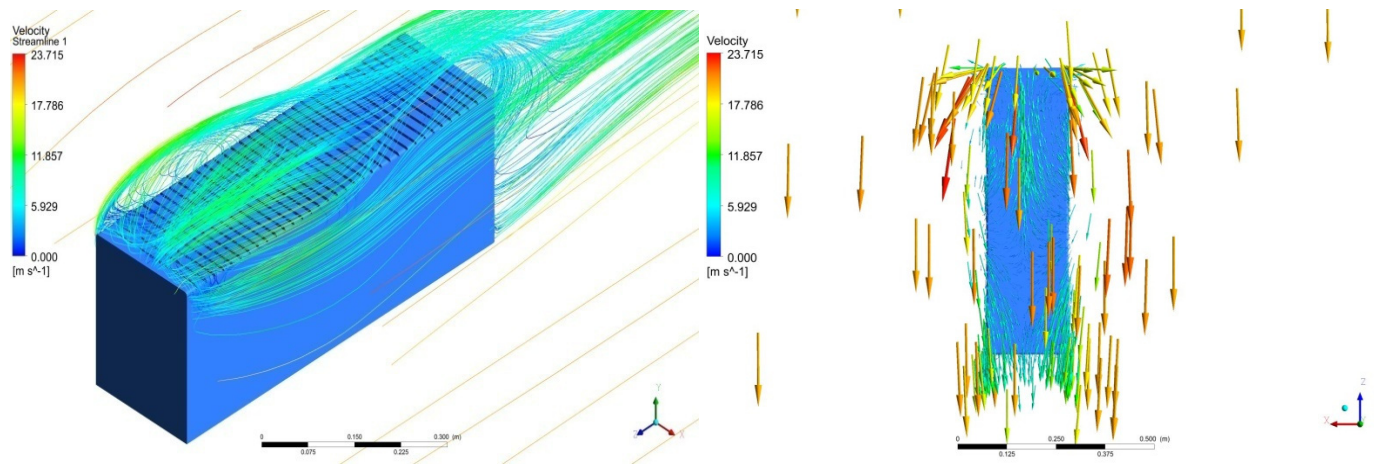
Figure 32. Streamline and vector-based representations of air fluid velocity variations over the third bus model through isometric and top projections.
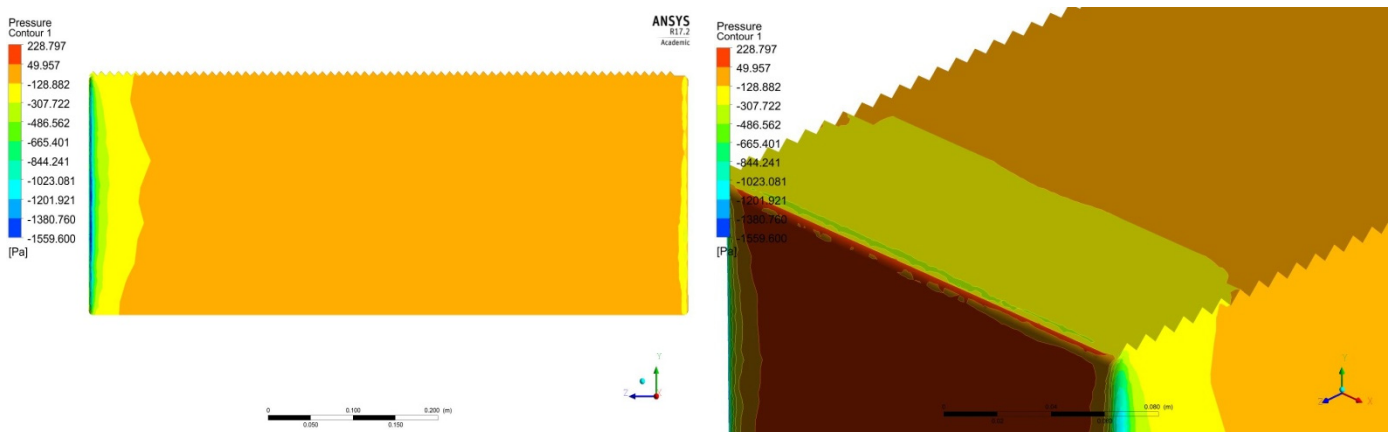

Figure 33. Emblematic side and zoomed-in frontal views of aerodynamic pressure distributions on the fourth bus model.

Figure 34. Vector- and streamline-based representations of air fluid velocity variations over the fourth bus model with the help of top and isometric projections.

Figure 35. Organized isometric and zoomed-in frontal views of aerodynamic pressure distributions on the fifth bus model.

Figure 36. Streamline- and vector-based representations of air fluid velocity variations over the fifth bus model through side and isometric projections.

Figure 37. Classic side and zoomed-in lengthwise positioned views of aerodynamic pressure distributions on the sixth bus model.

Figure 38. Streamline- and vector-based representations of air fluid velocity variations on the sixth bus model through isometric and top projections.

Figure 39. Typical side and zoomed-in isometric views of aerodynamic pressure distributions on the seventh bus model.
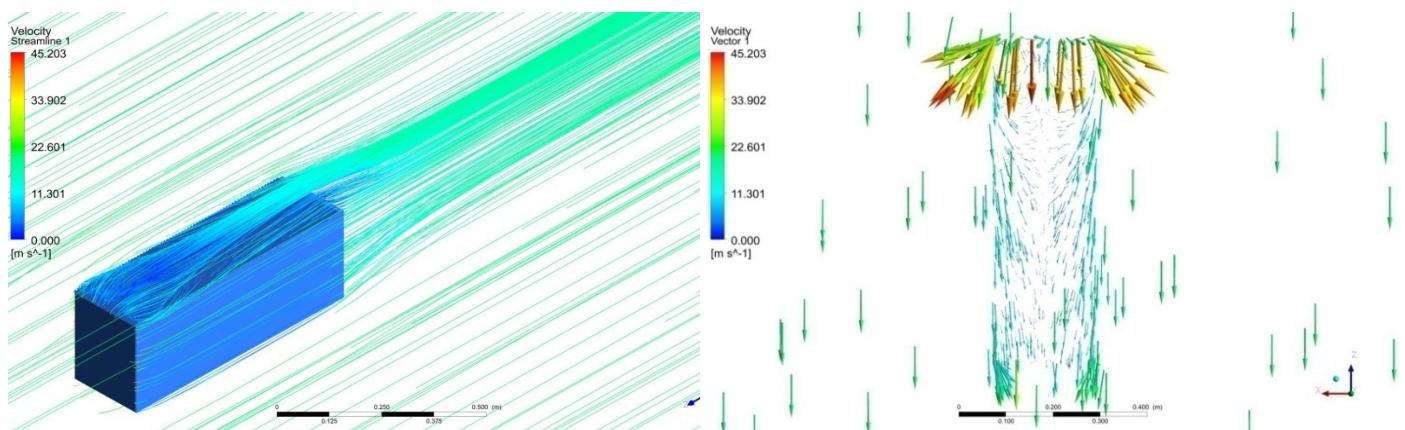

Figure 40. Streamline- and vector-based representations of air fluid velocity variations on the seventh bus model—isometric- and top-oriented projections.
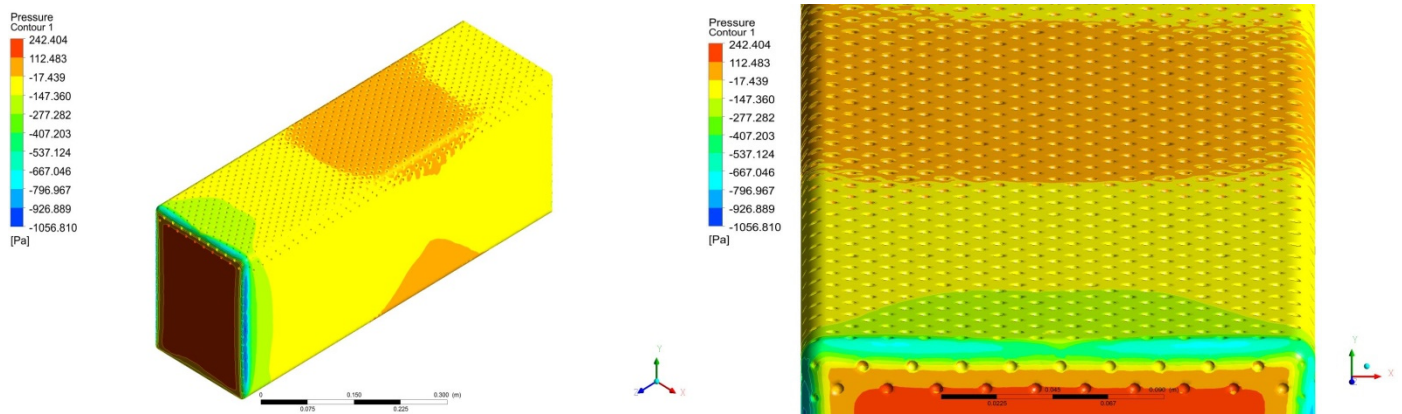
Figure 41. Characteristic views of aerodynamic pressure distributions on the eighth bus model using isometric and top-oriented projections.
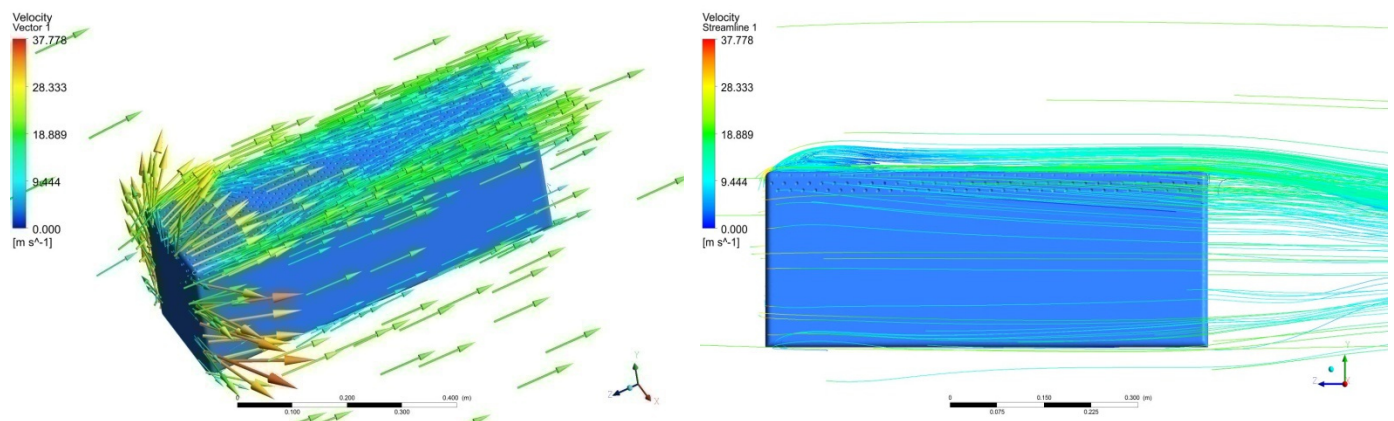

Figure 42. Vector and streamline-based representations of air fluid velocity variations on the eighth bus model.

3.1.1. Model I

Figures 27 and 28 depict the changes in aerodynamic pressure and velocity on and above the first bus model. Furthermore, the existence of dimples and their related impacts on fluid characteristics were collected and are shown in a zoomed-in view to provide further clarity. The primary findings were that the dynamic pressure fluctuations that occurred in and around the dimples lowered the high production of turbulence around these dimples.

3.1.2. Model II

Figures 29 and 30 depict the aerodynamic pressure distributions and associated velocity fluctuations of the second bus model. The imposed inverted dimples reduced dynamic pressures as well, although the decrement zones occurred exclusively near the inverted dimples. This inverted dimple did not result in a reduction in dynamic pressure at the flow separation zones; hence, this way of reducing drag is insufficient for this high-speed work.

3.1.3. Model III

Figures 31 and 32 show typical views of the aerodynamic pressure fluctuations generated on and over the third bus model. The crucial aspect to remember about this strategy is that the fluid velocities were linearly lowered in a meaningful way along the bus's longitudinal direction. This impression was caused by the continual projection of dimples on the bus's side faces.

3.1.4. Model IV

The drag reduction methodology's square-cut character influenced the conventional flow across the fourth simulated bus, as seen in Figures 33 and 34 using vector and streamline-based representations. This fourth option, like the second drag reduction result, failed to accomplish a constant velocity decrease in the bus along its longitudinal direction. Furthermore, from the base model to model IV, a distinct coordinate system was generated in which the main flow direction (drag force developing direction) is designated as the Z-direction, the upward direction is designated as the Y-direction, and the side flow direction is designated as the X-direction.

3.1.5. Model V

The fluid characteristics of 10 mm fins varied when they were utilized in the bus models, as seen in Figures 35 and 36. In terms of output production, this drag reduction strategy was undoubtedly unique in comparison to other strategies. Figure 35 shows that pressure fluctuations across the longitudinal locations of the bus significantly lowered, whereas Figure 36 shows that the induction level of eddies was significantly larger than in previous circumstances. As a result, this approach was incapable of delivering superior results. For this model, a unique coordinate system was created, with the X-direction representing the main flow (drag force-generating direction), the Z-direction representing the upward direction, and the Y-direction representing the side flow.

3.1.6. Model VI

The expanded version of fifth drag reduction was used, which was designed with a 20 mm fin gap over the bus model's top face. The primary flow was diffused and, as a result, the fluids produced the subordinate routes due to their somewhat increased length and depth-wise sections. Figures 37 and 38 depict vivid visual depictions of these fluid behaviors. This sixth strategy, like the fifth, produced more eddies, which had an impact on the bus's performance.

3.1.7. Model VII

The fluctuations in aerodynamic pressure and velocity of air particles over the riblet-equipped bus model are shown in Figures 39 and 40. This forced approach was ineffective at achieving a focused result since it generated a large number of tiny circulations.

3.1.8. Model VIII

The impact on the dimples' effect grew even more as the results of the first, second, and third bus models were seen. As a result, the eighth bus model was created using all of the aforementioned strategies. Figures 41 and 42 show typical depictions of aerodynamic pressure and velocity fluctuations across the eighth bus type. The velocity fluctuations were adjusted in a zigzag fashion due to the existence of dimples placed on the top face, which was not necessary for the targeted output. Additionally, from model VI through model VIII, a unique coordinate system was developed, with the Z-direction representing the main flow (drag force-generating direction), the Y-direction representing the upward direction, and the X-direction representing the side flow.

3.1.9. Discussion

The pressure effect and shear stress contributions, which are primary drag-generating variables in vehicle aerodynamics, were the most important aspects studied in this paper. The wake forms at separation areas were recorded by precisely meshing the flow-separating regions with the inflation setup. As a result of this, it was shown that flow wakes were also produced in drag reduction approaches, which had both advantages and problems. The main benefit is that flow velocities at flow separation places were lowered, resulting in reasonable reductions in vacuum areas forming. The velocity reductions were mostly caused by the application of different drag reduction strategies. To explore the behavior of

the skin friction drag effect on the performance effects of buses, high skin friction effects were included in the computation. Finally, Table 4 summarizes the aerodynamic forces generated by each bus type.

Table 4. Comprehensive outcome of drag generated on various bus models—forward direction.

Bus Model	Upward Force (N)	Sideslip Force (N)	Drag Force (N)
Base model	1.10147	0.29927	7.037
Model I	0.0660117	0.356574	5.76606
Model II	0.0616214	0.0105042	9.83527
Model III	1.82655	0.450884	7.49661
Model IV	0.212934	0.4451	6.5703
Model V	0.236562	0.0588171	12.0567
Model VI	0.13367	0.248186	11.836
Model VII	0.270574	0.640371	6.93219
Model VIII	1.1323	0.209187	7.0459

From Table 4, it was concluded that model I is good technique to provide low drag, and it could also have the capacity to increase the performance by means of providing high concentration on the speed of the bus instead of overcoming the opposing force.

3.2. CFD Results for Bus in Sideslip Investigation

Apart from the primary issue of intercity bus performance, passenger comfort must be maintained during the journey, especially when the bus is nearing lengthy endurance and overnight operation. The displacement of buses is one of the key causes that compromise passenger comfort. Vertical direction-based dislocation is common as a result of the existence of speed breakers and uneven road construction. The lateral direction-based dislocations occur mostly as a result of side forces caused by significant aerodynamic gust loads created naturally or intentionally by other vehicles. This work was completed in order to evaluate the influence of side forces and their reductions using the previously mentioned drag reduction approaches. As a result, nine distinct bus models were used in CFD computations in this study.

3.2.1. Model I

Figures 43 and 44 are shows the fluctuations in aerodynamic pressure and free stream velocity across the initial bus model. Figure 43 depicts the behavior of air flow in the side flow direction over an intercity bus. Figure 44 depicts the pressure outline used to calculate the drag force of the bus simulated with a higher number of dimples on the top and side surfaces, with evident changes in pressure measurements owing to the presence of dimples.

3.2.2. Model II

Figures 45 and 46 depict airflow behavior using velocity changes and aerodynamic pressure distributions over a bus modeled with inverted dimples on the top and side surfaces using velocity streamlines. Based on sideslip velocity, the given velocity in this situation was 10 m/s.

Figure 46 shows that dynamic pressure fluctuations occurred for these inverted dimple cases as well, albeit at a much slower rate than for other regular dimple cases. This approach is no longer suitable for reducing the sideslip impact.

3.2.3. Model III

Figures 47 and 48 show the frontal view of dynamic pressure fluctuations over bus model III, as well as the rear view-based turbulence formations.
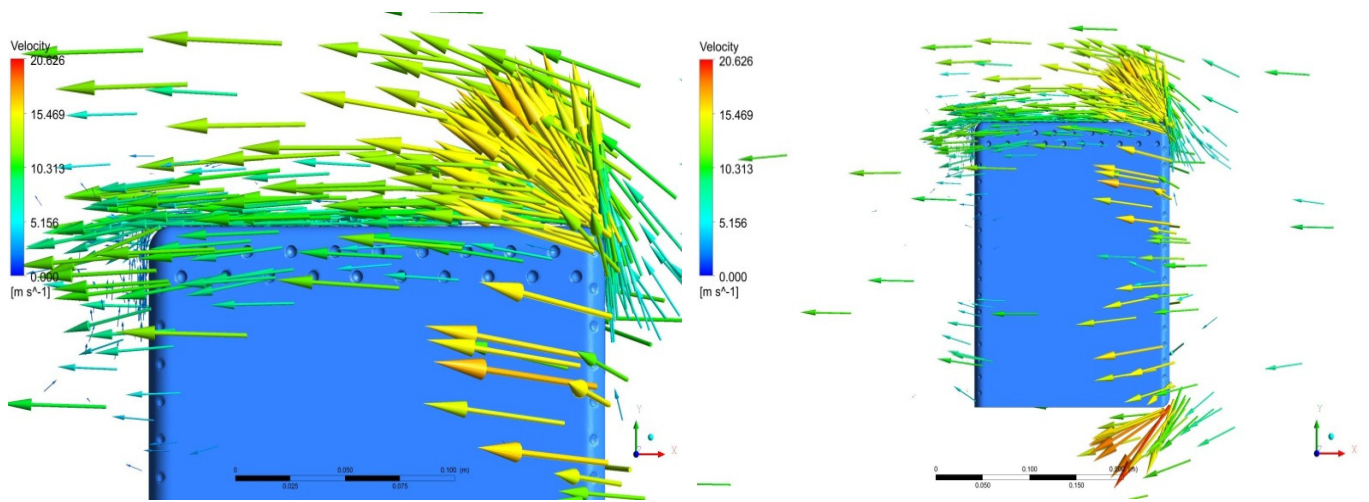
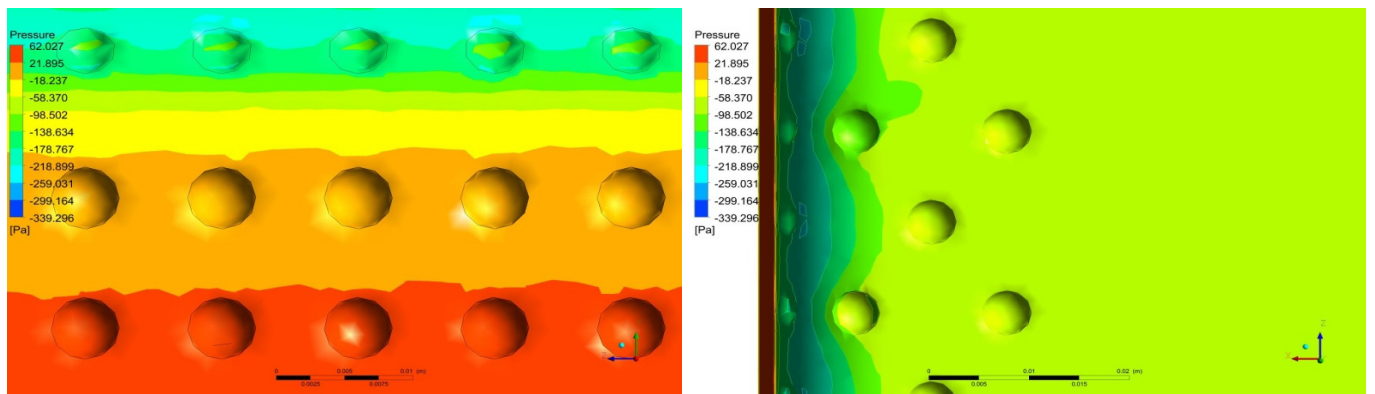**Figure 43.** Representations of sideslip flow velocity distributions over the first bus model.

Figure 44. Representations of the dynamic pressure decrement in the presence of dimples in the first model.
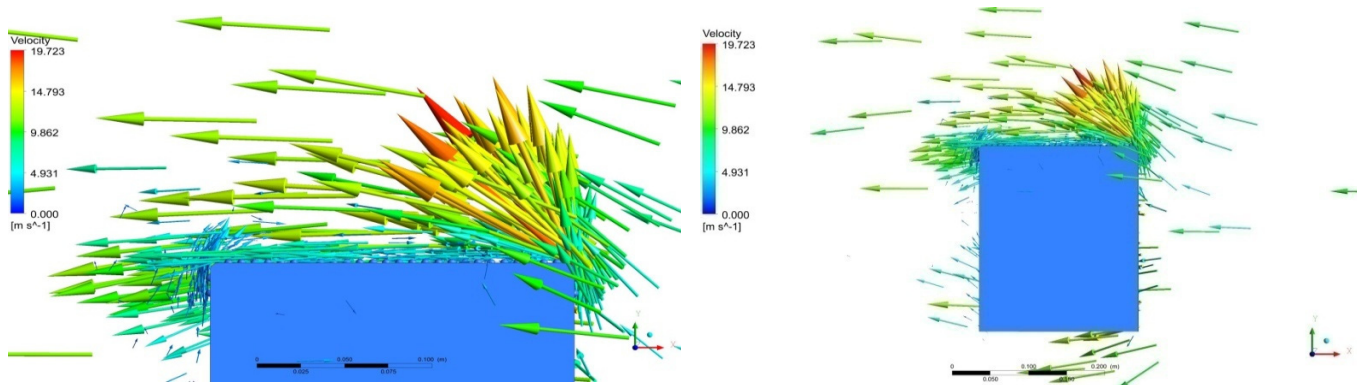

Figure 45. Systematic views of velocity distributions over the second bus model.
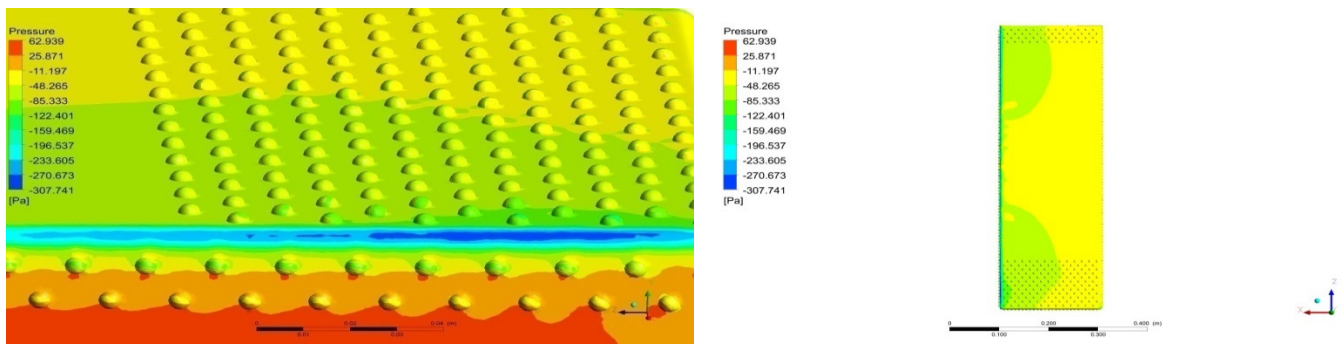
Figure 46. Archetypal views of dynamic pressure variations over the inverted dimples loaded on the bus surfaces.
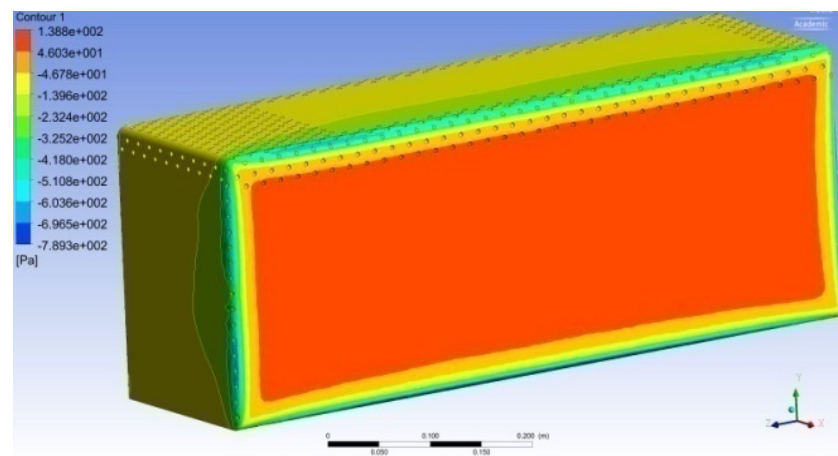

Figure 47. A typical isometric view of pressure variations on the third bus model.
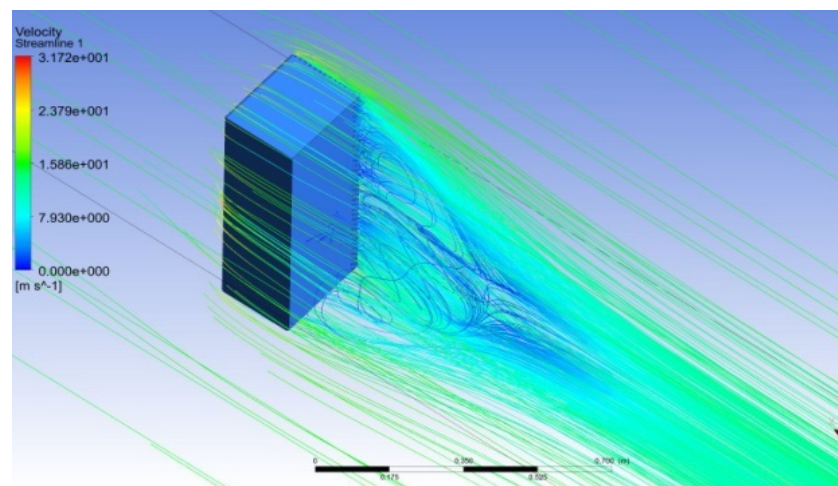
Figure 48. Streamline-based isometric representation of velocity distributions over the third bus model.

Figure 47 shows that aerodynamic pressure decrements transpired in the initial stage of the top surfaces and so remained constant on the same surfaces. This effect was designed to prevent undesirable disruptions in the direction of sideslip. Figure 48 shows that the turbulence production was relatively high in this scenario. This extreme turbulence was characterized by the lack of dimples. As a result, the dimples must be expanded, which is the main result of this third approach.

3.2.4. Model IV

Figures 49 and 50 show the different stagnation point-based portrayal of dynamic pressure fluctuations across the fourth bus model, as well as the rear view-based turbulence forms.
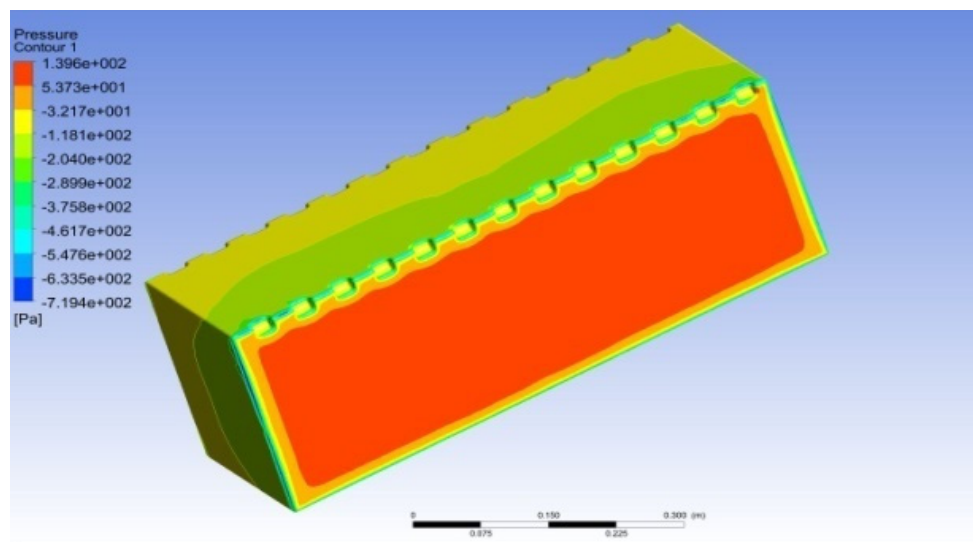

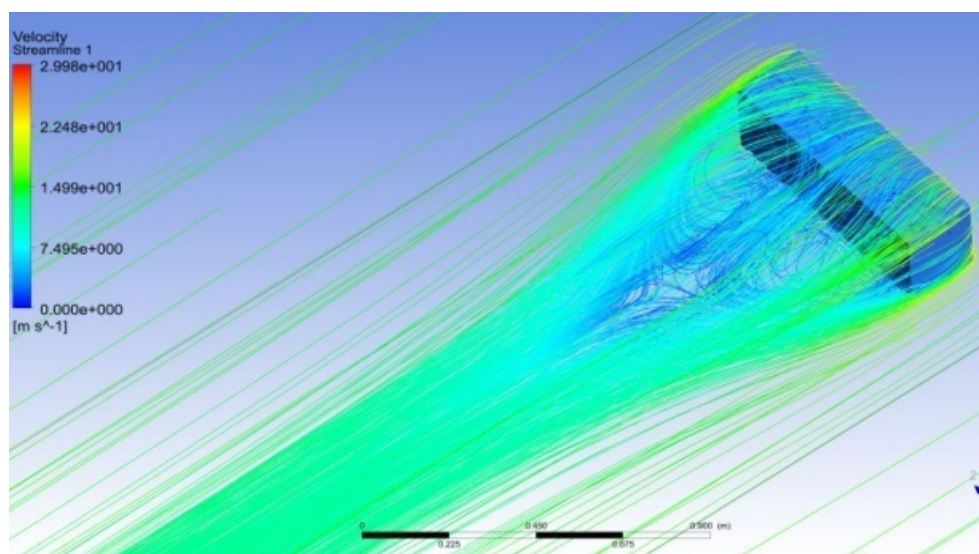**Figure 49.** Typical isometric view of pressure variations on model IV.

Figure 50. Typical representation of velocity distributions over model IV.

Turbulence was heavily created in the rear regions of this bus model, and aerodynamic pressure decrements occurred slowly throughout the top surface of the bus in the lateral directions. As a result, each of the aforementioned problems can undoubtedly diminish bus comfort.

3.2.5. Model V

An idiosyncratic stagnation point-based view of dynamic pressure variations over the fifth bus model and representations of the turbulence formations through isometric projection are revealed in Figures 51 and 52, respectively.
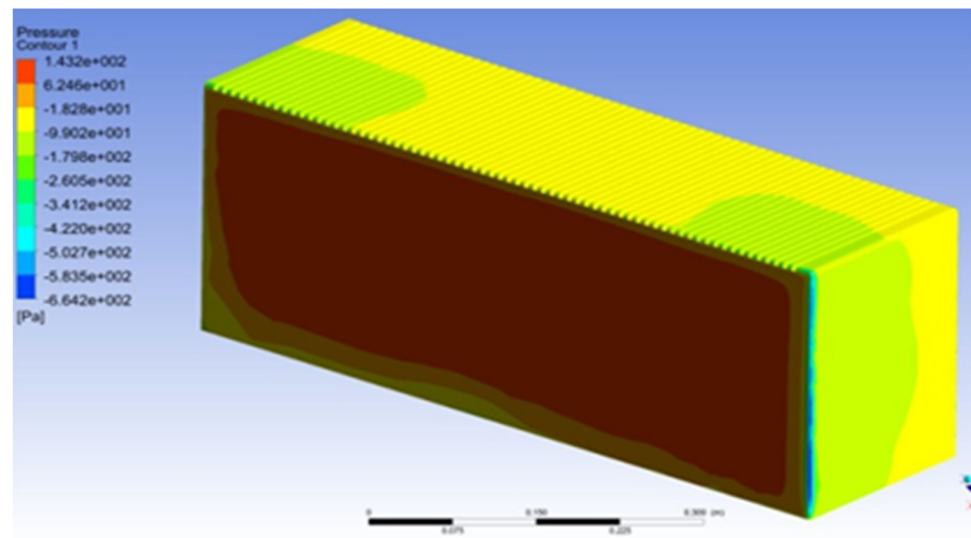
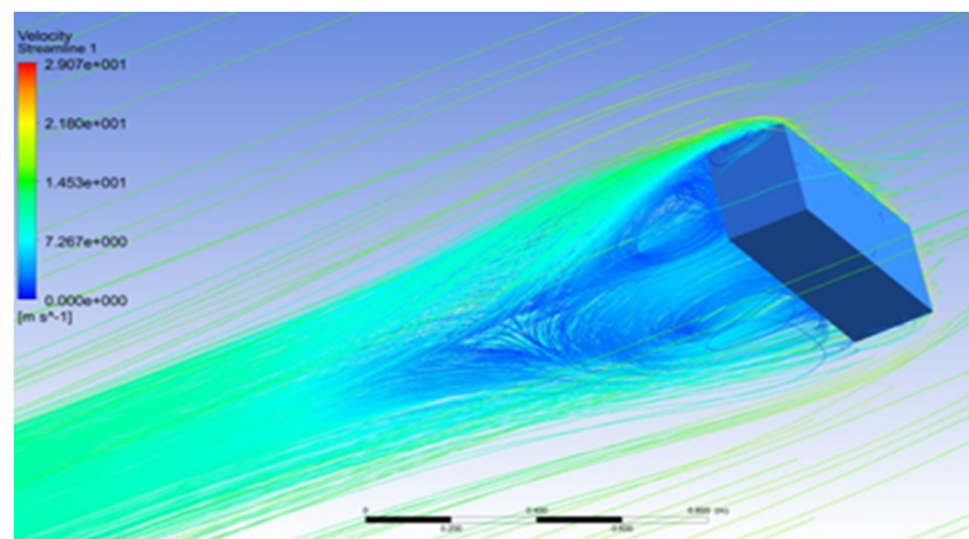**Figure 51.** Typical isometric view of pressure variations on model V.

Figure 52. Typical representation of velocity distributions over model V.

The fifth bus model, like the fourth bus model, had a lot of turbulence at the back. Aerodynamic pressures decreased on the bus's top surface occur in a non-linear and unimportant manner in the lateral directions. As a result, each of the aforementioned problems potentially jeopardizes bus comfort.

3.2.6. Model VI

Figures 53 and 54 demonstrate computed and presented isometric projection-based depictions of aerodynamic pressure on the bus and variations in speed through streamlines across the vehicle.

Because the fifth bus model was found to be too flabby to provide comfort at high gust loads, an extra fin design-based method was applied, resulting in an enlarged version in the sixth bus model. However, the same drawbacks existed and will continue to exist in this sixth bus type.

3.2.7. Model VII

Figures 55 and 56 show the fluctuations in aerodynamic pressure and free stream velocity across the seventh bus model. Figure 55 depicts the behavior of air flow in the side

flow direction over the region. Figure 56 properly depicts the pressure map used to calculate the drag force of the bus simulated with a higher number of fins on the top surfaces.
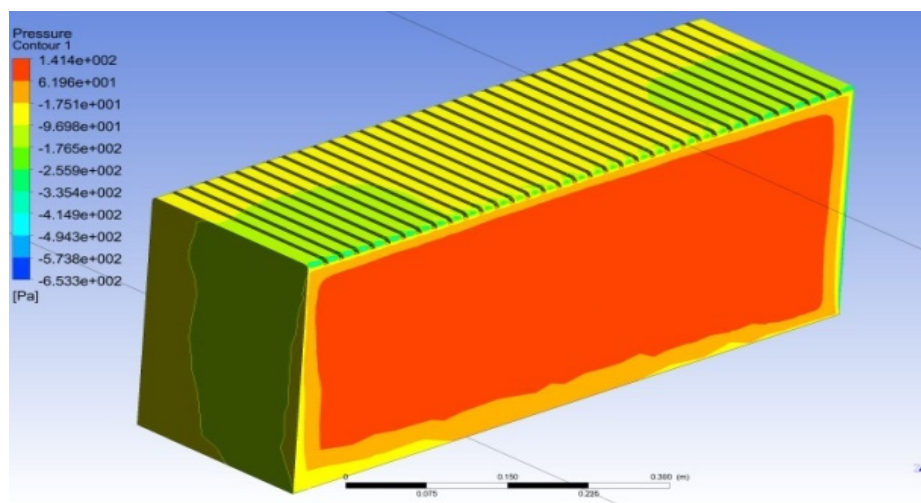

Figure 53. Typical isometric view of pressure variations on model VI.
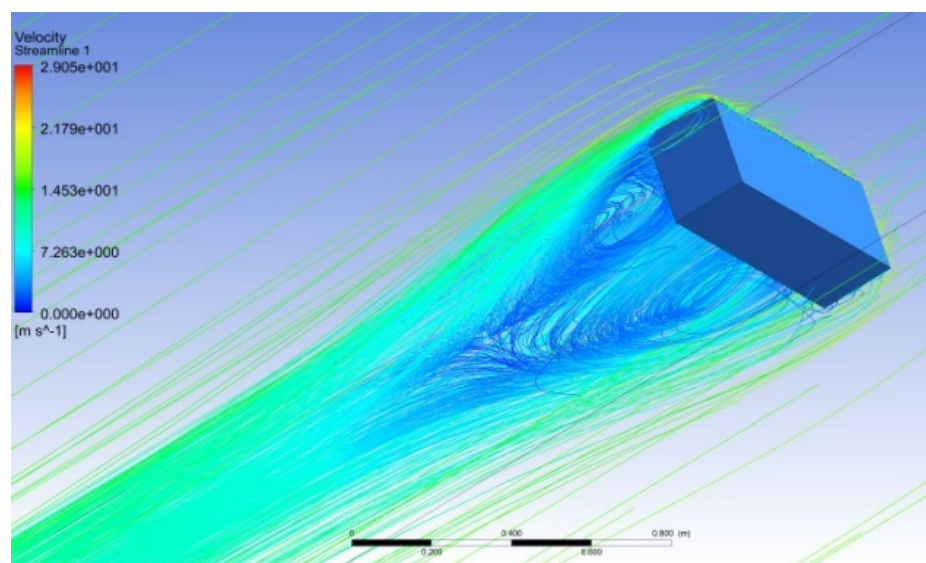

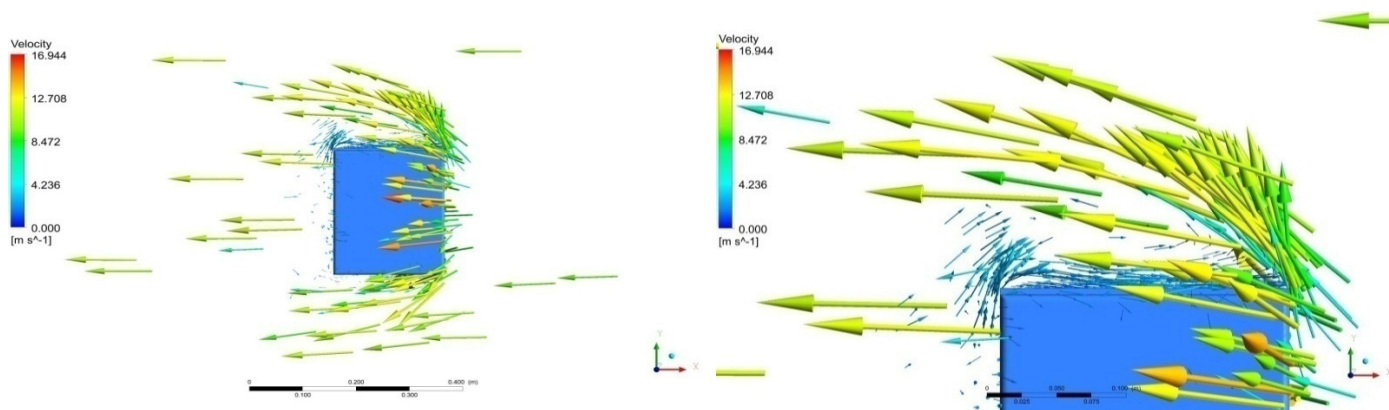**Figure 54.** Typical representation of velocity distributions over model VI.

Figure 55. Systematic views of velocity distributions over bus model VII.
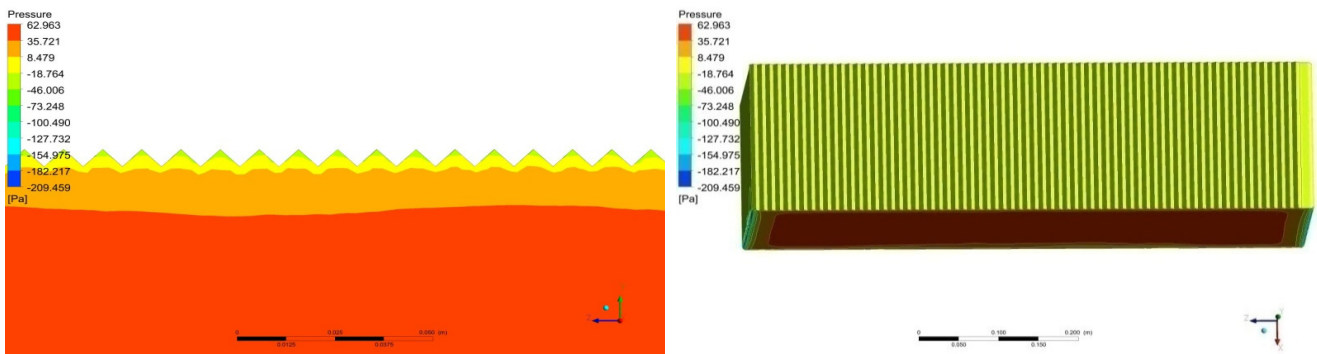
Figure 56. Representative views of dynamic pressure variations over the fins loaded on the bus surfaces.

3.2.8. Model VIII

Figures 57 and 58 demonstrate the velocity-relayed airflow behavior and aerodynamic pressure distributions across the bus, simulated with a medium number of dimples on the top and side surfaces, using a velocity vector and a pressure map.
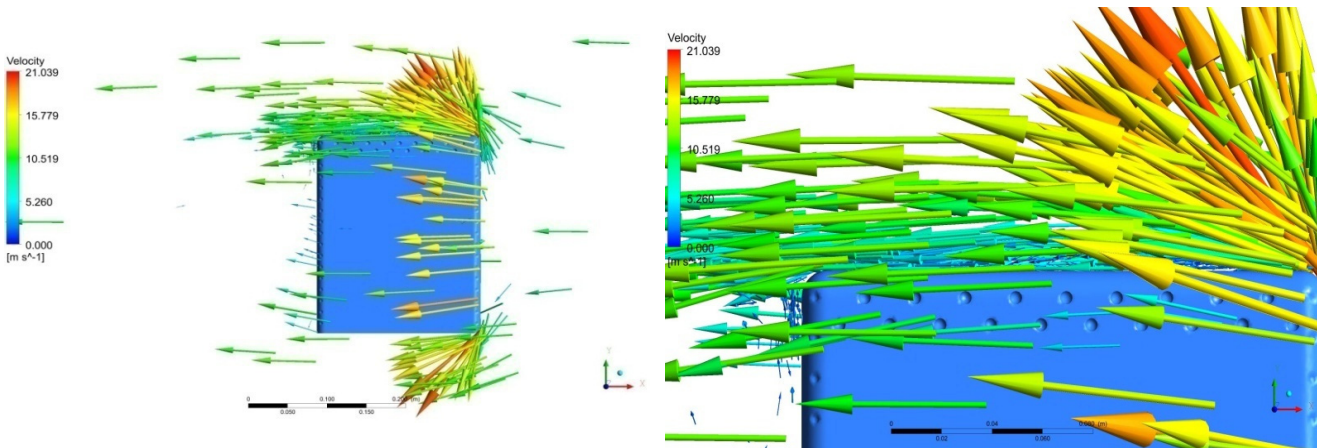

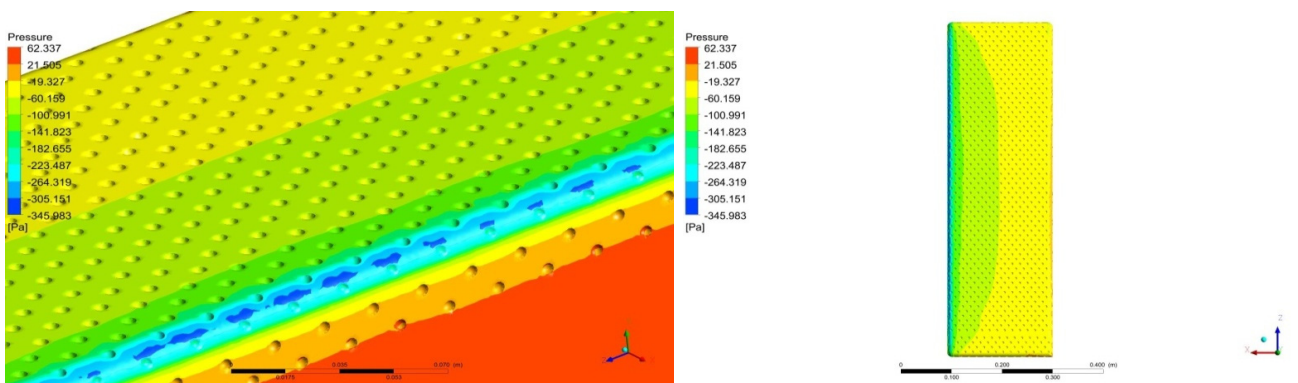**Figure 57.** Systematic views of velocity distributions over bus model VIII.

Figure 58. Exemplary views of dynamic pressure variations over the dimples loaded on the bus surfaces.

Although similar to the dimple cases, this model also performed better than other non-dimple-based models. In this case, the bus's breadth-wise position was chosen as the main air flow direction. This means that the dimples on the top faces of the bus acted as drag reducers more than in other models. In Figure 58, it was observed that the aerodynamic velocities were initially increased and, afterwards, they started swallowing

the kinetic energy of the fluid. Thus, the drag in the sideslip direction was reduced in a considerable manner.

3.2.9. Discussion

In comparison with the base bus model, the outcomes of all three scenarios for eight models are reported. For varied crosswind velocities, Table 5 compares the side force on various models.

Table 5. Comparison of side forces on various bus models.

Intercity Bus Models	Side Force Value in "Newton"		
	Crosswind Velocity (5 m/s)	Crosswind Velocity (10 m/s)	Crosswind Velocity (15 m/s)
Base model	2.40392	9.18491	20.2098
Model I	1.35382	6.41537	13.7896
Model II	2.71512	11.3569	25.3571
Model III	1.42998	6.6384	14.2063
Model IV	1.39427	9.72601	21.5342
Model V	3.08994	12.4983	28.2582
Model VI	3.03373	12.4949	27.9074
Model VII	2.93207	13.1211	29.4811
Model VIII	1.30671	5.95073	12.8353

Model VIII emerged as the best model from the comparative analyses due to its low side force induction. For side force velocities of 5 m/s, 10 m/s, and 15 m/s, the dimple model (model VIII) reduced side force by 54.35%, 64.79%, and 63.51%, respectively, compared to the base model. The model VIII intercity bus is equipped with dimples on the upper surface to help prevent turbulence from developing. In general, dimples can reduce fluid velocity; as a result of this lowered velocity, flow separation at geometrical changes, such as the meeting zone of the top and side surfaces, is reduced. The speed of the crosswind is lowered due to the presence of dimples at the appropriate locations on the sides of the bus model, which minimizes pressure drag and hence side forces.

3.3. Aerodynamics Investigations on the Optimized Bus for Civilian Use

From Tables 4 and 5, the greatest performers were model I and model VIII, both of which are equipped with the recommended dimple-based approach. As a result, deployment-based section considerations were used to select the optimal option between model I and model VIII. The application of dimples over the bus was easier in model I than in model VIII, and the sideslip force was somewhat higher in model I, so model I was chosen to offer high efficiency.

Figures 59–63 show the final intercity bus models that were modified and based on real-time implementation. Figure 63 is the most important result of these comparative studies since it shows the biggest decrease in aerodynamic drag and its associated impacts. First, CFD studies were calculated over the final and complete bus model in a multi-parametric study of the full bus model, and it was noticed that no harmful creation factors were formed on this final offered idea.

Aside from the computing platforms, the volumes of all bus types are clearly shown in Figures 59–63. Aluminum alloy 5052 is one of the lightest materials used in the building of intercity buses; hence, it is heavily engaged in the estimating mass of this vehicle. The density of the tire rubber and passenger details play a significant role in determining the total mass of the vehicle. Incompressible flow-based CFD analyses were computed on five different models based on the boundary conditions mentioned above, including the base bus model that does not contain dimples, the bus model equipped with dimples 30 mm in sized, the bus model equipped with dimples 50 mm in size, the bus model equipped with dimples 75 mm in size, and the bus model equipped with dimples 100 mm in size.

Figures 64–73 show the aerodynamic pressure distributions and speed changes for the above five examples.

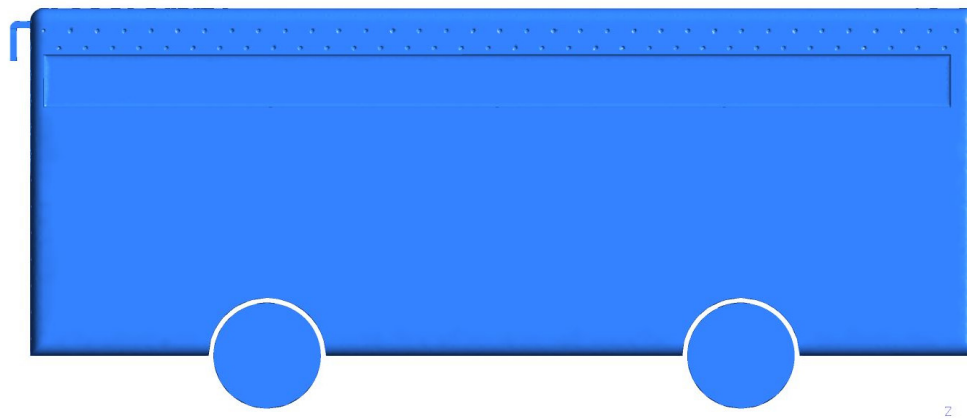**Figure 59.** Systematic top view-based representation of an intercity bus without dimples (base model).

Figure 60. Typical side view of an intercity bus loaded with 30 mm dimples in the optimized regions.
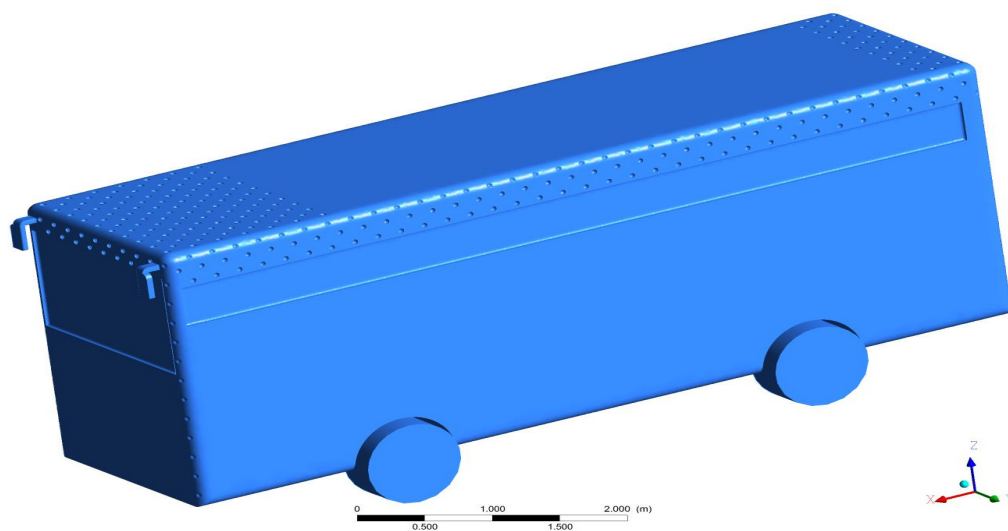

Figure 61. Typical isometric representation of a bus equipped with 50 mm dimples in the optimized regions.
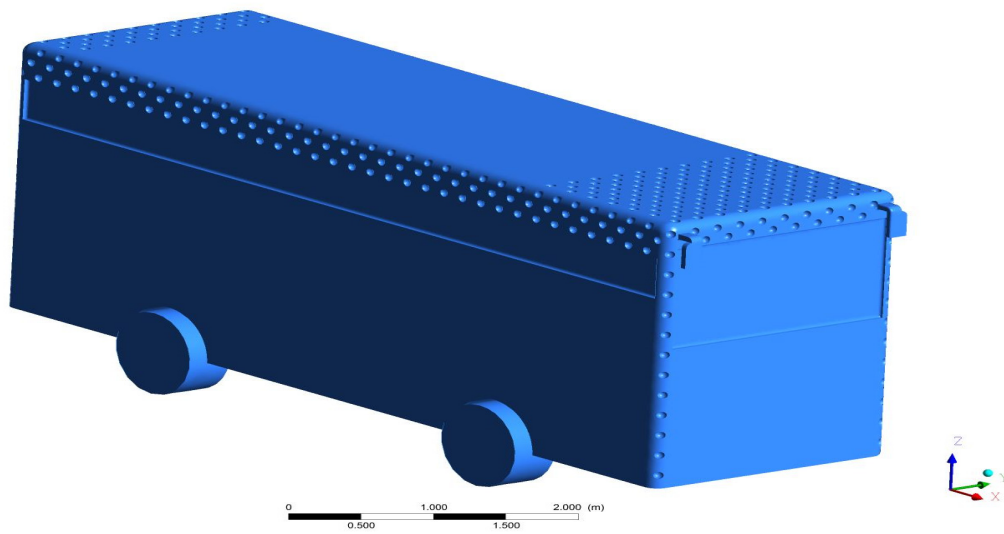
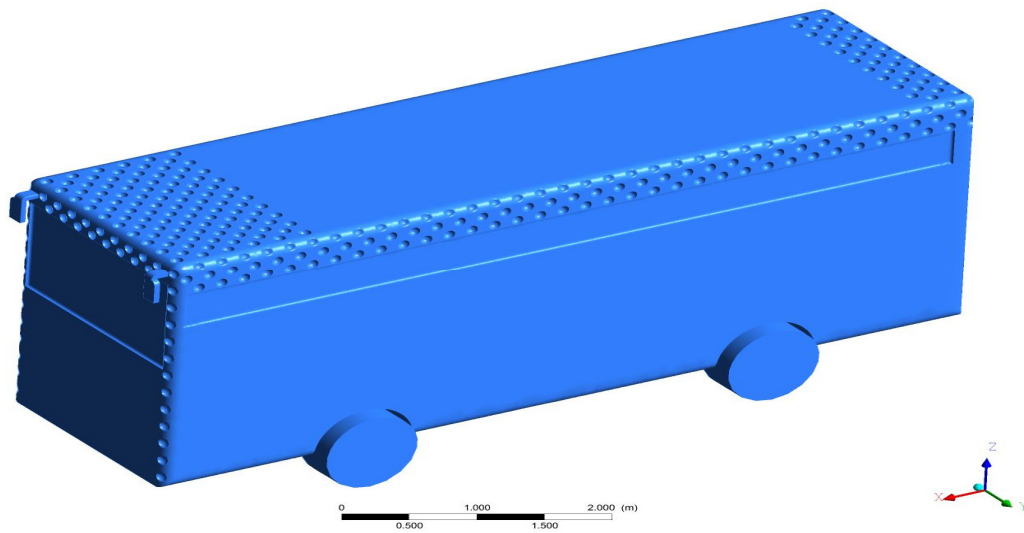**Figure 62.** Typical isometric representation of a bus equipped with 75 mm dimples in the optimized regions.

Figure 63. Typical isometric representation of a bus equipped with 100 mm dimples in the optimized regions.
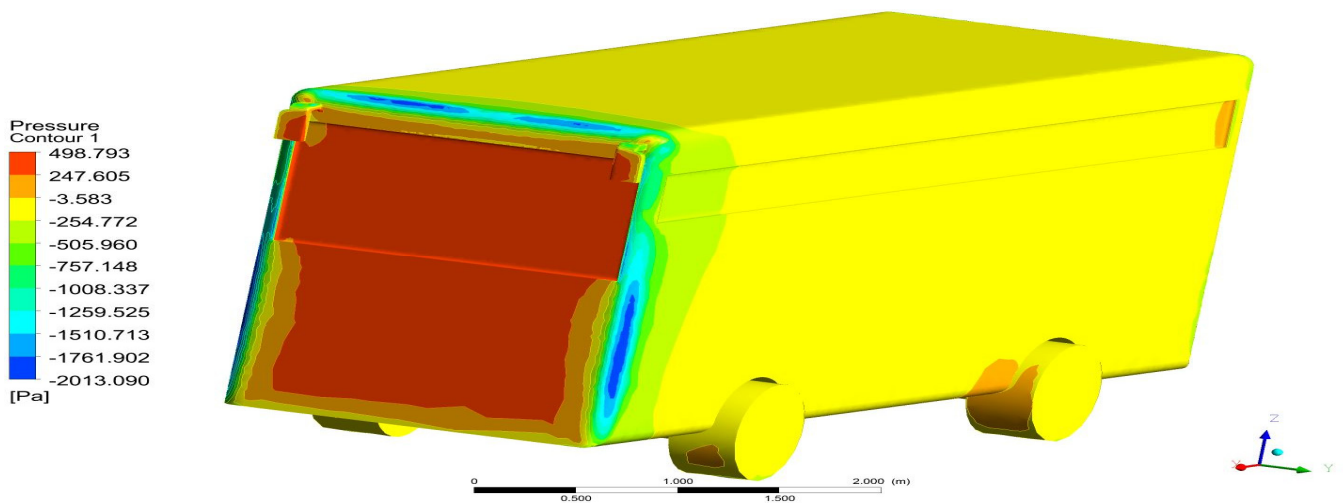

Figure 64. Aerodynamic pressure variations on the base bus model—isometric view-based representation.
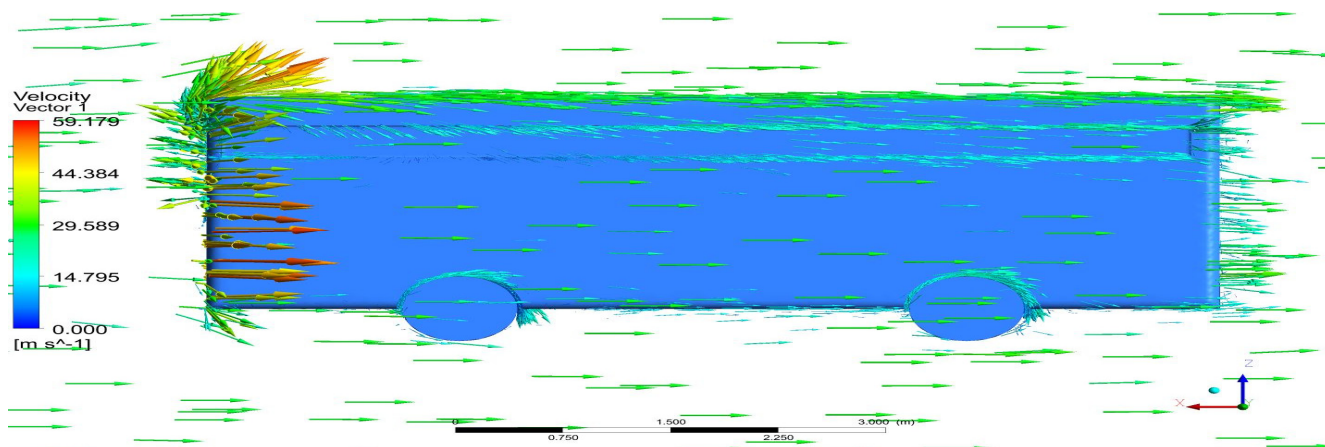
Figure 65. Aerodynamic fluid velocity variations over the intercity bus through vector-based projections.
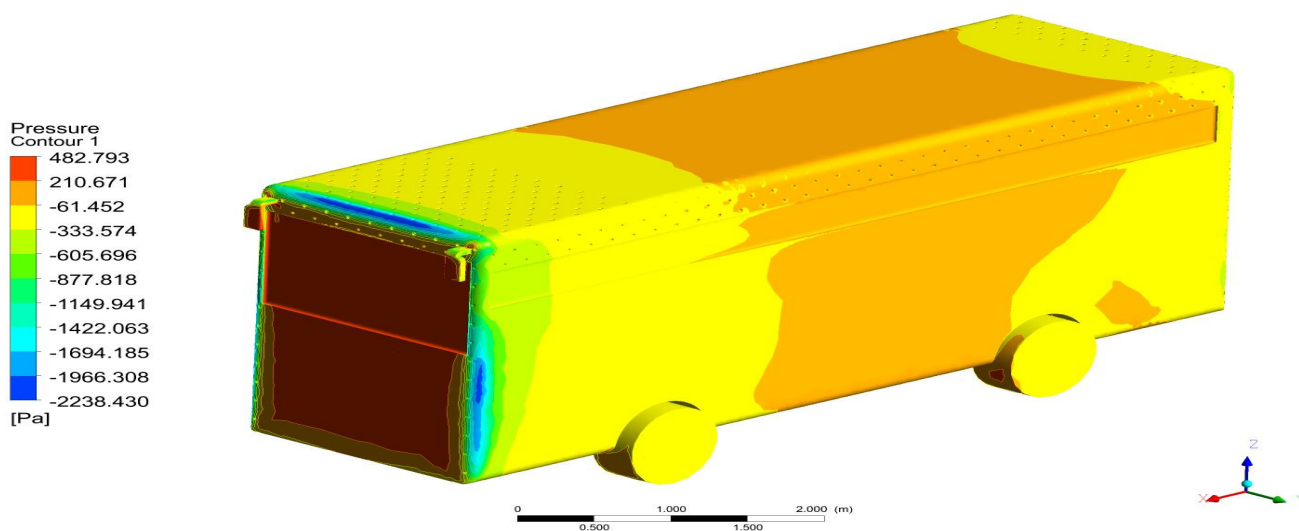

Figure 66. Typical projection of pressure distributions on the intercity bus loaded with 30 mm dimples.
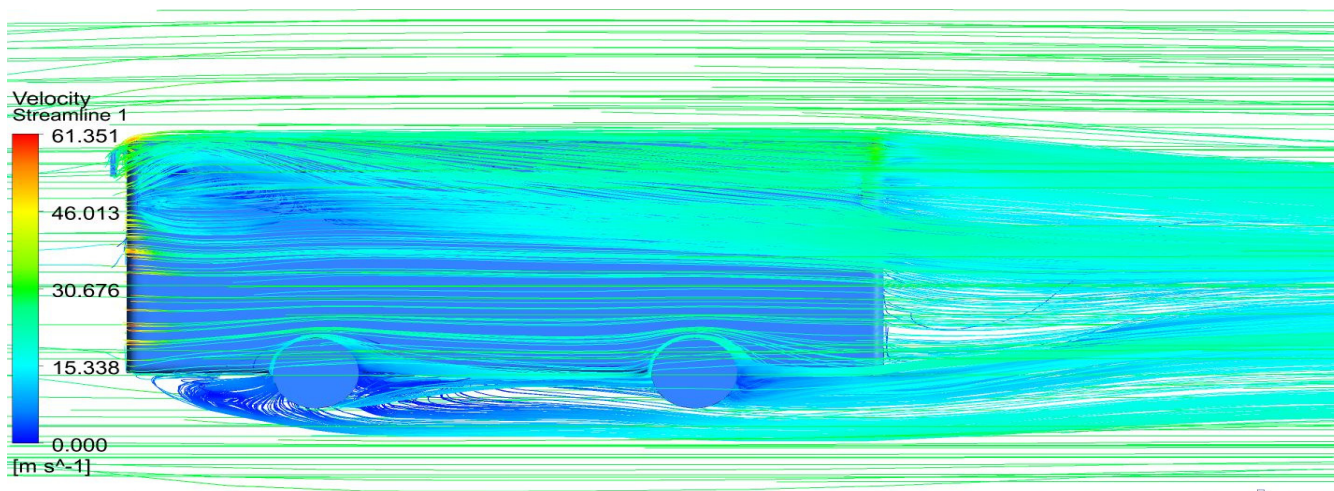

Figure 67. Velocity variations over the intercity bus loaded with 30 dimples through streamline-based projections.

Figure 68. Aerodynamic pressure variations on the bus model equipped with dimples 50 mm in size—isometric view-based representation.

Figure 69. Aerodynamic velocity distributions over the bus model equipped with dimples 50 mm in size—side view-based representation.

Figure 70. Aerodynamic pressure variations on the bus model equipped with dimples 75 mm in size—isometric view-based representation.

Figure 71. Aerodynamic velocity distributions over the bus model equipped with dimples 75 in size—side view-based representations through streamline mode.
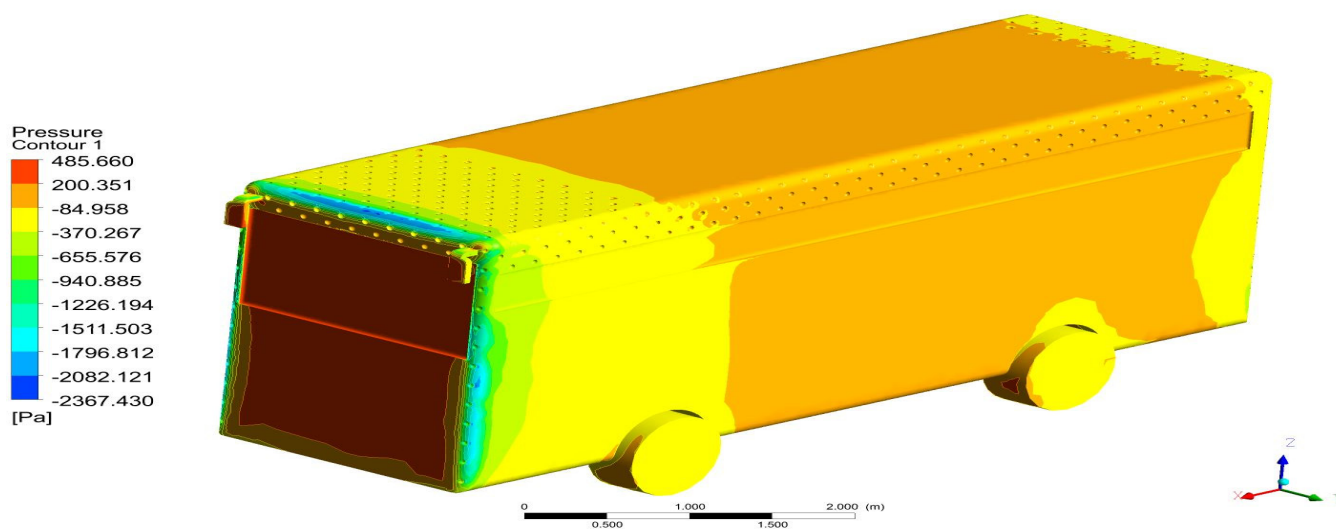

Figure 72. Aerodynamic pressure variations on the bus model equipped with dimples 100 in size—isometric view-based representation.

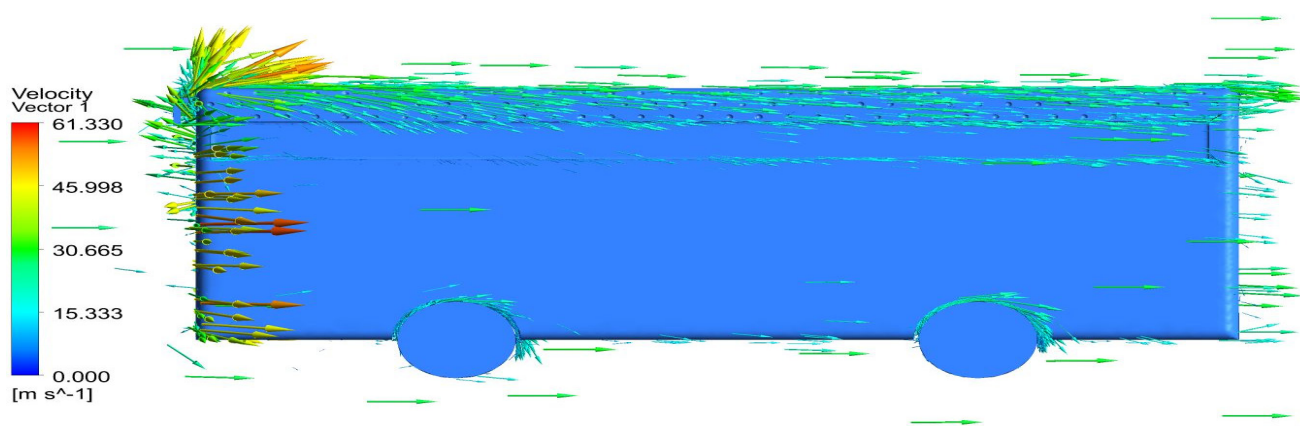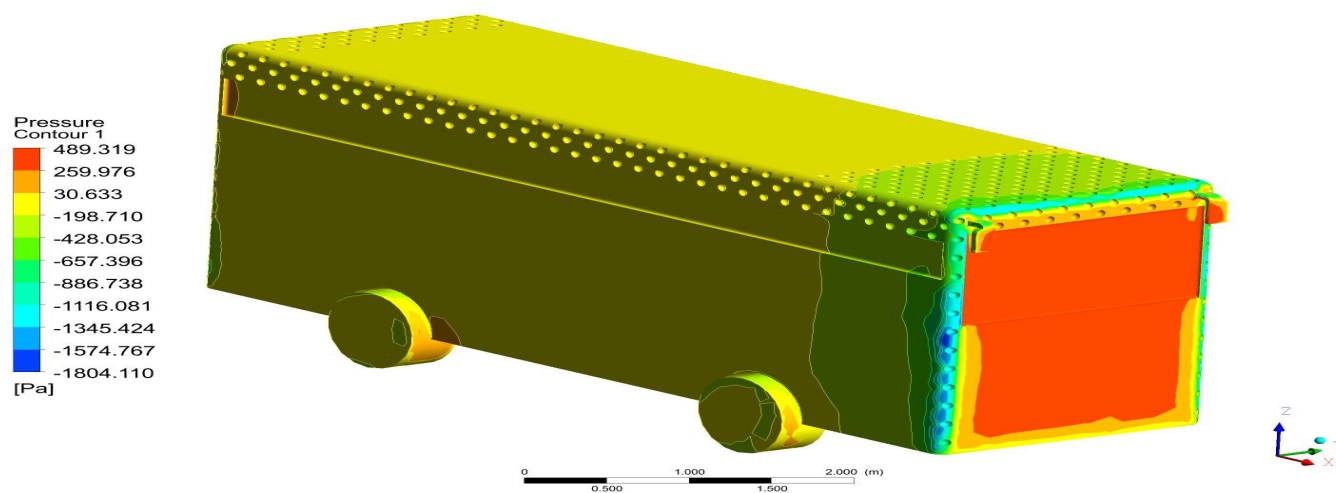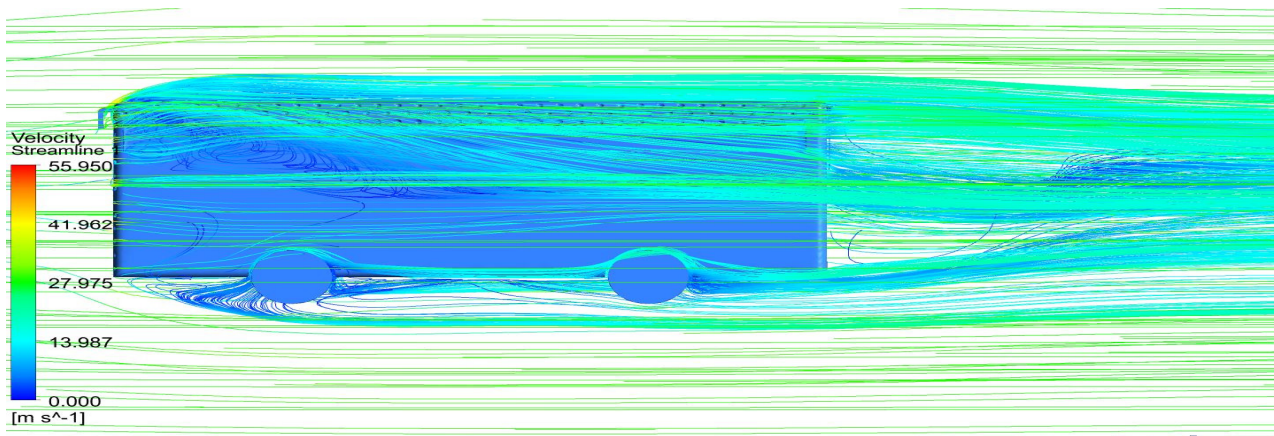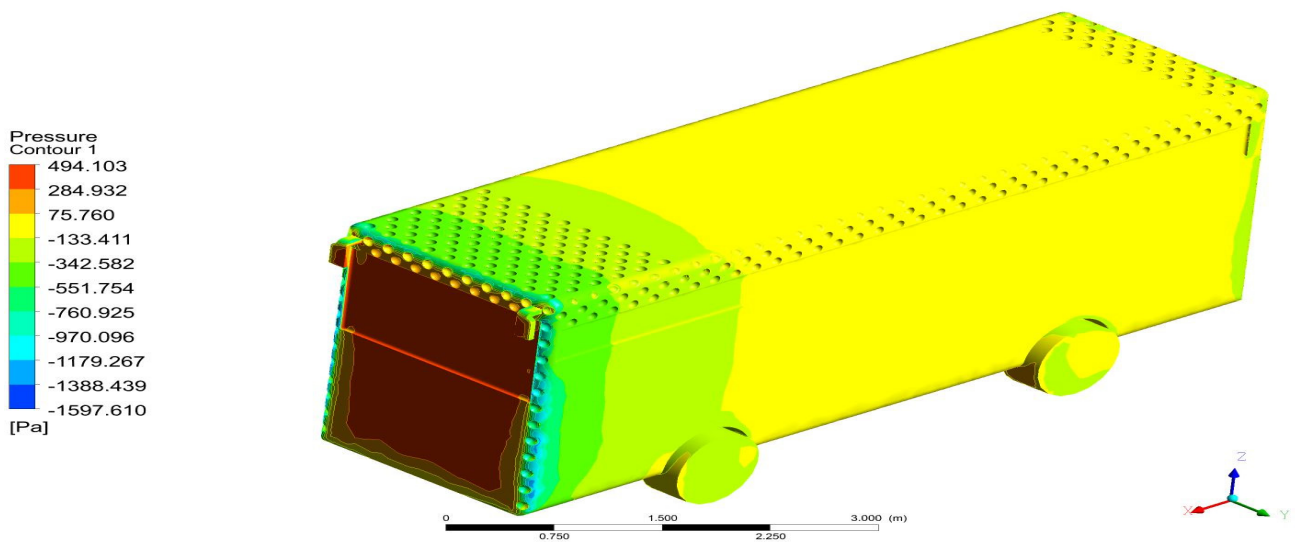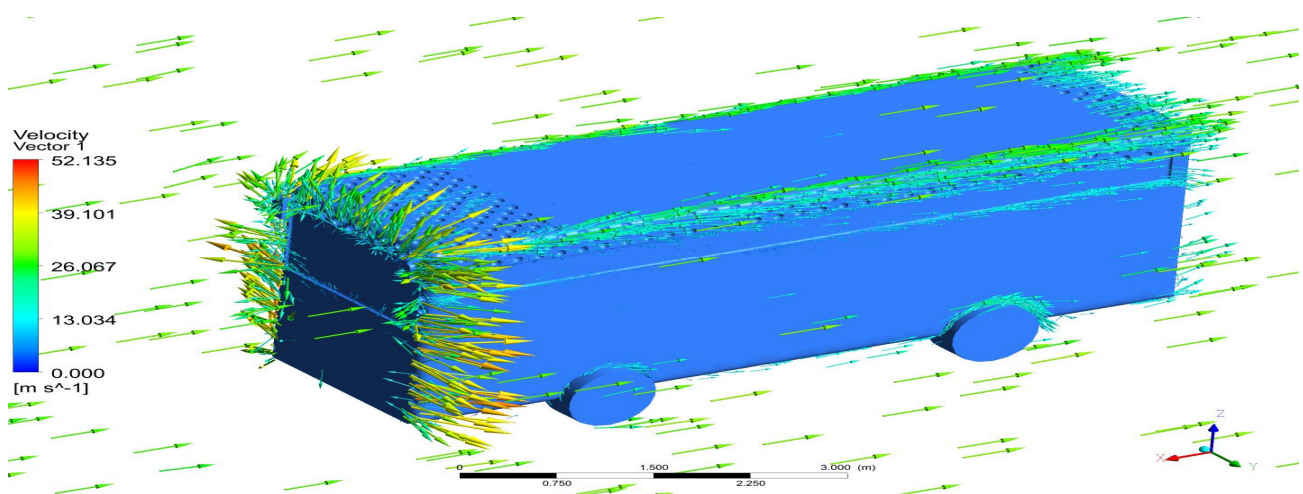**Figure 73.** Velocity variations of the intercity bus loaded with 100 mm dimples at the speed of 100 km/h.

The 30 mm dimple-equipped bus model induced lower drag force than all other models, whereas the 100 mm dimple-loaded bus model caused less extra opposing forces than other cases, as seen in Figures 64–73 and Table 6.

Table 6. Comprehensive aerodynamic forces on and over the optimized civilian intercity buses.

Bus Models	Drag (F_D) (N)	Upward Force (N)	Side Slip Force (N)	Induced Velocity (m/s)
Base bus model	1560.44	23.9324	114.237	59.179
30 mm dimple-loaded bus model	1550.41	0.940451	80.7699	61.351
50 mm dimple-loaded bus model	1574.78	42.3091	36.5971	61.330
75 mm dimple-loaded bus model	1806.74	30.8007	49.8049	55.950
100 mm dimple-loaded bus model	1904.09	16.3635	57.0211	52.135

3.4. Comprehensive Analyses of Energy Essential to Conquer External Resistances

To complete this investigation, the real-time performance of influencing and creating factors on the proposed equipped bus model concept needed to be checked, so a detailed literature survey [30] was conducted, wherein the focused parameters noted were the energy of the automotive engine, which required tackling the resistance force of the bus; the fuel consumption rate of the bus; the specific power of an intercity bus; the coefficient due to resistance; and the mechanical efficiency of the bus. Equations (11)–(19) were developed from pertinent fieldwork knowledge [30].

$$E_R = \int_0^D \left(\frac{F_{Forward}}{\eta_m \times t} \right) d(D) \tag{11}$$

It is evident from Equation (11) that estimating the required forward force to move the desired intercity bus is a necessary factor that has been factored into the computation of the automobile engine's required energy level. As a result, the significant components were examined and afterwards enforced in the relationship of the forward force needed to move the intended intercity bus, as shown in Equation (12).

$$F_{Forward} = F_{RR} + F_D + F_{IB} + F_M + F_A \tag{12}$$

The first contributor to the required forward force is the force generated due to the effect of rolling resistance. The rolling resistance force comprises the amount of pressure supplied to the tires, the forward speed of the intercity bus, gravitational force, and the gross mass of the intercity bus. The suitable relationship for the force required to oppose rolling resistance is incorporated in Equation (13).

$$F_{RR} = m \times g \times C_t \tag{13}$$

A conventional relationship may be used to compute the rolling resistance term coefficient of automotive vehicles, as indicated in Equation (14).

$$C_t = 0.005 + \left[\left(\frac{1}{P_T} \right) \times \left(0.01 + \left(0.0095 \times \left(\frac{V_B}{100} \right)^2 \right) \right) \right] \tag{14}$$

According to the literature review [27], the tire pressure attained is 8 bars, and the maximum velocity imposed on this intercity bus is 100 km/h. Thus, using Equation (14), the rolling resistance term coefficient was calculated to be 0.0074375. A second source of the F_{RR} is Equation (15), which explains how inertia can create force on the bus.

$$F_{IB} = m \times a \tag{15}$$

According to traditional real-time measurements, the acceleration of moving vehicles is primarily determined by two factors: the vehicle's induced velocity and its endurance to finish the task. The velocities caused by the optimized bus models were estimated using the CFD technique for these extensive investigations. Because dimple impositions can certainly assault the traditional formations of aerodynamic velocity over the bus, CFD was employed at this point. Table 6 shows the collected results of all the induced velocities across the optimized bus models. The third source of FRR was the force imparted on the bus as it performs various turning maneuvers. The connection of maneuvering forces is represented in Equation (16).

$$F_M = m \times g \times \sin(\alpha) \tag{16}$$

The authors defined maneuvering in this study as the execution of different turning actions by an intercity bus. The major activity highlighted in this study is the intercity bus's continuous level flight; hence, the force necessary to counteract the bus's turning movement is ignored. In addition, the writers finish the turning actions of the bus in a future work. Furthermore, CFD successfully computed side forces in both vertical and lateral orientations. Table 6 summarizes the total estimated extra forces. Drag caused by pressure imbalance and skin friction effects was the most significant and inevitable contribution to this FRR. Equation (17) reveals the standard drag force connection.

$$F_D = 0.5 \times \rho_a \times (V_b)^2 \times C_D \times A \tag{17}$$

From Figures 64–73 and Table 6, it is clearly observed that the CFD approach was imposed on the perfect estimation of various aerodynamic forces on and over the optimized intercity bus models. Thus, the values of drag force (F_D) for all the cases were determined through the CFD approach. Finally, the other forces contributing to the performance affecting factors were sideslip forces due to crosswind and upward forces due to the profiles of the buses. Along with the terms mentioned in Equation (18), all additional forces must be included and upgraded.

$$F_A = F_S + F_U \tag{18}$$

The relevant forces needed to estimate the energy required of the automotive engine to overcome air resistance were determined and are comprehensively listed in Table 7. As seen in Table 7, the required energy to tackle the opposing force was greater in the base model than in all other dimple-equipped bus models. In particular, the 100 mm dimple-loaded bus model performed very well with lower required energy than the base model. Hence, with the help of the relationship of required energy, the first 100 mm dimple-equipped bus model was shortlisted as the best model.

3.5. Comprehensive Estimations of Specific Power and Fuel Consumption of the Optimized Bus

The association between specific powers and fuel consumption for the vehicle was discovered through a literature review [30]. After that, the intercity bus's unique fuel consumption through a power relationship was calculated, as seen in Equations (19) and (20).

$$P_{IB}^S = \frac{((F_{RR} + F_D + F_{IB} + F_M + F_A) \times V_b)}{m} \tag{19}$$

All of the compositional parts of Equation (19) were determined using CFD analysis and hence substituted in the same equation. The relative specific power of all the models was calculated and is presented in Figure 74.

$$\text{FC} = \left[0.622 \times P_{IB}^{S} \right] + 0.7 \tag{20}$$

Table 7. Comprehensive estimated data of required energy and its associates of the optimized civilian intercity buses.

| Bus Models	F_{RR} (N)	F_D (N)	F_{IB} (N)	F_A (N)	E_R (W)
Base bus model	1481.814	1560.44	564,151.1735	138.1694	18,114,050.15
30 mm dimple-loaded bus model	1481.736	1550.41	564,121.3957	81.71035	18,110,974.01
50 mm dimple-loaded bus model	1481.345	1574.78	563,972.5067	78.9062	18,106,896.28
75 mm dimple-loaded bus model	1480.21	1806.74	563,540.7286	80.6056	18,100,534.41
100 mm dimple-loaded bus model	1478.294	1904.09	562,811.1725	73.3846	18,080,057.28
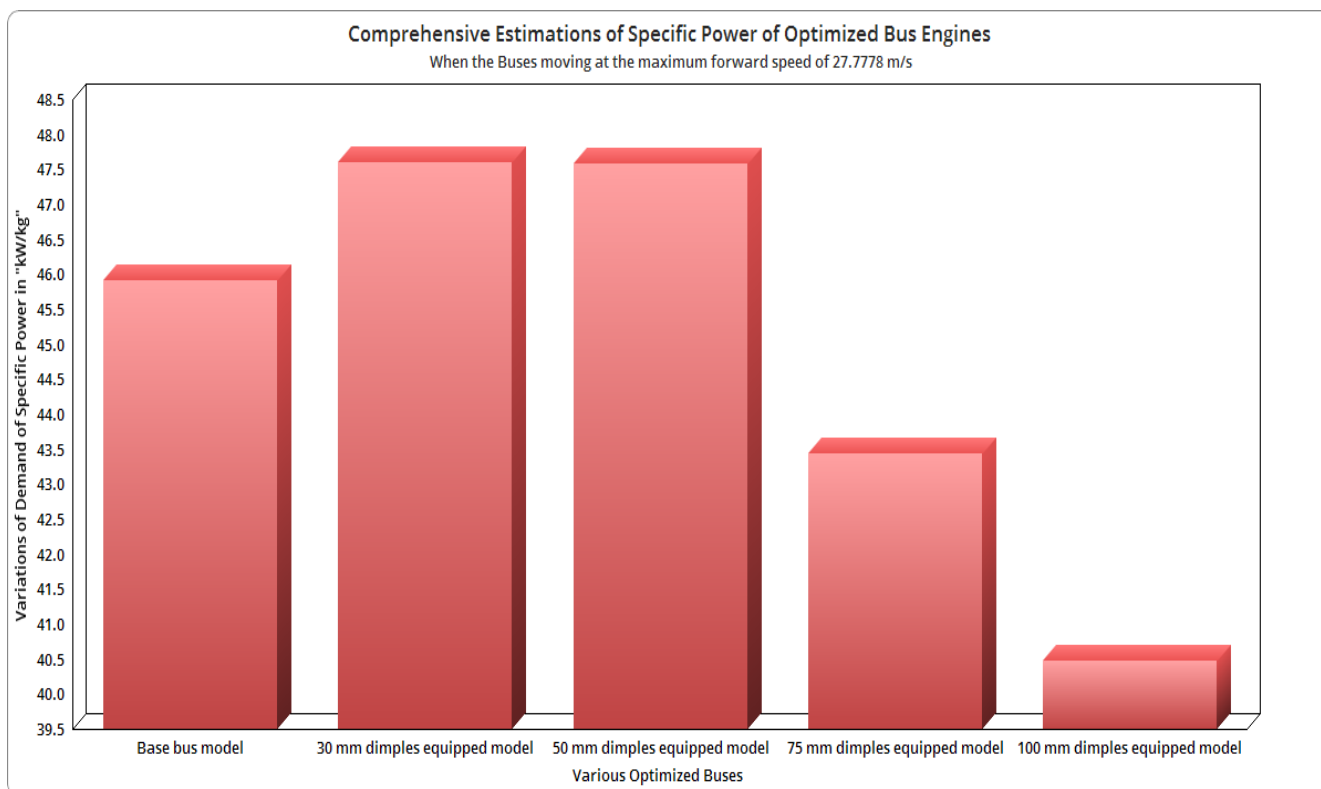
Figure 74. Comprehensive estimations of specific power of the optimized bus engines.

Following the calculation of specific powers, the fuel consumption rate (FCR) was used as an inquiry factor, with Equation (20) taking precedence. The unique relationship was derived and is given in Equation (20) based on the knowledge gathered via historical relationships [30]. The fuel consumption rates for each of the five bus types were calculated and are depicted graphically in Figure 75. As with prior parametric studies, this FCR-based parametric research produced a 100 mm dimple-loaded bus model, which is ideal for completing the objective with good performance.
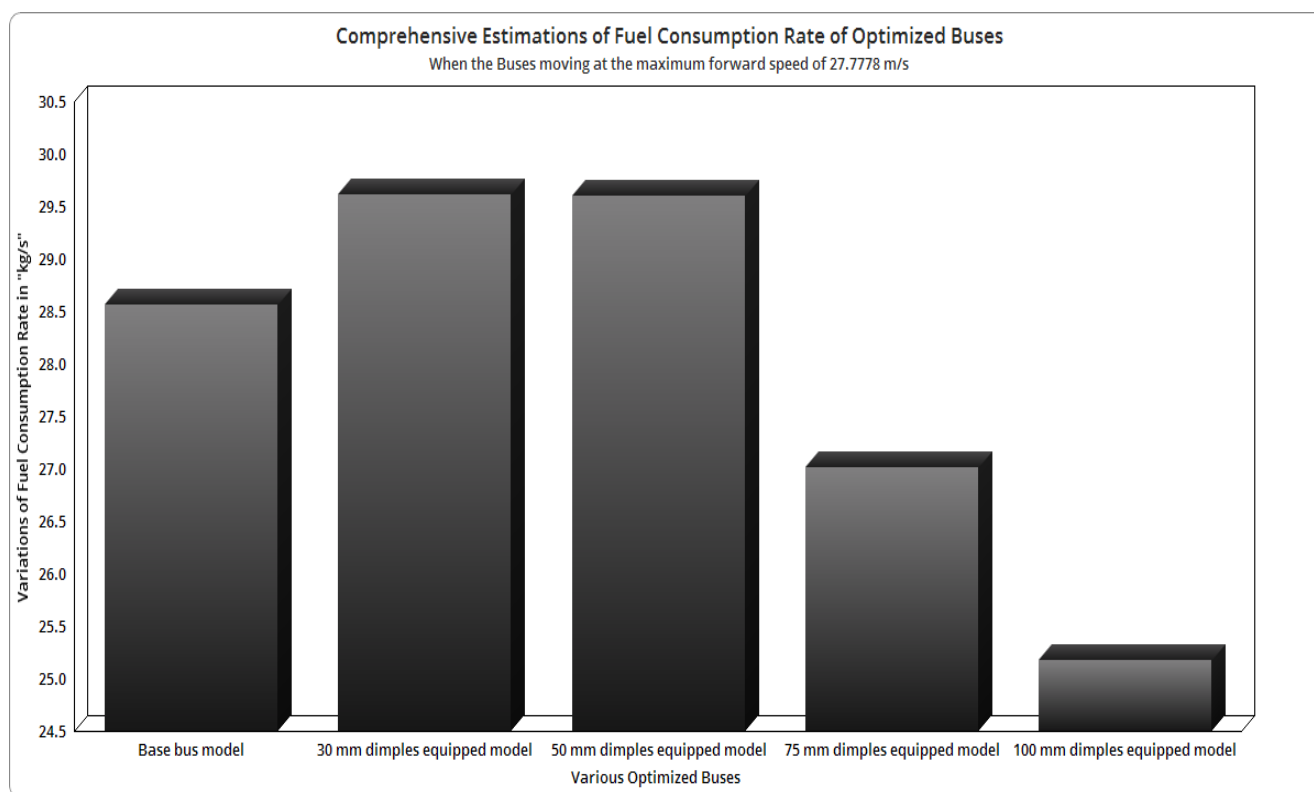
Figure 75. Comprehensive estimations of the fuel consumption rate of the optimized buses.

3.6. Comprehenisve Aeroacoustics Analyses on the Optimized Bus

Aeroacoustics are important in the analysis of the generation of unwanted noise over a vehicle's exterior surface caused by the impact of turbulence. Because this suggested concept involved the imposition of dimples on the exterior surface of an interstate bus, the possibility of turbulence formation was fairly considerable. As a result, the final parametric analysis employed the aeroacoustics technique to examine noise forms across all bus models using ANSYS Fluent 17.2. In addition to all of the standard boundary and beginning conditions presented in the preceding CFD calculations, the broadband noise-based computational model was used for the first time in this aeroacoustics analysis. The intercity bus's speed was estimated to be 100 km/h [31–41]. The computational simulations were carried out using modern facilities loaded with tools, such as ANSYS Fluent 17.2. Figures 76–82 depict the usual decibel fluctuations between bus types. Finally, Figure 83 shows the entire bar chart. To begin, the aeroacoustics calculation was run over the base bus model, and the results are shown in Figures 76 and 77. Figures 78–80 show noise fluctuations for 30 mm, 50 mm, and 75 mm dimpled bus models, respectively. One of the most notable findings is that the highest sound levels created by the bus models exceeded 100 dB in just a few areas. Because of this minor contribution, sound induction would have no negative impact on the passengers' health. The primary sections of all bus models were covered with acceptable noise levels for humans. Thus, the suggested idea has proven that it will not interfere with the performance of the intercity bus and will help a lot in achieving high performance.
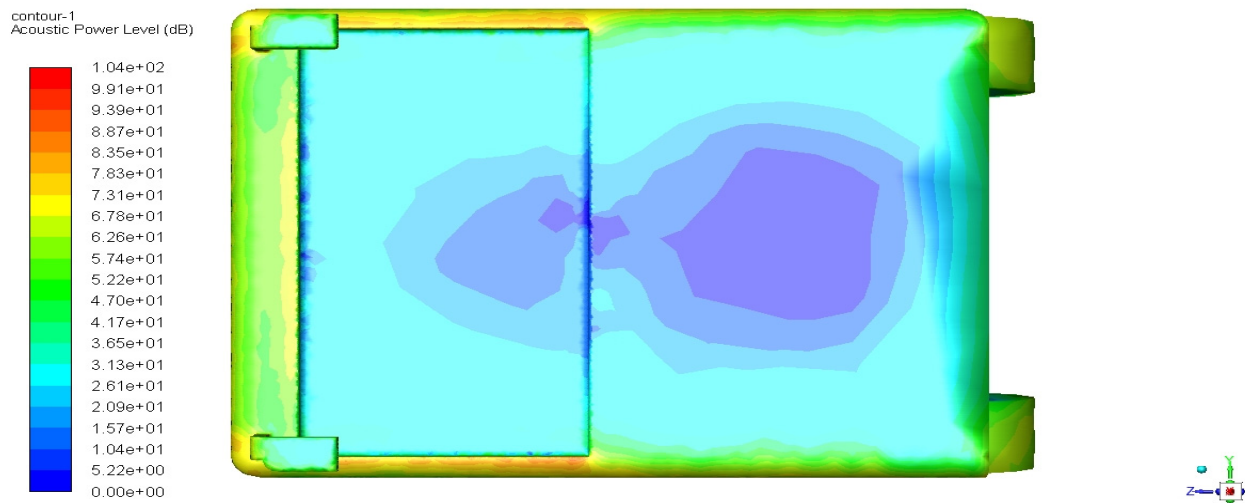
Figure 76. Typical representation of aeroacoustic outputs of the base bus model—front view.
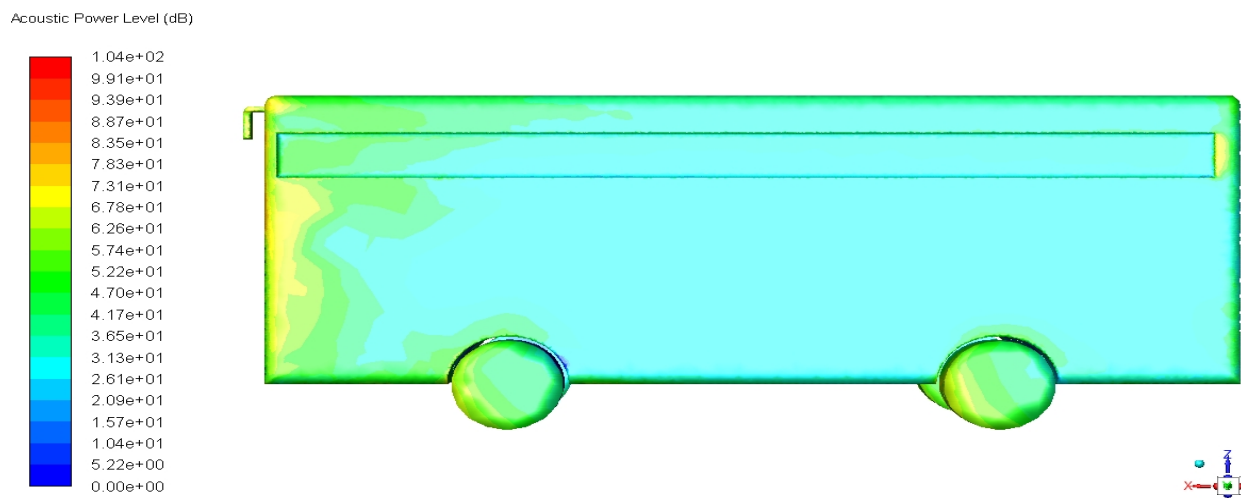

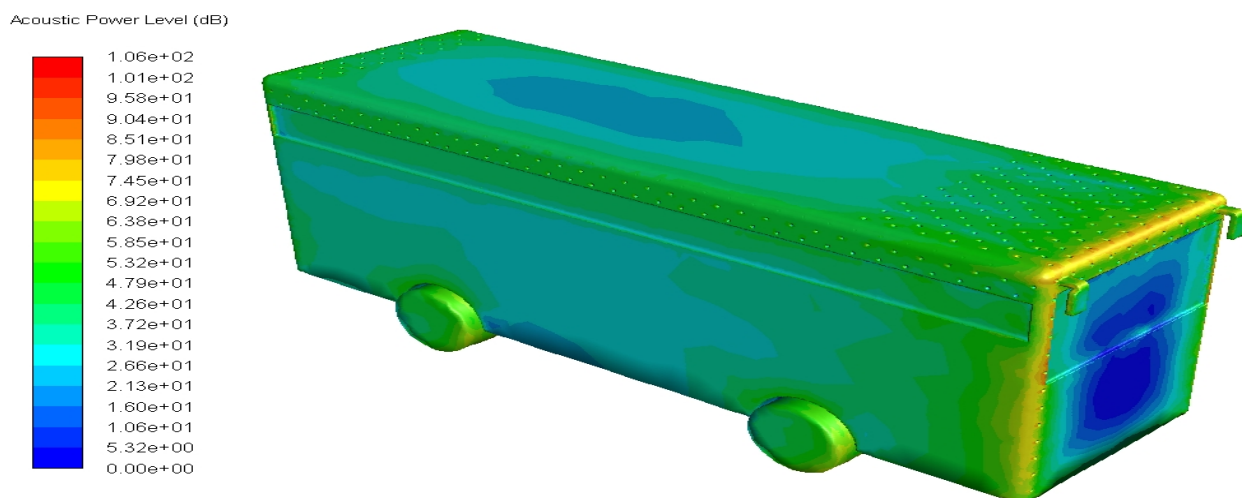**Figure 77.** Typical representation of aeroacoustic outputs of the base bus model—side view.

Figure 78. Typical representation of aeroacoustic outputs of the 30 mm dimple-equipped intercity bus—isometric view.
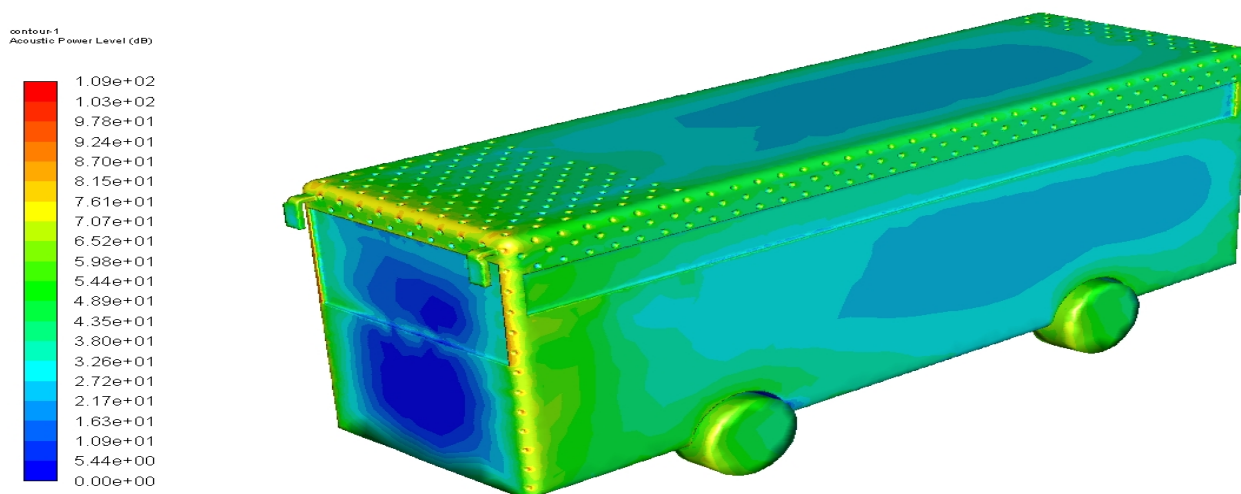
Figure 79. Typical representation of aeroacoustic outputs of 50 mm dimple-equipped intercity bus—isometric view.
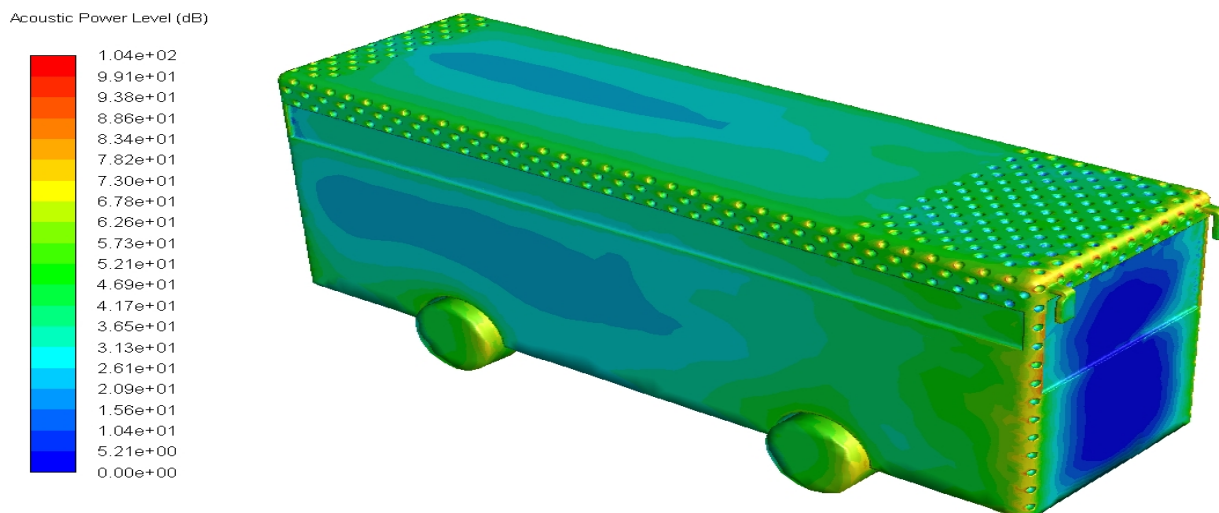

Figure 80. Typical representation of aeroacoustic outputs of 75 mm dimple-equipped intercity bus—isometric view.
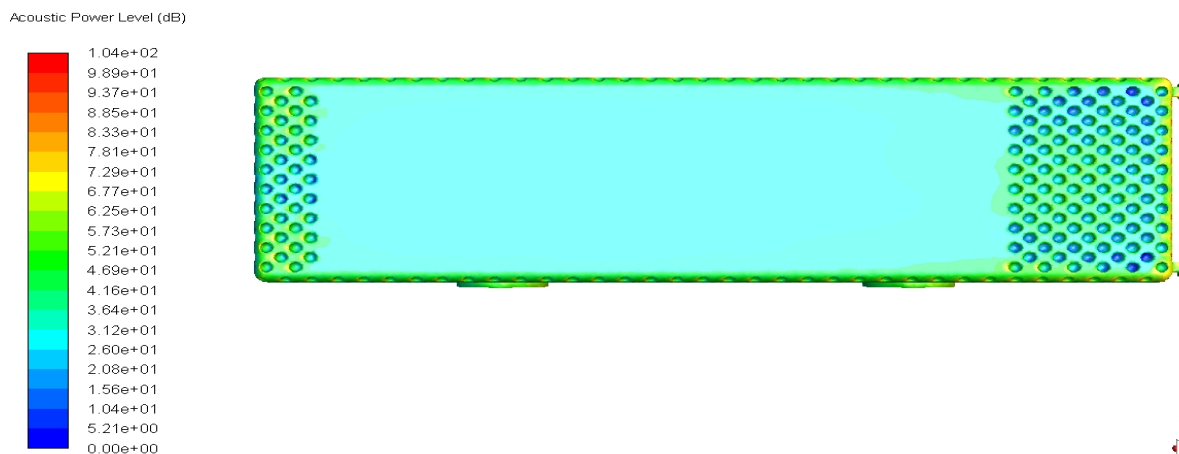

Figure 81. Typical representation of aeroacoustic outputs of 100 mm dimple-equipped intercity bus—top view.
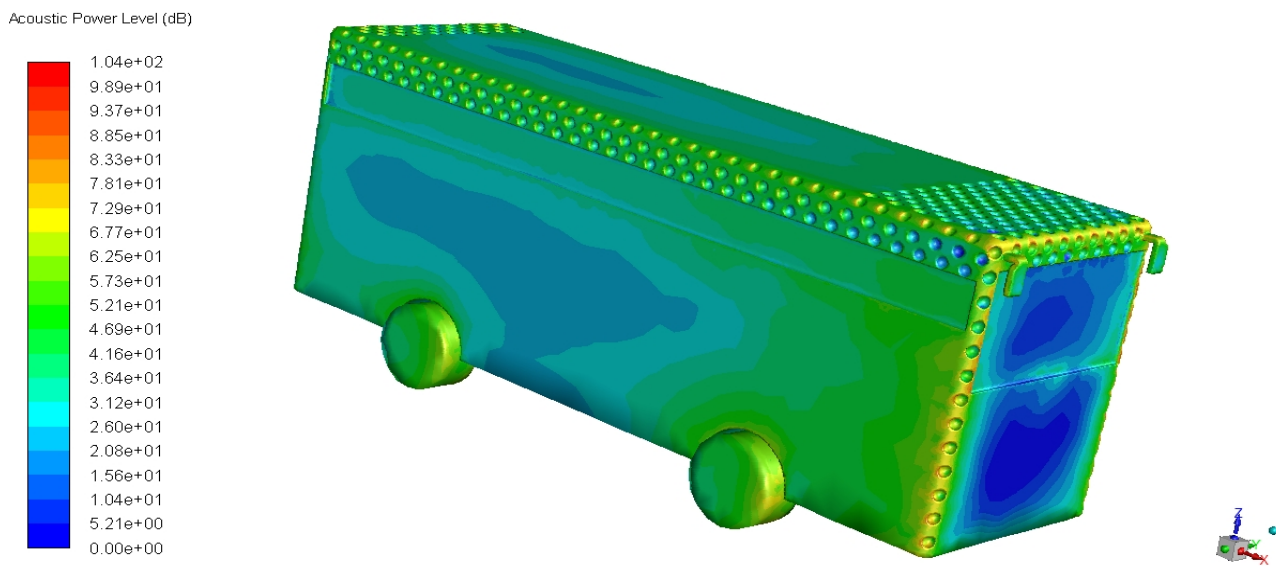
Figure 82. Typical representations of aeroacoustic outputs of 100 mm dimple-equipped intercity bus—isometric view.
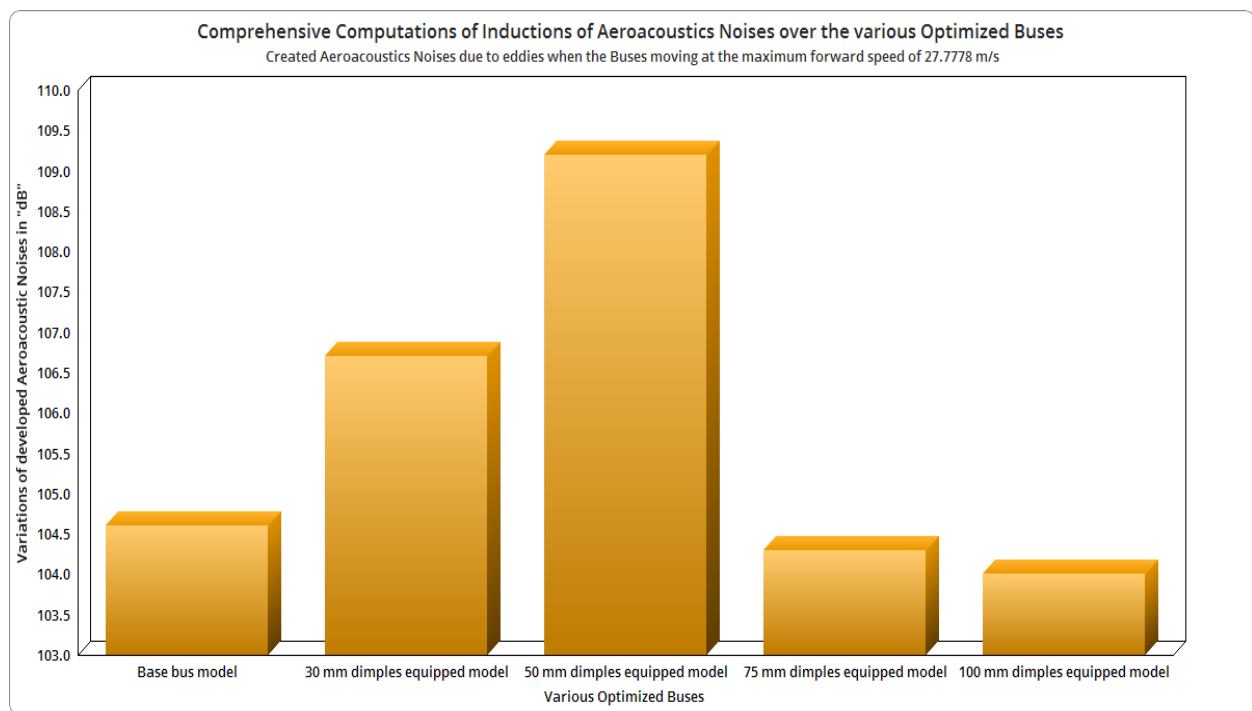
Figure 83. Comprehensive computations of the inductions of aeroacoustics over the various optimized buses.

Finally, the major bus model came into play, which was the 100 mm dimple-loaded bus. The aeroacoustic outputs of the best model (100 mm dimple-loaded bus) are revealed in Figures 81 and 82. The attained noise outcome over this bus model was a tiny level lower than the base bus model. A bar chart shows all of the bus models' full aeroacoustic outputs in Figure 83.

4. Conclusions

The geometry of an intercity bus with and without dimples was modeled using CATIA, and the dimensions of both cases were provided by prior research. The computational studies were performed using ANSYS Workbench 17.2 with the provided boundary conditions

derived from fieldwork. Throughout the convergence of iterations, the coefficient of the drag value was obtained, and it was noticed that the coefficient of the drag decreased from 0.51 to 0.306 at a velocity of 22 m/s. In addition, the drag was reduced from 22 m/s by generating dimples in the front and back of the intercity bus. The subsonic wind tunnel served as a platform for experimental testing, with the identical numerical circumstances being used as the experimental input. The results were compared, and it was proven that creating dimples on an intercity bus is an effective approach to reducing drag.

The pressure difference between turbulence and frictional behavior contributed significantly to this study, so side force production and reduction strategies were emphasized. A total of eight actual bus types were modeled in this regard. The base bus design models were contrasted with side force reduction strategies such as dimples, inverted dimples, riblets, square cuts, and fins. In this research, the side force, pressure, and velocities for all eight models were computed using a CFD-based numerical tool. ANSYS Fluent 17.2 is an example. Finally, comparison studies were run for all models at various crosswind velocities. Table 4 shows that the bus models with dimples led to a reduction in interior force. However, models with square-cuts, fins, and riblets deviated from the goal, preferring side force. Among the dimpled bus models, the one with dimples clustered on the top surface significantly reduced the side force of the bus in contrast to the basic bus model. When compared to the base model, the dimple model (model VIII) reduced side force by 54.35%, 64.79%, and 63.51% for side force velocities of 5 m/s, 10 m/s, and 15 m/s, respectively. To summarize, when compared to the basic bus model, the bus model with dimples grouped on the top surface reduced side force by 61%. As a result, this research offers dimple-based drag reduction approaches that should be adopted in intercity buses to reduce disturbance affecting trip comfort. As seen in Tables 3 and 4, the top performers were model I and model VIII, both of which were equipped with the dimple-based recommended approach. As a result, deployment-based section considerations were used to select the optimal option between model I and model VIII. The application of dimples over the bus was easier in model I than in model VIII, and the sideslip force was somewhat higher in model I, so model I was chosen to offer high efficiency.

The appropriate drag reduction strategies and ideal places to correct the dimples were determined using scaled model-based simulations. The entire real-time bus model was then enforced in multi-parametric research. During multi-parametric examinations of the whole bus model, the drag, side, upward forces, and induced velocities were estimated using CFD, and thus the appropriate opposing factors affecting the model were generated. Second, the energy necessary to combat the opposing variables was computed, with the base bus model requiring more energy than the drag reduction strategies used in the bus models. Third, the specific power of the intercity bus models was determined using a combination of analytical and computational methodologies. Based on the particular power outputs, it was obvious that the 100 mm dimpled bus model did better than others in terms of consuming less specific power. Fourth, the fuel consumption rate of all models was calculated, and the same 100 mm dimpled bus model was nominated as the best performer due to its lower fuel consumption rate than others. Fifth, aeroacoustics approach-based calculations were applied to all models, resulting in noise creation owing to air turbulence. According to the aeroacoustics investigation, the suggested dimple-based idea has no effect on the health of the passengers as the bus approaches the maximum forward speed. Finally, the suggested idea was confirmed to not interfere with the performance of the intercity bus and greatly helped with the accomplishment of high performance. According to the authors, the suggested dimple-based drag reduction approach can significantly improve intercity bus performance by lowering the negative effect of current conventional buses and boosting the positive effect of the same traditional base buses.

Nomenclature

The governing equations implemented in the computational investigations and calculations for the energy required of the engine are predominantly comprised of various nomenclature. Thus, the complete details of the nomenclature involved in this work are tabulated below:

A	Frontal area of the intercity bus (m^2)
a	Acceleration (m/s^2)
C_D	Coefficient of drag (no unit)
C_{RR}	Rolling resistance term coefficient (no unit)
D	Distance traveled by the bus (m)
E_R	Energy required to move the vehicle in forward direction with the inclusion of drag force being conquered (W)
FC	Fuel consumption of an intercity bus (g/s)
$F_{Forward}$	Required force to move the intercity bus in forward direction (N)
F_{RR}	Force generated due to the effect of rolling resistance (N)
F_{IB}	Force generated due to the effect of the inertia of the bus (N)
F_M	Force imparted on the bus when it executes various maneuvers (N)
F_D	Force induced on the bus due to opposing factors (N)
F_A	Force required to resist additional forces when the bus is approaching steady, level movement (N)
F_S	Force required to resist side forces when the bus is approaching steady, level movement (N)
F_U	Force required to resist upward forces when the bus is approaching steady, level movement (N)
g	Acceleration of gravity (m/s^2)
m	Gross vehicle mass (kg)
η_m	Mechanical efficiency of the drive system (in most cases the values is 87%)
P_T	Fluid pressure loaded inside the tire of the bus (bar)
t	Time taken to cover distance D (s)
V_B	Forward velocity of the bus (km/h)
V_b	Forward velocity of the bus (m/s)
P_{IB}^S	Specific power of the intercity bus (W/kg)
ρ_a	Density of the air fluid (kg/m^3)
α	Turning angle of the bus when executes various maneuvers (degrees)

References

1. Senthil Kumar, M.; Vijayanandh, R.; Raj, K.G.; Udhaya, K.A.; Naveen, K.K. Conceptual Design and Aerodynamic Drag Investigation of an Automotive Vehicle. In Proceedings of the 24th National and 2nd International ISHMT-ASTFE Heat and Mass Transfer Conference (IHMTC-2017), Hyderabad, India, 27–30 December 2017.
2. Muthuvel, A.; Murthi, M.K.; Sachin, N.P. Aerodynamic exterior body design of bus. *Int. J. Sci. Eng. Res.* **2013**, *4*, 7.
3. Jadhav, C.R.; Chorage, R.P. Modification in commercial bus model to overcome aerodynamic drag effect by using CFD analysis. *Results* **2020**, *6*, 100091. [CrossRef]
4. Youhanna, E.W.; Mohamed, H.M.; Oraby, W.A.H. Investigation of Crosswind Aerodynamics for Road Vehicles Using CFD Technique. In Proceedings of the ICFD11, Eleventh International Conference of Fluid Dynamics, Alexandria, Egypt, 19–21 December 2013; pp. 1–9.
5. Szodrai, F. Quantitative Analysis of Drag Reduction Methods for Blunt Shaped Automobiles. *Appl. Sci.* **2020**, *10*, 4313. [CrossRef]
6. Thorat, S.G.; Prasad Rao, G.A. Computational Analysis of Intercity Bus with Improved Aesthetics and Aerodynamic Performance on Indian Roads. *Int. J. Adv. Eng. Technol.* **2011**, *2*, 103–109.
7. Patten, J.; McAuliffe, B.; William, M.; Tanguay, B. *Review of Aerodynamic Drag Reduction Devices for Heavy Trucks and Buses*; CSTT-HVC-TR-205; National Research Council of Canada, Centre for Surface Transportation Technology: Ottawa, ON, Canada, 2012.
8. Alonso-Estébanez, A.; Del Coz Díaz, J.J.; Álvarez Rabanal, F.P.; Pascual-Muñoz, P. Numerical simulation of bus aerodynamics on several classes of bridge decks. *Eng. Appl. Comput. Fluid Mech.* **2017**, *11*, 435–449. [CrossRef]
9. Kim, W.; Hong, S.H. The Effect of COVID-19 on the Efficiency of Intercity Bus Operation: The Case of Chungnam. *Sustainability* **2021**, *13*, 5958. [CrossRef]
10. Hemida, H.N.; Krajnovic, S. DES of the Flow around a Realistic Bus Model Subjected to a Side Wind with 30° Yaw Angle. In Proceedings of the Fifth IASME/WSEAS International Conference on Fluid Mechanics and Aerodynamics, Athens, Greece, 25–27 August 2007.
11. Hoonsiri, C.; Chiarakorn, S.; Kiattikomol, V. Using Combined Bus Rapid Transit and Buses in a Dedicated Bus Lane to Enhance Urban Transportation Sustainability. *Sustainability* **2021**, *13*, 3052. [CrossRef]
12. Hariram, A.; Koch, T.; Mårdberg, B.; Kyncl, J. A Study in Options to Improve Aerodynamic Profile of Heavy-Duty Vehicles in Europe. *Sustainability* **2019**, *11*, 5519. [CrossRef]
13. Nikam, K.C.; Borse, S.L. Study of Air Flow through a Open Windows Bus Using OpenFOAM. *Int. J. Fluids Eng.* **2014**, *6*, 53–64.
14. Arun Raveendran, D.R.; Shridhara, S.N. Exterior Styling of an Intercity Transport Bus for Improved Aerodynamic Performance. *sasTech* **2009**, *8*, 9–16.
15. Bettle, J.; Holloway, A.G.L.; Venart, J.E.S. A computational study of the aerodynamic forces acting on a tractor-trailer vehicle on a bridge in cross-wind. *J. Wind. Eng. Ind. Aerodyn.* **2003**, *91*, 573–592. [CrossRef]
16. Abinesh, J.; Arunkumar, J. CFD Analysis of Aerodynamic Drag Reduction and Improve Fuel Economy. *Int. J. Mech. Eng. Rob. Res.* **2014**, *3*, 430–440.
17. Jones, W.P.; Launder, B.E. The Prediction of Laminarization with a Two-Equation Model of Turbulence. *Int. J. Heat Mass Transf.* **1972**, *15*, 301–314. [CrossRef]
18. Launder, B.E.; Sharma, B.I. Application of the Energy Dissipation Model of Turbulence to the Calculation of Flow Near a Spinning Disc. *Lett. Heat Mass Transf.* **1974**, *1*, 131–138. [CrossRef]
19. Wilcox, D.C. *Turbulence Modeling for CFD*, 2nd ed.; DCW Industries: Anaheim, CA, USA, 1998; pp. 107–131.
20. Siddhesh, K.; Prashant, T.; Rajkumar, E. Aerodynamic study of state transport bus using computational fluid dynamics. *IOP Conf. Ser. Mater. Sci. Eng.* **2017**, *263*, 062052. [CrossRef]
21. Ray, A.; Singh, S.N.; Seshadri, V. Evaluation of Linear and Non-linear Hydrodynamic coefficients of Underwater vehicles using CFD. In Proceedings of the ASME 28th International Conference on Ocean, Offshore and Arctic Engineering, Honolulu, Hawaii, 31 May–5 June 2009.
22. Vijayanandh, R.; Kumar, M.S.; Kumar, B.S. Numerical Study on Drag Effect of Waste Collector Attachment in the Train. *Int. J. Mech. Prod. Eng. Res. Dev.* **2018**, *8*, 1060–1078.
23. Kumar, M.S.; Vijayanandh, R.; Kaviarasan, N.; Kumar, R.D.; Arasu, I.A.I.; Kanmaniraja, R. Computational and Theoretical Analysis of Aerodynamic Performance on Roller Airfoil. *Int. J. Eng. Technol.* **2018**, *7*, 637–642. [CrossRef]
24. Raja, V.; Solaiappan, S.K.; Rajendran, P.; Madasamy, S.K.; Jung, S. Conceptual Design and Multi-Disciplinary Computational Investigations of Multirotor Unmanned Aerial Vehicle for Environmental Applications. *Appl. Sci.* **2021**, *11*, 8364. [CrossRef]
25. Manivel, R.; Babin, T.; Kennedy, J.H. A study on the effect of turbulence and vortices on the efficiency of centrifugal fan through CFD simulation. *Int. J. Mech. Prod. Eng. Res. Dev.* **2018**, *8*, 993–1001.
26. Raj Kumar, G.; Balasubramaniyam, S.; Senthil Kumar, M.; Vijayanandh, R.; Raj Kumar, R.; Varun, S. Crash Analysis on the Automotive Vehicle Bumper. *Int. J. Eng. Adv. Technol.* **2019**, *8*, 1602–1607. [CrossRef]
27. Jagadeeshwaran, P.; Natarajan, V.; Vijayanandh, R. Numerical Estimation of Ultimate Specification of Advanced Multi-Rotor Unmanned Aerial Vehicle. *Int. J. Sci. Technol. Res.* **2020**, *9*, 3681–3687.
28. Vijayakumar, M.; Vijayanandh, R.; Vijayanandh, R.; Ramesh, M.; Senthil, K.M.; Raj Kumar, G.; Sivaranjani, S.; Dong, W.J. Conceptual Design and Numerical analysis of an Unmanned Amphibious Vehicle. In Proceedings of the AIAA Scitech 2021 Forum, Online, 11–15 & 19–21 January 2021. [CrossRef]

29. Balaji, S.; Prabhagaran, P.; Vijayanandh, R.; Senthil Kumar, M.; Raj Kumar, R. Comparative computational analysis on high stable platform for long-range applications. *Lect. Notes Civ. Eng.* **2020**, *31*, 369–391. [CrossRef]

30. Mieszek, M.; Mateichyk, V. Determining the fuel consumption of a public city bus in urban traffic. *IOP Conf. Ser. Mater. Sci. Eng.* **2021**, *1199*, 012080. [CrossRef]

31. Vijayanandh, R.; Kiran, P.; Indira Prasanth, S.; Raj Kumar, G.; Balaji, S. Conceptual Design and Optimization of Flexible Landing Gear for Tilt-Hexacopter Using CFD. In Proceedings of the International Conference on Unmanned Aerial System in Geomatics, Roorkee, India, 6–7 April 2019; pp. 151–174. [CrossRef]

32. Vijayanandh, R.; Senthil Kumar, M.; Vasantharaj, C.; Raj Kumar, G.; Soundarya, S. Numerical Study on Structural Health Monitoring for Unmanned Aerial Vehicle. *J. Adv. Res. Dyn. Control Syst.* **2017**, *9*, 1937–1958.

33. Senthil Kumar, M.; Vijayanandh, R.; Rahul Srinivas Arun Karthik, D.; Tamil Mani, M. Acoustic Analysis and Comparison of Chevron Nozzle Using Numerical Simulation. *Int. J. Mech. Prod. Eng. Res. Dev.* **2018**, *8*, 1089–1103.

34. Murugesan, K.; Vijayanandh, R.; Venkatesan, R.; Saravanan, R.; Senthilkumar, S.; Darshan Kumar, J. Conceptual Design of High Endurance cum Hybrid Configuration based Personal Air Vehicles with Three-Axis Solar Tracker System. In Proceedings of the 2021 International Conference on Advancements in Electrical, Electronics, Communication, Computing and Automation (ICAECA), Coimbatore, India, 8–9 October 2021. [CrossRef]

35. Kumar, M.S.; Vijayanandh, R.; Kumar, G.R.; Kumar, B.S.; Nishanth, B.; Ramesh, M.; Balaji, S. Numerical and experimental performance estimations of the passenger train with waste collector near Windows. *AIP Conf. Proc.* **2021**, *2317*, 050007. [CrossRef]

36. Udhaya Prakash, R.; Raj Kumar, G.; Vijayanandh, R.; Senthil Kumar, M.; Ram Ganesh, T. Structural analysis of aircraft fuselage splice joint. *IOP Conf. Ser. Mater. Sci. Eng. J.* **2016**, *149*, 012127. [CrossRef]

37. Aswin Kumar, V.; Sivaguru, M.; Rohini Janaki, B.; Sumanth Eswar, K.S.; Kiran, P.; Vijayanandh, R. Structural Optimization of Frame of the Multi-Rotor Unmanned Aerial Vehicle through Computational Structural Analysis. *IOP J. Phys. Conf. Ser.* **2021**, *1849*, 012004. [CrossRef]

38. Vijayanandh, R.; Ramesh, M.; Raj Kumar, G.; Thianesh, U.K.; Venkatesan, K.; Senthil Kumar, M. Research of Noise in the Unmanned Aerial Vehicle's Propeller using CFD. *Int. J. Eng. Adv. Technol.* **2019**, *8*, 145–150. [CrossRef]

39. Vijayanandh, R.; Ramesh, M.; Venkatesan, K.; Kumar, G.R.; Kumar, M.S.; Rajkumar, R. Comparative Acoustic Analysis of Modified Unmanned Aerial Vehicle's Propeller. *Lect. Notes Mech. Eng.* **2021**, *45*, 557–571. [CrossRef]

40. Ramesh, M.; Vijayanandh, R. Acoustic Investigation on Unmanned Aerial Vehicle's Rotor Using CFD-MRF Approach. In Proceedings of the ASME 2019, Gas Turbine India Conference—GTINDIA 2019, Chennai, India, 5–6 December 2019; Volume 2, pp. 1–7. [CrossRef]

41. Rashidi, M.M.; Bég, O.A.; Parsa, A.B.; Nazari, F. Analysis and optimization of a transcritical power cycle with regenerator using artificial neural networks and genetic algorithms. *J. Power Energy* **2011**, *225*, 701–717. [CrossRef]